SINGLE AND DOUBLE IONIZATION CROSS SECTIONS FOR ALKALI AND ALKALINE EARTH IONS BY ELECTRON IMPACT

Takato HIRAYAMA

Department of Physics
Faculty of Science and Technology
Sophia University

A thesis submitted to Sophia University
in partial fulfilment of the requirements
for the degree of Doctor of Science

January 1987

ABSTRACT

The absolute cross sections for electron impact single and double ionization of singly charged alkali and alkaline earth ions have been measured as functions of electron energies with the use of the electron-ion crossed beam technique. The following cross sections have been measured;

$$
\begin{aligned}
e + Na^+ &\text{ --- } Na^{2+} + e + e \\
&\text{ --- } Na^{3+} + e + 2e \\
e + K^+ &\text{ --- } K^{2+} + e + e \\
&\text{ --- } K^{3+} + e + 2e \\
e + Sr^+ &\text{ --- } Sr^{2+} + e + e \\
&\text{ --- } Sr^{3+} + e + 2e \\
e + Ba^+ &\text{ --- } Ba^{2+} + e + e \\
&\text{ --- } Ba^{3+} + e + 2e
\end{aligned}
$$

The target ion beams produced in a thermionic emission type or a surface ionization type ion source were crossed at right angles by the electron beam.

The results for the single ionization cross sections of these ions are in good agreement with the previous measurements by the other groups. The results for single ionization of K^+, Sr^+ and Ba^+ show the evidences of the excitation-autoionization processes.

The results for the double ionization cross sections of these ions provide the first experimental data obtained by the systematic measurements. The results for double ionization of K^+, Sr^+ and Ba^+ show evidences of the inner-shell direct ionization followed by autoionization. Especially for Ba^+ distinctive

structures which are attributable to the direct ionization of 4d and 5s electrons followed by the autoionization are clearly observed.

Experimental results for single ionization are compared with the semi-empirical Lotz formula, distorted wave calculations by Younger and other theoretical predictions available for these ions. For the double ionization there are a limited number of theoretical calculations available up to now. Younger has succeeded in reproducing the Ba^+ double ionization results qualitatively, in which he showed that the contribution from indirect processes are dominant, using the distorted wave method.

The thesis contains a brief review of experimental and theoretical approach on our subject up to now, followed by a detailed description of the experimental method, apparatus and procedures used to obtain absolute cross sections. The experimental results are presented with discussions of experimental accuracies. The experimental results are compared with published experimental data and theoretical calculations.

Table of CONTENTS

List of Figures

List of Tables

CHAPTER 1

INTRODUCTION

1-1 General Introduction

Collisions between electrons and ions have long been of interest to astrophysicists who require knowledge of the basic collision processes involved between the electrons and ions in a plasma, in attempting to model conditions in non-equilibrium plasmas occurring in stellar atmospheres which are usually so tenuous that the laws of equilibrium thermodynamics cannot be strictly applied. Many of the plasma properties, for example the radiation emitted, depend on the state of ionization of ions in these plasmas. Moreover, cross section data on the electron-ion collision processes with high accuracy has been strongly requested in recent years by fusion research aiming towards controlled thermonuclear plasmas as energy sources.

It is also interesting to discover how the Coulomb charge of an ion influences a reaction. A striking example is the excitation of positive ions by electron impact including the excitation to the autoionizing levels where the attractive field ensures that many partial waves contribute to excitation, even at threshold. Thus the excitation function of a positive ion is finite and usually large at threshold, whereas for a neutral atom it is zero.

While the electron impact ionization of atoms has been investigated experimentally since the end of the last century,[1] it was not until 1961, because of experimental difficulties, that the high-quality crossed-beam experiment measuring electron impact ionization of an ion (He^+) was reported by Dolder et al.[2]

The experimental problems will be discussed in Chapter 2-4.

Theoretical treatment of electron impact ionization of ions is also very difficult. There is a variety of possible ionization mechanisms which have to be considered. Possible processes including not only direct mechanisms but also indirect mechanisms, which lead to ionization, are listed in Table 1-1.

In addition to the complexity in the ionization mechanisms, ionization theory is difficult as the two (in single ionization) or more (in multiple ionization) free electrons continue to interact with the ion core and each other out to infinity due to the Coulomb potential. Thus, the asymptotic region should be treated as a three-body or many-body problem whose full solution is not possible and various simplifying approximations are needed to be applied. A survey of theoretical work will be given in Chapter 3.

1-2 Derivation of the Cross Section from Measured Quantities.

In this section an expression for the cross section for the crossed-beam experiments will be developed in terms of experimentally determined quantities.

To measure absolute cross sections for atomic collision processes it is necessary to know and control the densities of the colliding atomic species A and B and to measure the rate at which collisions occur within a well defined volume. The cross section at a collision energy E corresponding to a collision velocity v is given by

$$\sigma(E) = R_C (N_A \cdot N_B \cdot v \cdot V)^{-1}, \quad \text{---------- (1-1)}$$

Table 1-1. Electron Impact Ionization Processes.[$]

1. Direct single ionization

$$e + A^{q+} \text{ --- } A^{(q+1)+} + e + e$$

2. Excitation-autoionization

$$e + A^{q+} \text{ --- } [A^{q+}]^* + e$$
$$\qquad\qquad\qquad\qquad \text{└--- } A^{(q+1)+} + e$$

3. Resonant-recombination double autoionization

$$e + A^{q+} \text{ --- } [A^{(q-1)+}]^*$$
$$\qquad\qquad\qquad\qquad \text{└-- } [A^{q+}]^* + e$$
$$\qquad\qquad\qquad\qquad\qquad\qquad \text{└----- } A^{(q+1)+} + e$$

4. Resonant-recombination auto-double ionization

$$e + A^{q+} \text{ --- } [A^{(q-1)+}]^*$$
$$\qquad\qquad\qquad\qquad \text{└-- } A^{(q+1)+} + e + e$$

5. Direct-double ionization

$$e + A^{q+} \text{ --- } A^{(q+2)+} + e + e + e$$

6. Ionization-autoionization

$$e + A^{q+} \text{ --- } [A^{(q+1)+}]^* + e + e$$
$$\qquad\qquad\qquad\qquad \text{└-- } A^{(q+2)+} + e$$

7. Excitation-double autoionization

$$e + A^{q+} \text{ --- } [A^{q+}]^* + e$$
$$\qquad\qquad\qquad\qquad \text{└--- } [A^{(q+1)+}]^* + e$$
$$\qquad\qquad\qquad\qquad\qquad\qquad \text{└--- } A^{(q+2)+} + e$$

8. Excitation auto-double ionization

$$e + A^{q+} \text{ --- } [A^{q+}]^* + e$$
$$\qquad\qquad\qquad\qquad \text{└--- } A^{(q+2)+} + e + e$$

[$]Although other names for these processes have appeared in literatures, these names are recommended to be the most descriptive and least confusing.[3)]

where R is the number of interactions occurring per second, N_A, N_B are the densities of species A and B, respectively, V is the collision volume.[4)]

When the both species or the either of A or B are the neutral atom or molecule, it is very difficult to determine the densities N_A , N_B and the collision volume V accurately. But in the case of the electron-ion collision experiment as in this study, these quantities can be easily determined experimentally by measuring the current and the current density distribution of both beams because the projectile (electron) and the target (ion) are both charged particles.

Because N_A, N_B, v, and V in equation (1-1) are not directly measurable quantities, they must be modified in terms of experimentally determined parameters.

The current densities of both beams are usually non-uniform. In electron-ion collisions, the ion beam is uniform in its direction of motion, and any variation in the direction of motion of the electrons will be averaged out. Similarly, for the electron beam, only non-uniformity in the direction perpendicular to the beams, z direction need to be considered.

Taking account of the above consideration, it is convenient to consider the beam interaction geometry as shown in Fig.1-1, i.e. the width of both beams at a position z are $W_A(z)$ and $W_B(z)$ where the z-axis is the direction perpendicular to the plane including the beam A and B, the beam A and B with the velocity of v_A and v_B, respectively, collide with each other at right angles.

The number of collisions occurring per second in the element of height dz at z is given by differentiating the equation (1-1) as follows,

$$R_C(z)dz = \sigma(E) \cdot N_A(z) \cdot N_B(z) \cdot v \cdot dV(z) \ , \quad \text{---------- (1-2)}$$

where $N_A(z)$ and $N_B(z)$ are, respectively, the particle number densities in the beam A and B at height z.

Here $N_A(z)$, $N_B(z)$, v and dV(z) must be rewritten in terms of experimental parameters.

$$N_A(z) = i_A(z)(q_A \cdot e \cdot W_A(z) \cdot v_A)^{-1}, \quad \text{---------- (1-3)}$$

$$N_B(z) = i_B(z)(q_B \cdot e \cdot W_B(z) \cdot v_B)^{-1}, \quad \text{---------- (1-4)}$$

$$v = (v_A^2 + v_B^2)^{1/2} \ , \quad \text{---------- (1-5)}$$

and

$$dV(z) = W_A(z) \cdot W_B(z) \cdot dz \ , \quad \text{---------- (1-6)}$$

where $i_A(z)$ and $i_B(z)$ are the linear current densities at height z of beam A and B, respectively, v_A and v_B are the velocities of respective beam, q_A and q_B are the respective charge states of beam A and B, and e is the magnitude of the electronic charge.

By substituting these equation to eq(1-2), one can obtain

$$R_C(z)dz = \sigma(E) \frac{i_A(z)\ i_B(z)\ dz}{q_A\ q_B\ e^2} \frac{(v_A^2 + v_B^2)^{1/2}}{v_A\ v_B} \quad \text{-- (1-7)}$$

For the collisions between electron and singly charged ion, q_A and q_B equal to unity and $i_A(z)$, $i_B(z)$, v_A and v_B can be written as $i_i(z)$, $i_e(z)$, v_i and v_e, respectively.

Finally, the total number of interactions per second is

given by integrating eq(1-7) over the beam heights which is assumed to extend between plus infinity and minus infinity.

$$R_C = \sigma(E) \frac{\int i_i(z)\, i_e(z)\, dz}{e^2} \frac{(v_i^2 + v_e^2)^{1/2}}{v_i\, v_e} \quad \text{---------- (1-8)}$$

Solving for o(E) eq(1-7) is rewritten as

$$\sigma(E) = \frac{R}{I_i I_e} e^2 \frac{v_i v_e}{(v_i^2 + v_e^2)^{1/2}} \frac{F}{D} , \quad \text{---------- (1-9)}$$

where R is counting rate of product particle, I_i, I_e are the respective beam currents of ion and electron, D is an efficiency of product particle detector, i.e., R_C equals to R/D, and F is the form factor of the interaction region which takes account of non-uniform current densities within the beams defined by

$$F = \frac{\int i_i(z)\, dz \int i_e(z)\, dz}{\int i_i(z)\, i_e(z)\, dz} \quad \text{---------- (1-10)}$$

The form factor F is evaluated from the measurements of the spatial current distributions of electron and ion beams by moving a shutter with a narrow horizontal slit (0.1 mm high), vertically (i.e. along the z axis). (See Chapter 5-4)

CHAPTER 2

EXPERIMENTAL APPROACH TO ELECTRON IMPACT IONIZATION

In order to determine the ionization cross section, it is necessary to measure the reaction rate in an experimental condition where the densities of the electrons and ions, the relative impact velocity and the collision volume are known, as shown in eq (1-1) in chapter 1-2. The techniques which have been commonly used to measure all or some of these parameters, i.e. to measure the ionization cross sections of ions are the plasma spectroscopy method, the trapped-ion method and the crossed-beam method.

In this chapter a brief description of these methods will be given. And the some difficulties commonly encountered in the crossed-beam arrangement, which is adopted in this study, will also be discussed.

2-1 Plasma Spectroscopy Method.

Analysis of the spectral emission of a plasma can provide information about the ionization rate coefficients of the plasma constituents, and the ionization cross sections can be determined from these. If the electron temperature and density of a plasma are known (and a variety of measurement techniques are available) the excitation or ionization reaction rates can be deduced from intensity measurements of the time-resolved spectral emission of a transient plasma. Using a computer program, the ionization rate coefficients are searched for by varying them until the calculated time histories of properly chosen lines emitted by the desired ions agree with the observed ones.

This method suffers from the disadvantages that it is diffi-

cult to isolate a particular process to study, and that the rate coefficients determined may include ionization from excited states as well as from inner shells.

This technique has the advantages that rate coefficients are measured directly and that measurements can be made even for highly charged ions which may be unable to be produced in sufficient numbers usable for crossed-beam experiments.

Rate coefficients obtained by this method for hydrogen-like ions are in good agreement with those obtained from crossed-beam measurements, but are increasingly lower for more complex ions (about 15% lower for helium-like and 40% lower for lithium-like ions).[5] The reason for this discrepancy is not understood.

For more detail, refer to the references.[6],[7]

2-2 Trapped-Ion Method.

This method is based on the ionization of ions held in a trap, and bombarded by electrons. Cross sections for successive ionization to higher charge states can be deduced from the charge state analysis of extracted ions by means of a mass spectrometer or a time of flight method.

Several experimental approaches have been developed for the trapping of ions.[8] The most successful method is the onedeveloped by Baker and Hasted[9]. They make use of the space charge of an electron beam constrained by an axial magnetic field. Since the trapping time can be increased considerably by applying proper potential wells to the ends of the beam, the electron energy dependence of currents of multiply charged Cs^{n+} and Ba^{n+} ions (up to n = 10) could be measured.[10]

In recent years Donets and Ovsyannikov have further developed this concept to a high degree of perfection. By variation of

the trapping time, the charge state distribution of ions extracted from the Electron Beam Ion Source (EBIS) can be controlled.[11]

2-3 Crossed-Beam Method

The technique of crossed electron-ion beam has provided the most accurate and detailed information on electron impact ionization mechanisms described in Table 1-1. The general features and/or results of crossed-beam experiments have been discussed and reviewed by a number of authors[12-20].

The principle of the crossed-beam apparatus is shown in Fig.2-1. A target beam of ions of a given species, charge state and energy is collided with a monoenergetic electron beam, which further ionizes a small fraction of the target beam. Parent and product ions are separated downstream by the field of an electric or a magnetic analyzer and detected by collectors.

This technique was first applied successfully by Dolder et al.[21], who measured the cross sections for the process

$$He^{+} + e \text{ --- } He^{2+} + e + e.$$

Since that time, the ionization cross sections for a wide range of ion species are measured using the crossed-beam method. Recent activities of the some groups in this field are as follows.

(i) Culham Laboratory

Since 1983, Culham group has been studing the species which are likely to be present as impurities within fusion plasmas. The results recently reported by this group are single ionization cross sections for Al^{+}, Fe^{+}, W^{+}, Ni^{+}, Ti^{+}, Ti^{2+}, Ne^{+} and Ar^{2+}

ions[22-27].

They have also started to measure the ionization cross sections of neutral atoms using the crossed-beam technique and reported the results for He[28] and Fe[26].

(ii) Giessen University

This group mainly has been studing the single and multiple ionization processes for multiply-charged ions.

In 1980 they reported the first systematic measurements of multiple ionization cross sections for multiply charged Ar ions[28]. In this paper, they found the contribution from inner-shell direct ionization followed by autoionization became larger as the charge state became higher.

In 1985 they reported that at higher energies the electron impact single ionization cross sections for Sb^{2+} and Bi^{2+} ions were larger than the corresponding cross sections for Sb^{+} and Bi^{+} ions, respectively.[29] This extraordinary behaviour was explained by a consequence of the effect that the nd hole configuration goes to bound state from autoionization state when the charge state of the Sb and Bi ions is increased from +1 to +2.

And they also reported the systematic measurements on the single and multiple ionization cross sections for Xe ions[30] and Kr ions[31].

(iii) Oak Ridge National Laboratory. (Partly with the collaboration with the Joint Institute for Laboratory Astrophysics)

They have been measuring the single and multiple ionization cross sections for highly-charged ions produced in a Penning IonizationGage type ion source (ORNL-PIG). They reported the measurements of the iso-electronic sequence (Li-like[32], Na-like[33] and Mg-like[34] ions) and iso-nuclear sequence for rare-gas ions[35,36].

Very recently, they made a new Electron Cyclotron Resonance (ECR) type ion source[37], which works remarkably well. With the use of this new ion source, they measured the cross sections of triple ionization for Xe^{6+} [38], and the single ionization of Fe^{q+} ions for ion charge states q=5 up to q=15 (Na-like)[39].

(iv) Institute of Plasma Physics, Nagoya University.

They measured the single ionization cross sections of doubly-charged rare-gas ions with the ECR ion source.[40] In the results of Ar^{2+}, they found a structure which suggested a characteristic contribution from a sub-shell (3s) ionization.[41] They are now in progress to study the ionization for the ions whose configurations are $3s^2 3p^n$ systematically in order to confirm the idea mentioned above.[41,42]

2-4 Experimental Problems in Crossed-Beam Experiments

(i) Background signals

The particle density of ion beam is very low. In the present study, the ion beam of order of 10^{-8} A of singly charged ions are used giving particle densities of order of 10^6 cm^{-3}, which correspond to the vacuum pressure of 10^{-11} Torr. Even when a large electron current is used the probability of an ion being ionized is small and typically lies in the rage of 10^{-7} - 10^{-11}. The ratio of product to target ions is extremely small and careful design of the analyzer and particle collectors is required.

The pressure in the vacuum system usually lies in the order of 10^{-9} Torr during the both beams on and so the residual gas density exceeds the target beam density. The beam energy (2-3 keV) is sufficient to produce product ions in stripping collisions between beam ions and the residual gas at a rate of the comparable order to the true collision rate. These background

signals must be separated from the true signals. To realize the separation of true signals from background signals, the double beam modulation technique[43] is used in this study. Details of this method will be discussed in chapter 4-7. In this method electron and ion beams are pulsed. Pulsing the beams can be a source of error since the chopped beam may hit the surface of the electrode which can lead to the modulation of the background gas density. To avoid this background modulation, high chopping frequency must be used, and the measured cross section is shown to be independent of both pulse rate and electron current. (see Chapter 5-7)

(ii) Contaminated ion beam

In electron-ion collision experiment, various types of ion source are used. For example, Electron Cyclotron Resonance (ECR) type, Penning Ionization Gauge (PIG) type, Electron Beam Ion Source (EBIS), are widely used. The method of the production of ions in these ion sources are different but, in principle, the ions are produced by the collision between electrons and atoms and/or molecules, and the successive collisions between electrons and ions. So there is a possibility that the parent ion beam extracted from these ion sources may contain some states other than the ground state. The possibility of this is reduced by using an electron energy which is too low to produce ions directly in excited states in the source, and by having the time of flight to the collision region sufficiently long that these excited states will have enough time to decay. Ions in metastable states, however, will reach the collision region and can become a source of error.

In this study a thermionic emission type and a surface ionization type ion source are used. Because ions are produced by

thermal reaction in these ion source and the thermal energy is so low (less than 1 eV) that the excited states of ions can not be produced except for the heavy ions. In Ba^+ there is a possibility that the ions can contain some fraction of metastable states, which will be discussed in Appendix A-3.

(iii) Space Charge

The current densities in the beams must be kept sufficiently low to ensure the beams do not expand unacceptably as a result of mutual repulsion between their charges. This can be a problem especially with a low energy electron beam, but not with the ion beam because of its low density.

An additional problem concerning the space charge is the interaction of the two beams at the crossing region. The space charge of the electron beam will have a focusing effect on the ion beam, and ions which would normally reach the collector may be deflected so that the some part of the ion beams can not be detected. This effect gives a modulation of the collected current and a spurious signal which can be of either sign. It has been discussed in detail by Harrison[12]. This problem can be reduced by making the electron beam wider than the ion beam so that the focusing effect is not so large. Moreover, in order to collect all of the ions, including those deflected, the ion collectors should be made with large entrance apertures and mounted close to the collision region. Any change in the recorded signal due to this effect will be found as a non-linearity in a graph of signal against electron current. (See Chapter 5-7)

(iv) Beam profiles

The unstability and the change in shape of the profile of the both beams with time can be a source of error of the form factor, F. To minimize this error, in general, the one beam is

made wider than the another beam and the current density profile of the wider beam is kept as flat topped as is possible. The advantage to adopt such beam configuration will be shown in Chapter 5-4.

The difficulty in measuring the beam profile with high accuracy and a means of avoiding the necessity has been proposed by Brouillard et al. in 1981.[44] They suggest sweeping one beam across the other at a constant speed so that the one beam intersects each part of the another beam in turn. This method has several advantages. It does not require a separate measurement of the form factor and, furthermore, since both beams are always 'on', background pressure modulation effects cannot occur.The amplitude of the sweep displacement is large enough to produce no overlap of the beams in the extreme positions. This gives a convenient way to measure the background events due to gas-stripping collisions. The number of accumulated signal counts obtained in the overlap region is directly proportional to the ionization cross section and to the total intensities of both beams, no matter how these intensities are distributed spatially across the beams. This technique has recently been applied by the Giessen group with good results.[45]

CHAPTER 3

THEORETICAL APPROACH TO ELECTRON IMPACT IONIZATION

As mentioned in Chapter 1-1, the theoretical treatment of electron impact ionization is very difficult. Additional to the many-body nature of the problem there are a variety of possible ionization mechanisms which have to be considered as seen in Table 1-1.

In this chapter a brief outline of the theoretical methods, both classical and quantal, is given. The details can be found in references 46-48).

3-1 Classical Theory

In 1912 Thomson[49] had used classical theory of the binary encounter approximation to describe electron impact ionization of neutral atoms. Considering the energy transfer via Coulomb interaction from the incident electron to one of the atomic electrons at rest he deduced that the total ionization cross section σ at collision energy E is given by

$$\sigma(E) = 4\pi a_0^2 R \frac{n}{P_i E} \left(1 - \frac{P_i}{E}\right) , \qquad (3\text{-}1)$$

where n is the number of equivalent electrons of a shell with binding energy P_i, a_0 is the Bohr radius, and R = 13.6 (eV).

Thomson's theory implies a scaling of cross sections of an atom, $o_1(x)$, and an isoelectronic ion, $o_2(x)$, according to

$$\frac{\sigma(E)}{\sigma(E)} = \left(\frac{I_{P2}}{I_{P1}}\right)^2 , \qquad (3\text{-}2)$$

where $x = E/P_i$ are reduced energies, i.e., the incident electron energies are expressed in terms of the respective ionization energies P_{i1} and P_{i2}. The attractive Coulomb field of the ion however increases the kinetic energy of the incident electron and leads to a reduction in its impact parameter. Thus the cross section of the ion is enhanced for electron energies in the threshold region, whereas fast electrons are scarcely influenced.

This simple formula for the cross section reproduce the shape of the cross section curve remarkably well, although it overestimates the cross section at low energies and has the wrong energy dependence at high energy (1/E instead of lnE/E as required by quantum mechanics).

However, because of its simplicity, Thomson's approach has formed the basis for many attempts aiming at improved classical binary encounter calculations. The theory has been modified for ionization of ions to incorporate the Coulomb effect on the incident electron[50]. The restriction that the target electron is at rest prior to the collision was removed and various distributions of initial velocities were taken into account[51]. A further modification of the model, known as the 'exchange-classical' approximation, included certain quantum features like electron exchange and interference.[52]

Another classical approach is based on the impact parameter treatment of the ionization collision process[53]. This method reproduces the correct high energy behaviour of the cross section (lnE/E) since the binary nature of the collision is removed and many-body effects are accounted for.

Finally, in the 'exchange-classical impact-parameter' (ECIP) method[52], both previous approaches have been combined to incorporate the complementary advantages of the two theories. The

'exchange-classical' approximation is used to describe the close collisions ($r < R_0$) and the impact-parameter approximation is used to treat the distant collisions ($r > R_0$). Thus the correct behaviour of the ionization cross section is obtained at both low and high energies. The main difficulty of the method is that it involves choosing the correct cutoff impact parameter R_0.

All of these classical and semiclassical approximations only treat the direct knock-on ionization process. The effects of inner-shell excitation or ionization followed by autoionizing transitions have to be accounted for by independent calculations.

4-2 Quantum Theory

Thefirst quantum calculation of ionization was performed by Bethe in 1930[54], using the Born approximation. Since that time numerous quantum approaches have been carried out, most of them concerned with the ionization of neutral atoms[47]. The methods employed can be readily extended to the case of ionization of positive ions, but the theoretical procedures involved in all these calculations are very complex and lengthy. The difficulties mainly arise from the long range Coulomb potential requiring a full solution of the many-body problem in the asymptotic region. Various approximations have been developed to treat this problem. Exchange and interference between the two continuum electrons have to be taken into account. For ionization of complex ions, additional problems arise from the need to find accurate wavefunctions for the target states before and after the collision.

The most commonly used and generally accepted quantum approach to calculate electron-ion ionization is the Coulomb-Born approximation in which both the ionizing and ejected electron are described by Coulomb wavefunctions. Several versions of the Cou-

lomb-Born approach have been developed differing mainly in their approximations to treat (or not) exchange effects. Coulomb-Born type calculations are available now for a number of ion species, preferentially of hydrogenic structure[55,56]. A scaling prescription for ionization cross sections of hydrogenic ions with configurations from 1s up through 4f was given too[56,57].

The Coulomb-Born approximation has been modified to account for screening effects close to the target ion by using distorted waves instead of Coulomb waves to describe the ionizing electrons[58),59)]. On the other hand, if the charge of the target ion is neglected the plane wave Born approximation applies. This gives, involving only relatively easy computationalefforts, a good representation of the high energy behaviour of the cross section. At low energies however the cross section is underestimated, particularly for highly charged ions.

The necessity to take indirect processes like excitation-autoionization into account further complicates the theoretical treatment. Considerable complexity results from the presence of configuration interaction and intermediate coupling in the autoionizing state. For highly charged ions it is important to account for non-unit branching ratios for autoionization versus radiative decay. Usually direct and indirect ionization mechanisms are assumed to take place independently.In this case the crosssection for excitation (multiplied by the branching ratio for autoionization) is merely added to the cross section from direct ionization to yield the total ionization cross section.

4-3 Semi-Empirical Formula

In view of the very complex theoretical approaches and motivated by the need to provide reasonably accurate estimates of

unknown cross sections in a very simple fashion, several semi-empirical formulas have been proposed[60-62]. The most successful one, which has been used extensively in the calculation of plasma properties, was given by Lotz[62-64],

$$\sigma(E) = \sum_{i=1}^{N} a_i n_i \frac{\ln(E/P_i)}{E\ P_i}(1 - b_i \exp(-c_i(E/P_i - 1))), \quad --(3\text{-}3)$$

where E is the incident electron energy, P_i is the binding energy of the electrons in the i th sub shell and n_i is the number of electrons in the i th subshell. The a_i, b_i and c_i are constants determined by fitting to the measured cross sections. For most species it is sufficient to include only the 3 outer-most sub-shells. The best fit values for a_i, b_i and c_i were determined for measured cross sections and estimated for unknown cross sections and are tabulated by Lotz in the references.

The formula gives reasonable agreement with experiment for simple atoms, but rises too slowly from threshold in the case of ions. For more complex systems with electrons in d and f orbitals the agreement with experiment is poor for two reasons. Firstly, few measurements on complex systems were available when Lotz fitted his values for the a, b and c constants, and secondly the formula takes no account of autoionization from inner shells and this becomes significant for complex systems.

CHAPTER 4

THE APPARATUS AND THE EXPERIMENTAL METHOD

Two types of experimental setup are used for the measurements of alkali metal ions and alkaline earth ions, respectively. Schematic view of the crossed beam apparatus is shown in Fig.4-1 for the measurements of alkali metal ions and in Fig.4-2 for those of alkaline earth ions.

The experimental apparatus used for alkali metal ions consists of three chambers, i.e. the ion source chamber, the ion chopping chamber and the collision chamber. Singly charged ion beam produced in a thermionic emission type or a surface ionization type ion source is mass-selected by an electromagnet and focused and collimated to 1 mm diameter using several sets of electrostatic lens systems and collimator slits. A rectangular shape electron beam produced in a Pierce type electron gun collides with the ion beam at right angles. An L-shape slit scanner, which is controlled by a micro computer, is used for the measurements of the spatial distributions of both beams in the collision region.

After colliding with the electron beam, the ion beam is separated according to its charge state by a parallel plate charge state analyzer. The primary ion and the product ion are detected by a Faraday cup and a single particle detector, respectively. The beam modulation technique is used for the separation of true signals from various kinds of background signals.

For the measurements of alkaline-earth ions, the impurity emission in the ion beams produced by the surface ionization type ion source is negligibly small, and the magnetic field produced

in the mass-selector used in this study is so weak that the Ba^+ ion beam of sufficient energy (> 2 keV) can not be analyzed in the mass-selector. And to get enough ion current the path length of ion beams between the ion source and the collision region should be as short as possible. Because of the above reasons the mass-selector and the ion chopping chamber are removed and the ion source chamber is connected to the collision chamber via a gate valve.

The remaining sections in this chapter will be devoted to the detailed description of the each part of the apparatus.

4-1 Vacuum System

Each chamber is pumped separately depending upon vacuum requirements.

The ion source chamber is evacuated by a 10" oil diffusion pump with a water cooled trap. The base pressure of this chamber is 5×10^{-8} Torr and rises to $1\text{-}2 \times 10^{-7}$ Torr with the ion source in operation. The ion source chamber is connected to the ion chopping chamber through a gate valve with an ICF253 flange and a flat cross section mass analyzer tube. The chopping chamber is pumped by a 270 l/s turbo molecular pump and is capable of obtaining pressures in the 10^{-8}Torr range. This chamber is connected to the collision chamber with a 1 cm diameter by 14 cm long tube to provide differential pumping. The collision chamber, or main chamber is pumped by a cryogenic pump, whose pumping speed is 1000 l/s. The pressure during the operation of electron gun is in the order of 10^{-9}Torr.

For the measurements of alkaline earth ions, the ion source chamber is connected to the main chamber with a gate valve with an ICF70 flange and the main chamber is evacuated by a cryogenic

pump and a turbo molecular pump.

An interlock system closes all valves and shuts off all power supplies to the vacuum system automatically when sudden rise-up of the pressure or suspension of water supply occur, to prevent the breakdown of the pumping system and the glow discharge in vacuum.

4-2 Ion Source

The requirements on the ion source imposed by the experimental conditions are as follows:

i) the ion source can produce a collimated beam current of 10^{-8}A or more,

ii) the beam current and shape must be stable for periods up to several days, and

iii) the ion source must produce only the ground state ions.

In order to fulfil the above requirements, a thermionic emission type ion source and a surface ionization type ion source are used for the production of alkali metal ions and alkaline earth ions, respectively.

4-2.1 Thermionic Emission Type Ion Source.

A thermionic ion emitter is a material which, when heated in the presence of an electric field, will emit ions in a manner analogous to the way that thermionic electron emitters emit electrons.[65] This type of ion source is suitable for the species of which the ionization potential is relatively low. Therefore we chose this type for the alkali ion source. The alkali aluminosilicates ($X_2OAl_2O_32SiO_2$, X:desired element) are widely used for the thermionic ion emitters. We use the commercial Na-zeolite ($Na_2OAl_2O_32SiO_2$) to produce singly charged Na^+ ion. For K^+ ion,

the Na-zeolite has been exchanged with K using the techniques described in the literature[66].

The manner we use to make the ion emitter is as follows. The zeolite powder is placed inside a spiral made of a 0.2mm diameter platinum or tungsten wire with 6-7 windings around a needle (1mm in diameter). The spiral is heated up to 1100°C in vacuum. After proper aging time (about 5-10 hours), impurity emission from the ion emitter becomes less than 0.5% and the order of 10^{-8} A of Na^+ and K^+ can be obtained at the collision region. The life time of this emitter is about 100 hours.

The schematic view of the thermionic type ion source is shown in Fig.4-3. The spiral coated with ion emitter is placed at SP in the figure. Electrodes A, B, C and D are used for extracting and focusing the ion beam. Typical voltage applied to these electrodes for a 2 keV ion beam are given in Table 4-1.

The mass spectrum of this ion source for K^+ ion after proper aging time is shown in Fig.4-4. This spectrum shows that the impurity, most of which is Na^+, can be negligible and that intensity ratio in K^+ peaks is consistent with the isotopic ratio K^+_{39}/K^+_{41} of 13.5.

4-2.2 Surface Ionization Type Ion Source.

Thermionic emission type ion source described in section 4-2.1 is not suitable for the production of the singly charged alkaline earth ions because of their higher ionization potentials compared with those for alkali metal atoms. Therefore, a surface ionization type ion source is chosen as the alkaline earth ion source.

Atoms or molecules incident on hot metal surfaces leave the surface partly as positive or negative ions. This process is

Table 4-1. Typical Applied Voltage in the Thirmionic Emittion Type Ion Source.

Electrode	Voltage (V)
SP	+ 2000
A	+ 2015
B	+ 1965
C	+ 1830
D	0

called surface ionization[65]. This phenomenon was first observed in the case of caesium atoms on hot tungsten surfaces[67] and applied to the other alkali metal atoms and heavier alkaline earth atoms (Ca, Sr and Ba). A detailed discussion of the ionization efficiency and the other characteristics of this type of ion source will be found in Appendix A-1.

The first attempt on this type of ion source was carried out using a compact ion source with indirectly heated ionizer designed by Sakai et al.[68]

A schematic of this source is shown in Fig.4-5. The beam material in a stainless steel reservoir was heated up to 450 °C by a 0.25 mm tantalum heater placed around the reservoir. The atom vapor produced in the reservoir was led to the ionizer region through a guiding pipe made of molybdenum. The ionizer consisted of an ionizer holding pipe made of molybdenum, of which the inner diameter was 3 mm, and an ionizer which was a 0.1 mm Pt wire bundle. The ionizer was indirectly heated by a 0.3 mm tantalum heater up to 1100 °C with 200 W of power supply. The ionized particle were extracted by a extracting electrode. This electrode was made of 1 mm thick molybdenum disk with a hollow cone whose opening is 2 mm in diameter. Because this electrode was placed near the ionizer region, this part could be heated by ionizer heater up to enough temperature to emit thermal electron, which resulted in the discharge between the ionizer and the extracting electrode. To prevent this discharge, the molybdenum disc was covered with an 8 mm thick copper disk of which the thermal conductivity is very high.

This source had some weak points as follows,

i) the life time was too short (typically only a few days) because of heater burnout,

ii) the beam intensity was not enough for the ionization measurements (less than 10^{-9} A at collision region),

iii) the beam was not stable because of the discharge between the ionizer and the extracting electrode, even though the extracting electrode was covered with copper disk, and

iv) a manner to make the heater assembly was complicated.

The biggest cause of the 1st to 3rd weak points was thought that the volume of the ionizer region was so large that much power was necessary to heat it up to enough temperature for surface ionization of atoms.

Following this initial ion source test, a new ion source with directly heated ionizer was constructed with the object of obtaining increased beam current, and improved stability and simplicity of construction.

Schematic diagram of the ionizer region of the new source is shown in Fig.4-6. The design of the new ion source was based on theone by Lyon and Peart[69] except for the shape of an output slit of the reservoir. Neutral atom vapor is produced in a stainless steel reservoir which can be heated up to 550 °C by a 0.3 mm diameter tungsten heater with a heating power of 120 W. The atom beam is led to an ionizer surface through a circular slit which is 0.35 mm in width. The ionizer is a 0.025 mm thick Re ribbon which is directly heated up to 1600 °C with a power of 40 W. The effective cross section of the ionizer is about 0.2 mm^2. The advantage of this arrangement with a circular slit is that the spatial distribution of the ion beam will be axially symmetric, which is a desirable property in electron-ion crossed-beam experiments.

Schematic diagram of the ion source with the several sets of lens optics and deflector plates is shown in Fig.4-7. The ions

are extracted from the ionizer surface by some extracting electrodes. The reservoir block also works as a extracting electrode. Then ions are focused and steered by an einzel lens and deflector plates.

An ion beam of adequate current of 3-5 x 10^{-8} A at the collision region can be obtained using this new ion source. Moreover the beam produced from this source is remarkably stable and the life time is more than 1 month.

Because of high temperature of the ionizer surface, it is possible that some fraction of the produced ions include some metastable states. This problem will be discussed in Appendix A-2.

4-3 Electron Gun

A Pierce type electron gun[70] with an oxide-coated cathode whose cross section is 4 x 25 mm^2 is used to produce a rectangular and uniform electron beam. A side view of the electron gun with the collision region and the Faraday cup is shown in Fig.4-8. The electrons are extracted by a grid G with a positive potential and collimated by three sets of grounded electrodes. The beam defining slit placed at the entrance of the collision region is 3 mm in height and 15 mm in width, and the output slit of collision region is 10 mm in height and 30 mm in width. The electron beam is collected in a cylindrical Faraday cup whose inner diameter is 36 mm. The Faraday cup is coated with colloid carbon (Aqua Dag) and positively biased to prevent escape of secondary electrons.

4-4 Beam Probe

In order to get the absolute cross sections, it must be

known how the both beams collide with at the collision region, i.e. the current density profile of the both beams must be measured, as described in Chapter 1-2.

Schematic view of the beam probe used in this study with the beam crossing region and electron gun is shown in Fig.4-9.

An L-shape shutter with a narrow horizontal slit of 0.1 mm height can move vertically with the stroke of 20 mm. The spatial distributions are evaluated by measuring the transmission of beam current through the slit in the shutter as a function of slit position. A stepping motor and a micrometer drive system outside the vacuum are used to accurately position the shutter under computer control. The computer records the profiles of the both beams and performs an on-line calculation of the required integrals in eq (1-10) to obtain the form factor. (See Chapter 4-8)

As will be shown in Chapter 5-4, the form factor corresponds to the effective beam height of the electron beam. In this study, an L-shape slit scanner, which measures the current density profile of both beams at some distance from the real collision region, is used. Therefore, the measured form factor may contain some error.The discussion of this problem will be given in Chapter 5-4.

4-5 Charge State Analyzer

The analyzer is a 45 parallel plate analyzer with three exit slits such that, when a beam of a given E_i/q passes through the slit designated the A^+ exit slit, beams of $E_i/2q$ and $E_i/3q$ simultaneously passes through the other exit slits, designated the A^{2+} and A^{3+} exit slits, respectively. The analyzer is completely enclosed to prevent entering of stray particles and is equipped with three guard plates to minimize effects due to

fringing fields. A set of vertical deflection plates is placed at the entrance slit to check the transmittance of ion beam, as will be discussed in Chapter 5-3.2.

A drawing of the analyzer appears in Fig.4-10.

4-6 Single Particle Detector

In the measurements for alkali ions, a direct incident type detector, which is shown in Fig.4-11, was used. It consists of a channel electron multiplier (Ceratron EMT6081B, MURATA) and an entrance aperture, whose diameter was 10 mm, which is the same as that of the entrance cone of the multiplier. The product ions were accelerated with a voltage of about 3.5 kV before entering the entrance cone. The potential of the entrance aperture was adjusted so that the counting efficiency of the ion counter gave the maximum value.

After the measurements for alkali ions, a drop of output gain of the multiplier was observed. This was thought to be due to the change of the condition of the entrance cone surface of the multiplier because the alkali atoms are very active. And there was a possibility that in the alkaline earth measurements, the surface condition of the multiplier would also change with time. For this reason it was decided to use the single particle detector with a secondary electron converter developed by Rinn et al.[71]

This new detector is shown in Fig.4-12. It consists of a Ceratron and two electrodes; the converter plate 'P' made of a copper-beryllium metal sheet and a repeller electrode 'Rep' in front of the Ceratron funnel.

The incident ions hit the converter plate P. In order to obtain a high secondary-electron yield, the converter is inclined

relative to the ion-beam axis with an angle of 45° and is made of a copper-beryllium metal sheet. Secondary electrons are extracted from P and focused onto the Ceratron entrance funnel. The repeller electrode Rep is necessary for a proper adjustment of the electric field in front of the Ceratron funnel. In addition, a grid is installed across the entrance part of the ion beam to conserve the rotational symmetry of the extraction field for the secondary electrons. The optimum voltages for high detection efficiency are also indicated in Fig.4-12 for the respective electrodes.

This detector has some advantages;

(1) larger cross section of sensitive area than that of the entrance funnel of the Ceratron,

(2) reduction of the damage of the surface of the Ceratron by the impinging ions, and

(3) high average number of secondary electrons released by an incident ion from the converter plate, which results in the high detecting efficiency.

A proper voltage is applied between the output end of Ceratron and the electron collector to extract the electron pulse effectively. This method is reported to enlarge the pulse height of the output pulse[72].

The pulse-counting electronic chain is shown in Fig.4-13. An output pulse of electronic-charge is converted to voltage pulse by a load register (designated as 'R' in the Fig.4-12)and amplified and shaped to a pulse whose pulse-height is a few Volts. Then a single channel analyzer (SCA) cut off the low level electronic noises and generates a TTL pulse, which is triggered by an input pulse. The cut-off voltage in SCA (lower discriminator level) is set at 0.2 V, which is high enough to remove the

electronic noises and low enough to pass the pulses from the product ion detector through the SCA. The pulses accepted by the SCA are fed to the data acquisition system, which will be shown in Chap.4-9.

4-7 Beam Chopping Technique.

The signals detected by a product ion detector consist of the true signals S_T, the background signals caused by ion beam S_i (mainly due to charge stripping collisions of the target beam on residual gas atoms and molecules and on the slits), background signals caused by electron beam S_e, and dark noise of the secondary electron multiplier S_B. As mentioned in chapter 2-4, the double beam chopping technique is used in this study to separate the true signals from the background signals.

A pulsing sequence for the double beam chopping method is shown in Fig.4-14. The both beams are chopped squarely and the phase differs by a 1/4 period each other. The signals recorded in phase-1 to phase-4 are, respectively, the sum of S_e and S_B in phase-1 (C_1), the sum of S_T, S_i, S_e and S_B in phase-2 (C_2), the sum of S_i and S_B in phase-3 (C_3), and S_B in phase-4 (C_4). So the each signals (S_T, S_i, S_e and S_B) can be obtained by calculating from the signals in each phase as follows,

$$S_T = (C_2 + C_4) - (C_1 + C_3)$$

$$S_i = C_3 - C_4$$

$$S_e = C_1 - C_4$$

$$S_B = C_4 .$$

The signalcounting for each phases are controlled by applying the gate control pulses on the scaler. The output pulses from the product ion detector are counted when the gate control pulse is 'ON', and not counted when the gate control pulse is

'OFF'. The duration of the gate control pulse is chosen to be slightly shorter than a 1/4 period of the beam chopping, as shown in Fig.4-14, to avoid a difficulty that occur during the transient time caused by the incomplete rizing and shutting of the beam current.

When the background signals due to electron beam S_e is negligibly small compared to S_i, the single beam chopping method can be used. A pulsing sequence for single chopping mode is shown in Fig.4-15. In this mode, only the electron beam is chopped. The signals in phase-1 in Fig.4-15 is the sum of the S_T and S_B', and those counted in phase-2 is S_B', which in its turn includes S_i, S_e and S_B in the double chopping mode. So S_T and S_B can be obtained by a simple subtraction as follows,

$$S_T = C_1 - C_2$$

$$S_B' = C_2 \ .$$

In the present study, the counting rate of S_e is a few count per second, being negligibly low in the measurements for large cross sections, i.e. for large count rate of S_T, which is the case where the single beam chopping method is satisfactory. However, when the count rate of S_T is as low as that of S_e as in the measurements at the threshold region, most of data are taken using the double beam chopping method.

An electronic circuit system, which can generate the beam control pulses and the gate control pulse, was designed and constructed by the author himself in order to realize the beam chopping method. The detail of this system is given in Chapter 4-9.

4-8 Micro-Computer System to Measure The Form Factor

To determine the form factor, it is necessary to measure the

vertical current density profile of both beams by a L-shape slit board which must be able to be controlled precisely from the outside of the vacuum. A stepping motor which is controlled by a micro-computer (NEC, PC-8801mkIIsr) is used in the present study.

A block diagram of this system is shown in Fig.4-16. A stepping motor is connected to a linear-motion inducer whose stroke is 20 mm. The inducer can convert a rotative motion in the atmosphere to a linear motion in the vacuum. Minimum step angle of the stepping motor is 1.8 deg, and the one rotation of the inducer corresponds to 1 mm linear motion in vacuum, so one step of the stepping motor corresponds to 0.005 mm of the linear motion of the slit board. In our device, the sampling pitch of the density profile is 0.1 mm, so the number of step of the motor for each sampling is 20.

The ion and electron current passed through the slit board are collected by each Faraday cups, which are connected to the pico-ampere meters (TAKEDA RIKEN model TR-8641 and KEITHLEY model 485). The analogue-voltage outputs from each electrometers are converted to digital signals by Analogue-to-Digital Converter (ADC) and stored in the memory in a micro-computer and the density profiles of the both beams are displayed in a graphic monitor. The form factor is then calculated by the micro-computer using the stored numbers.

The sequence of the measurements of the form factor is controlled by the micro-computer as follows,

(1) the parameters of the micro-computer are initialized,
(2) the slit board goes up to the upper limit position where the slit board completely interrupt the both beams,
(3) the slit board goes down to the position of the first sampling,

(4) the current signals are converted to theanalogue voltage signals by the electro-meters,

(5)the analogue signals are digitalized by the ADC and stored in the memory, and the recorded data are displayed on a graphic monitor,

(6) the slit board goes down to the next sampling position,

(7) repeat the above procedure (4) to (6) until the sampling number becomes the preset number (normally 100 times),

(8) when the above iteration finishes, the slit board goes down to the lower limit position where the slit board does not interrupt the both beams at all,

(9) micro-computercalculates the form factor and saves the data to a floppy disk.

The uncertainty in the form factor measurements will be discussed in Chapter 5-8.

4-9 Data Acquisition System.

To realize the beam chopping method, an electronic circuit system has been designed and constructed by myself. The functions of this system are as follows,

(1) this system can be used in both the double chopping method and the single chopping method,

(2) the chopping frequency can be varied from 31 Hz to 4 kHz in order to check the background modulation effect (see Chap.2-4),

(3) the timing of the gate 'ON' and 'OFF' of the gate control pulse can be variable,

(4) the real-time calculation of S_T, S_i, S_e and S_B can be done and the results of the accumulation can be displayed individually,

(5) the data accumulation time can be preset with a crystal-controlled timer,

(6) the maximum amplitude of the output pulses for beam chopping is 500V, which is large enough to chop both beams completely,

(7) the chopping pulses are isolated from the ground potential in order to be applied to any floated electrodes, and the possible isolation voltage is about 2 kV.

A block diagram of this system is shown in Fig.4-17. This system consists of a control pulse generator unit, a timer unit, a multiplexer (control) unit, a counter unit and a chopping pulse driver unit. All of the circuit, except for the chopping pulse driver unit, is composed of TTL and C-MOS IC. Circuit diagrams of each unit are bound into this thesis as Appendix B.

In the control pulse generator unit, an ion control pulse (designated as 'A' in the figure) and an electron control pulse ('B' in the figure) and a gate control pulse ('C' in the figure) are generated using a crystal-controlled oscillator and some logic circuits. The chopping frequency can be set to 31Hz, 62.5Hz, 125Hz, 250Hz, 500Hz, 1kHz, 2kHz and 4kHz. The delay and the width of the gate control pulse can also be varied.

The pulses A, B and C are fed to the multiplexer unit. This unit generates the counter control pulses, i.e. 'counter up/down' pulses, and 'count inhibit' pulses, for each counters for S_T, S_i, S_e and S_B, by the logic calculation using the pulse A, B and C. For example, a counter up/down pulse and a count inhibit pulse for S_T counter are produced by the calculation as,

S_T(up/down) = (A AND B) + ((not A) AND (not B))

S_T(inhibit) = (not C)

The pulses obtained by these logic calculations are shown in Fig.4-18.

These control pulses are fed into the counter unit, which consists of 4 up/down counters and 6-digit LED display. The signal pulse from the product ion detector is added or subtracted according to the control pulses.

Control pulses A and B generated in the control pulse generator unit are also fed into the chopping pulse driver unit. In this unit, these pulses of TTL level (0 - 5 V) are amplified to the voltage high enough to chop the electron and ion beams completely. The maximum output voltage is 500 V. These pulses are isolated from the ground potential by a photo-coupler (HP-6N135), and can be applied to any floating electrodes. The maximum isolation voltage is 2000 V from the ground potential.

The data acquisition time is controlled by the timer unit, which consists of a crystal-controlled clock, a time set swich, and a digital comparator. The comparator compares the time indicated by the clock with the preset time on the switch, and when the clock time coincides with the preset time, a 'stop' pulse is generated and fed to the multiplexer unit, then the system stops. The preset time can be set from 1 second to 99 hour 59 minutes 59 seconds.

CHAPTER 5

CROSS SECTION MEASUREMENTS AND SYSTEMATIC CHECKS

In this chapter, the method to determine the quantities in equation (1-10) and the various routine daily measurements will be discussed. Some systematic checks for the absolute measurements are also given.

5-1 Routine Measurements.

The data-taking sequence for the experiments begins with tuning of the ion beam. This starts with heating up the ion source to an adequate temperature. It takes about 10 minutes for the thermionic emission type ion source and about 30 minutes for the surface ionization type ion source. Then the beam is tuned by adjusting several sets of deflectors and einzel lenses to obtain the maximum currents into the in-line Faraday cup in the parallel-plate charge state analyzer. Then the ion beam is deflected and collected in the final Faraday cup. Some adjustments are done using deflectors and an einzel lens in the collision chamber,

(1) to insure that the primary and the product ion beam is fully collected in the final Faraday cup and the product ion detector, respectively, (see chapter 5-3.2)

(2) to obtain the signal to background ratio of about 5 to 10 at the impact energy where the cross section has the maximum value.

When the count rate of product ion exceeds 10^4 cps and 3×10^3 cps in the measurements of alkali ions and alkaline earth ions, respectively, the ion current is reduced in order not to be affected by the dead time of the counting electronics. (see chap-

ter 5-5)

At this point, the beam is said to be tuned. During a data accumulation, only small adjustments of the lens voltage in the ion source chamber are made to keep the ion current optimum.

Then, the channel electron multiplier (CEM) operation is checked by observing a pulse height of output signal by an oscilloscope. Various instrumental checks are performed, including checking the amplifier gain and the lower level discriminater in SCA.

Following these initial measurements and checks the data accumulation sequence begins. Typical integration time, which depends on the cross section, is about 600 to 1200 sec at the threshold region and 30 to 120 sec at the higher energy region. At each energy, a few times of the integrations are carried out. The beam profiles are measured at every energy and the form factor for the every electron energy is calculated. This sequence is repeated until the impact energy reaches about 1000 eV.

A typical data run includes cross section measurements at 80 to 100 energies and takes approximately 10 to 15 hours to complete, not including the time required to tune the ion beam and complete the various pre-measurements, which generally required a few more hours to the actual data accumulation time.

The data accumulation as described above is repeated a few times to check the reproducibility of the measured cross sections.

5-2 Cross Section Calculation

A cross section is calculated by equation (1-9) using the measured quantities.

The electron current is measured directly from the ampere-

meter because the electron current is very stable with time. However, the ion current changes with time (in the worst case, the changes are about 20 to 30 % in 60 to 120 seconds). So it is necessary to obtain the average current over the accumulation time. A current integrator for the ion beam was designed and made by the author. A block diagram of the integrator is shown in Fig.5-1. By dividing the integrated current which is displayed on the integrator by the integration time, the average current is obtained.

The counting rate R is obtained from the results of the calculation in the data acquisition system described in chapter 4-9. The R (count/second) is calculated using the accumulated count N during the integration time T as follows,

$$R = (N/T) \times A \times 100/W ,$$

where A = 4 in the double chopping mode and A = 2 in the single chopping mode, and W is the width of the gate control pulse, when the interval of each phase in figure 4-14 and 4-15 is represented as 100.

The form factor is directly measured using the manner as described in chapter 4-8. The beam velocities v_i and v_e are calculated from each acceleration voltages and the masses of electron and ion. The detection efficiency D is assumed to be unity in this study. The consistency of this assumption in the results of present work will be given in chapter 5-6.

Using these measured quantities, the absolute ionization cross sections can be calculated. The following sections in this chapter will be devoted to an overview of the possible systematic effects and some measurements for the check.

5-3 Beam Collection

To obtain the absolute ionization cross section from the measured quantities, it is essential that all particles of the electrons and the ions existing in the collision region are completely collected and accurately measured. Various measurements are done to check the complete collection of the both beams, including the product ion beam.

5-3.1 Electron Beam Collection

A problem concerned to the accurate measurements of a large electron current with a large cross section is commonly encountered in the experiments whose purpose is to get absolute cross sections. The openning of the electron collector is 10 mm in height and 30 mm in width, which is much larger than the beam defining slit placed at the entrance of the collision region which is 3 mm in height and 15 mm in width. The complete suppression of the secondary electrons from the collector surface was the biggest problem in this work. The electron collector is positively biased to prevent the escape of the secondary electrons. Grid wires in front of the electron collector, as shown in figure 4-8, are grounded to avoid the distortion of the electric field in the collision region. The bias voltage of the collector is normally set to +5V during the experiment.

Moreover, the surface of the collector is covered with the Aqua Dag (Colloid Carbon) to suppress the secondary electron emission due to the incident and the scattered electrons.

5-3.2 Ion Beam Collection

To verify the analyzer transmittance of the ion beam, several methods are used. The first is the comparison between the current measured at the in-line Faraday cup in the charge state

analyzer and the final Faraday cup. In most of this test measurements, the agreement is quite well. If it is not so well, then the further adjustment of the deflector and the lens system are done until the agreement becomes quite well.

The next test is done by scanning the ion beam vertically and horizontally by scanning the applied voltage of the vertical deflector placed just before the analyzer entrance aperture and the analyzer retarding voltage, respectively, and the beam currents passed through the final ion collector and the count rate detected by the product ion detector is measured as functions of the scanning voltages. The results of these measurements are shown in Fig.5-2 for the vertical scanning and in Fig.5-3 for the horizontal scanning. The insurance for the perfect transmission lies in the flatness of the transmitted currents at their peaks. It is true that the flatness on the top of these curves are not the proof of 100% transmission in itself. However, in order to produce a flat topped scan for an imperfectly transmitted beam scan, it must have an uniform horizontal current distribution. In view of the fact that our beam has a circular cross section and is collimated to 1 mm in diameter at the entrance of collision region, while the width of the exit slit of the analyzer is 8 mm, this is extremely unlikely. Therefore, the top-flatness in these measurements is believed to be the evidence for the full transmission.

In addition to the analyzer transmission, we have verified that no secondary electrons escape the final Faraday cup by variation of the bias voltage applied to the Faraday cup. Normally the bias voltage is set at +15V.

The collection efficiency of the product ion detector, i.e., the detection efficiency D in equation (1-10) will be discussed

in chapter 5-6.

5-4 Form Factor Measurements.

As shown in chapter 1-2, the form factor F is defined by

$$F = \frac{\int i_i(z)dz \int i_e(z)dz}{\int i_i(z) i_e(z)dz} \quad \text{---------- (5-1)}$$

This integration is approximated as follows,

$$F = \frac{(\sum_n i_{in}\Delta z)(\sum_n i_{en}\Delta z)}{\sum_n (i_{in} i_{en}\Delta z)}$$

$$= \frac{\Sigma i_{in} \Sigma i_{en}}{\Sigma(i_{in} i_{en})} \Delta z, \quad \text{----------(5-2)}$$

where Δz represents the interval of the current sampling, and i_{in} and i_{en} are the linear current densities along the z axis at nth sampling point, and they have a dimension of current/length. The measurable quantity is not the linear current density i but the current i' passed through the slit of height S. So the equation (5-2) can be rewritten as,

$$F = \frac{\Sigma i'_{in} S \; \Sigma i'_{en} S}{\Sigma(i'_{in} S \cdot i'_{en} S)} \Delta z$$

$$= \frac{\Sigma i'_{in} \; \Sigma i'_{en}}{\Sigma(i'_{in} i'_{en})} \Delta z \quad \text{---------- (5-3)}$$

It must be noted that the form factor does not depend on the slit height S, but the slit height must be small enough compared to the beam height for the approximation done in equation (5-2).

The form factor is measured and calculated using the equation (5-3) by the computer described in chapter 4-8.

Form factor represents the non-uniformities of the both

beams at the interaction region. So the change of beam shape with time can be a source of error. In the present study, the electron beam is stable but the ion beam current is sometimes unstable with time. Hereafter in this section, the influence of this unstability of the ion beam on the form factor will be discussed.

When we consider the current density profiles of both beams as shown in Fig.5-4, i.e. a narrow ion beam is completely superimposed on the top-flat region of electron beam, the form factor is calculated as

$$F = \frac{\Sigma i'_{in}\ \Sigma i'_{en}}{\Sigma (ui'_{in})} \Delta z$$

$$= \frac{\Sigma i'_{en}}{u} \Delta z \ , \qquad (5\text{-}4)$$

where u is the current of the electron beam at top flat region. This results shows that, in the ideal case as shown in figure 5-4, the form factor does not depend on the density profile of ion beam, so the unstability of the shape of ion beam has no influence on the form factor. And the form factor, which has a dimension of length, corresponds to the effective height of the electron beam.

But to make the electron beam which has such an ideal density profile as described above is not possible. A typical example of the measured current density profile of both beams is shown in figure 5-5. Although a perfect top-flatness can not be obtained, the electron has an approximately top-flat current density at the region where it crosses with the ion beam. Therefore an error due to the unstablity of ion beam is minimized by

having the beam arrangement as shown in figure 5-5.

As shown above, the effective electron beam height can be estimated from the form factor measurement and, in this work, it varies 4 mm to 5 mm depending on the impact energy, whereas the height of the beam defining slit of the electron gun is 3 mm. This fact suggests a beam spread due to a space charge effect or the other reason. The beam spread due to the space charge effect is estimated to be less than 1 % at the collision center under the present experimental conditions, and it does not explain such a large spread. So the sauce of this spread is concluded to be due to the other reason, mainly due to the lens focusing effect.

As an L-shape slit is used in the present work, the measured profiles are those measured at the 2 mm downstream from the collision center. Therefore, it is necessary to interpolate the form factor at the collision center from the measured density profile. From the discussion in the last paragraph, this correction is done by the linear geometrical interpolation, as shown in Fig.5-6 for all of the results presented in this thesis. 'F_D' in the figure is the effective beam height at the downstream from the collision center, i.e. the form factor measured using the L-shape slit, and 'F' is that at the collision center. F is calculated as

$$F = A(F_D - S)/B + S \quad \text{----------(5-5)}$$

where the 'S', 'A' and 'B' are the height of the entrance slit, the distance from the entrance slit to the collision center and the slit board, respectively. This correction factor is within a few percent. The uncertainty due to this interpolation will be discussed in chapter 5-8.

5-5 Counting Rate

The product ion detector and the counting electronics have an overall dead time T, i.e., after one ion has hit the detector, the time until the next ion can be counted is at least T. If another ion hits within the dead time T after an initial pulse, the next ion can not be counted. For a given incident flux of ions J, the Poisson probability for time intervals t between two successive ions where t is larger than T is given by

$$P_0(JT) = \frac{(JT)^0}{0!} \exp(-JT) = \exp(-JT) \quad . \quad \text{----------(5-6)}$$

This also gives the probability D that the second ion can be counted, i.e., the detection efficiency D, is,

$$D = Z / J = \exp(-JT) \quad , \quad \text{----------(5-7)}$$

where Z is the observed count rate. Under the condition of small incident ion fluxes J, i.e., JT is much less than unity, D can be approximated by D = 1 - JT, and such condition that Z is nearly equal to J holds at low count rates, therefore D is,

$$D = 1 - ZT \quad . \quad \text{----------(5-8)}$$

For the direct incident type product ion detector, the dead time is estimated to be less than 1×10^{-6} second from the observation of the pulse shape by an oscilloscope. In this case, when the count rate reaches 10^4 count per second, the detection efficiency D becomes 99 %. So for the direct incident type detector, special attention is paid so that the count rate does not

exceed 10^4 cps.

For the detector with the secondary electron converter, the dead time is measured to be approximately 5×10^{-6} second. Therefore, in this case, the ion current is reduced by adjusting the lens optics in the ion source chamber, when the count rate exceeds 3×10^3 cps.

5-6 Detection Efficiency

In the present work, the primary is the singly charged ion and the product is the doubly or triply charged ion. The detection efficiency D of the product ion detector for the doubly and triply charged ion must be known, because the detection efficiency depends on both the energy and the charge state of incident ion. However, the doubly and triply charged ions are not available using the thermionic emission type and the surface ionization type ion sources. Therefore the detection efficiency is not experimentally determined but is assumed to be unity. The consistency of this assumption is insured by the following reasons,

(1) the present results are in good agreements with the reliable data of the crossed-beam measurements by previous workers within the experimental error, if the detection efficiency is assumed to be unity,

(2) for the direct incident type detector, the entrance aperture is adjusted so that the detection efficiency gives the maximum value (see chapter 4-6),

(3) for the detector with the secondary electron converter, the electron yield from the CuBe surface is reported to be about 10 for 10 keV Ar^{+1} and about 7 for 10 keV $Xe^{1+71)}$, which indicate that the all positive ions with adequate kinetic energy probably release enough secondary electrons to give a

high detection efficiency, moreover,

(4) the counting rate is not so sensitive to the voltage applied between the converter plate and the Ceratron entrance, which is used for the acceleration of electron to the Ceratron entrance, and

(5) a care is taken so that the count rate does not exceed 10^4 cps for the direct incident type detector, and 3×10^4 cps for the detector with converter, which results in the counting failure of the signals as shown in chapter 5-5.

5-7 Consistency Check of Cross Section.

In this section, some measurements of the dependence of the deduced cross sections on several experimental parameters will be given. The checked parameters are the ion current I_i, the electron current I_e, the ion velocity v_i and the parameters for the data acquisition system. Typical results of the checking tests are illustrated along the following items. These checking tests are done by measuring the single ionization cross section for Sr^+.

(1) Ion Current Dependence.

In Fig.5-7, the cross sections as functions of the ion current is shown at the impact energy of 70 and 200 eV. At both energies, the results is shown to be independent of the ion current.

(2) Electron Current Dependence.

The cross section dependence on the electron current is shown in Fig.5-8. The cross section is shown to be independent of the electron current from the figure.

(3) Ion Velocity Dependence.

The dependence of cross section on the ion energy, which is

proportional to the square of ion velocity, is measured and the results are shown in Fig.5-9. In this energy region, cross section does not change with the ion energy as can be seen in the figure. In the present work, ion beams with 2 keV and 3 keV energy is used for the measurements of alkali-metal ions and alkaline earth ions, respectively.

(4) Dependence on Parameter of Data Acquisition System.

Several checks of the parameter of the data acquisition system are done. Checked parameters are the chopping frequency, and the width 'W', where either of the start timing 'At' or the end timing 'Re' of the gate control pulse is varied.

Results for the cross section dependence on the chopping frequency are shown in Fig.5-10. The measured cross sections are plotted as a function of chopping frequency from 31 Hz to 2 kHz. The cross sections at the frequency from 31 Hz to 250 Hz show almost the same value within the counting statistics, however, those at the frequency higher than the 500 Hz show larger values. This change is thought to be due to the inaccuracy of ion current measurement which may occur at such high frequency that the electronics of the amperemeter can not follow. In the present work, the data are taken at the frequency of 125 Hz.

The measured count rate as a function of the gate width W is shown in Fig.5-11, where 'At' is fixed to 13 and 'Re' is varied. Linear relation between the count rate and the gate width is observed and the extraporated count rate at the zero gate width seems to be zero, which is the desired results.

The measured count rate is shown in Fig.5-12 as a function of the gate width where, 'Re' is fixed to 95 and 'At' is varied. The linear relation breaks at the gate width wider than 80 %, however, the extraporated count rate indicates zero value. The

reason of the break-down of the linearity is due to the noise of electronics generated by the chopping pulse driver which occurs at 'At' = 0.

Taking into account of the above results, the data are taken at 'At' = 10 to 15, 'Re' = 95 to 98 and 'W' = 80 to 85, throughout the present work.

5-8 Experimental Uncertainty.

All statistical uncertainties are quoted at the 68 % confidence level (68% CL), corresponding to one standard deviation of the mean. Where systematic uncertainties of a nonstatistical nature occur, an effort has been made to assess these uncertainties at a confidence level consistent with the statistical 68% CL. Where different uncertainties are judged to be uncorrelated, they are combined in quadrature to give a total uncertainty.

The counting statistics depends on the experimental conditions, i.e., the beam currents, the impact energy, the cross section, the signal to background ratio and others, however, it is estimated to be less than 1 % for most of the data point except for the data at the threshold region.

The measurements for alkali metal ions were done in the early stage of the present work. At that time, as the current integrator was not used, the ion current I_i could not be measured accurately. Therefore, the results for Na^+ and K^+ includes larger uncertainties than those for Sr^+ and Ba^+.

Table 5-1 and 5-2 list the sources of uncertainty and their estimations in the results for alkali ions and alkaline earth ions, respectively.

Table 5-1. Estimated Experimental Uncertainties in Alkali Measurements.

Source of uncertainty		Uncertainty (±%)
Counting statistics		(depends on the counting rate)
Systematic uncertainties		
Electron current	: I_e	3.
Ion current	: I_i	10
Ion velocity	: v_i	1
Form factor	: F	+1,-7
Detection efficiency	: D	+0,-5
Signal count rate	: R	negligible
Total quadrature sum of systematic uncertainties		+12.6 -11.7

Table 5-2. Estimated Experimental Uncertainties in Alkaline Earth Measurements.

Source of uncertainty		Uncertainty (±%)
Counting statistics		(depends on the counting rate)
Systematic uncertainties		
Electron current	: I_e	3
Ion current	: I_i	3
Ion velocity	: v_i	1
Form factor	: F	+1,-5
Detection efficiency	: D	+0,-5
Signal count rate	: R	negligible
Total quadrature sum of systematic uncertainties		+6.7 -6.6

CHAPTER 6

RESULTS AND DISCUSSION - SINGLE IONIZATION

In this chapter, the results of single ionization cross sections are presented and discussed. Experimental results are compared with previous crossed-beam results and the theoretical calculations except for the Sr^+ results, whose theoretical cross sections are not available up to now. The results for Na^+ and K^+ have already been published[73] and this paper is bound into this thesis as Appendix-C.

6-1 Na^+ Single Ionization.

6-1.1 Discussion of Cross Section.

The single ionization cross section for Na^+ is shown in Fig.6-1 as a function of electron energy. Present results are in good agreement with the previous crossed-beam data of Peart and Dolder[74] and Hooper et al.[75] within the mutual experimental uncertainties. Also shown in the figure is semiempirical Lotz calculation, which gives the estimation of the direct ionization of the 2s and 2p electrons.[63] The experimental results and the Lotz calculation are in good agreement, which suggests that, in Na^+ single ionization, only the direct ionization of the 2s and 2p electrons occurs.

A numerical list of the present results is given in Table 6-1 together with the total uncertainty.

6-1.2 Comparison with Theory.

Figure 6-2 shows comparisons of the present experimental results with the theoretical results by Younger[76] and Moores[77].

Table 6-1. Numerical List of Na^+ Single Ionization.

Impact Energy (eV)	Cross Section ($x10^{-17}cm^2$)	Uncertainty (±%)
45	0.00	----
50	0.05	50
55	0.21	+33, -32
60	0.40	+16, -15
65	0.60	+14, -13
70	0.88	+14, -13
75	1.05	+13, -12
80	1.33	+13, -12
85	1.51	+13, -12
90	1.51	+13, -12
95	1.73	+13, -12
105	1.87	+13, -12
115	2.00	+13, -12
125	2.13	+13, -12
135	2.29	+13, -12
145	2.30	+13, -12
155	2.45	+13, -12
165	2.50	+13, -12
175	2.48	+13, -12
195	2.58	+13, -12
215	2.61	+13, -12
225	2.67	+13, -12
255	2.46	+13, -12

Table 6-1. (Continued.)

Impact Energy (eV)	Cross Section ($x10^{-17}cm^2$)	Uncertainty (±%)
295	2.64	+13, -12
335	2.58	+13, -12
365	2.41	+13, -12
395	2.46	+13, -12
445	2.23	+13, -12
495	2.39	+13, -12
595	2.22	+13, -12
695	2.14	+13, -12
795	2.11	+13, -12
895	1.98	+13, -12
1995	1.73	+13, -12
1195	1.68	+13, -12
1395	1.58	+13, -12

Moores calculated the cross section using the Coulomb-Born approximation without exchange, including the contributions from direct ejection of both the 2s and 2p electrons. This calculation overestimates the cross section about 40% near the maximum, and the agreement between the experiment and the theory is poor especially for the lower energy region, although, the agreement seems to become better at higher energies.

Younger calculated the cross section using the distorted-wave Born-exchange approximation at the incident electron energy range from one to three times of the threshold energy. This calculation includes the direct ejection of the 2s and 2p electrons, but does not include the indirect processes such as excitation-autoionization. This results also overestimates the cross section about 30 to 50%.

6-2 K^+ Single Ionization.

6-2.1 Discussion of Results.

The results for single ionization of K^+ are shown in Fig.6-3, together with the results of Peart and Dolder[74] and Hooper et al.[75] Although, our results and those of Peart and Dolder are in good agreement, results of Hooper et al. are about 13% smaller than ours in the energy region where the cross sections show their maximum. A curve by Lotz calculation, which includes contributions by both the 3p and 3s electrons, is also shown in Fig.6-3. The values of cross section are listed in Table 6-2 with the experimental uncertainties.

In our results an abrupt rise is observed near the threshold, which is attributable to the excitation-autoionization of K^+. Aizawa et al.[78] studied the autoionizing states of K^+ in the ejected electron spectra resulting from low energy K^+ + He colli-

Table 6-2. Numerical List of K^+ Single Ionization.

Impact Energy (eV)	Cross Section ($x10^{-17}cm^2$)	Uncertainty (±%)
30	0.00	----
32	0.18	80
35	1.51	+16, -15
40	6.14	+13, -12
45	8.13	+13, -12
50	9.02	+13, -12
55	9.08	+13, -12
60	9.16	+13, -12
65	9.34	+13, -12
75	9.52	+13, -12
85	9.40	+13, -12
95	9.58	+13, -12
105	9.68	+13, -12
115	9.50	+13, -12
125	9.77	+13, -12
135	9.12	+13, -12
145	8.97	+13, -12
155	8.86	+13, -12
175	8.50	+13, -12
195	8.23	+13, -12
215	7.77	+13, -12
235	7.40	+13, -12
255	7.13	+13, -12

Table 6-2. (Continued.)

Impact Energy (eV)	Cross Section ($x10^{-17} cm^2$)	Uncertainty (±%)
275	6.66	+13, -12
295	6.57	+13, -12
325	6.10	+13, -12
355	6.01	+13, -12
395	5.83	+13, -12
445	5.18	+13, -12
495	4.80	+13, -12
545	4.42	+13, -12
595	4.14	+13, -12
645	3.86	+13, -12
695	3.87	+13, -12
795	3.41	+13, -12
895	3.02	+13, -12
995	2.93	+13, -12
1195	2.55	+13, -12
1395	2.27	+13, -12
1595	1.98	+13, -12

sions. Typical spectra is shown in Fig.6-4. They identified three groups of autoionizing states, which correspond to the $K^+(3s3p^6nl)$, $K^+(3s^23p^4nln'l')$ and $K(3p^5nln'l')$. Decay from the first and the second autoionization states leads to the production of K^{2+} ion. Core excited autoionizing states are situated ranging from 5.28 eV (K^+ $3s3p^64s$ ^1S) to 10.81 eV (K^+ $3s3p^64d$ ^1D) above the ground K^{2+} (J=3/2) state. Doubly excited autoionizing states are from 11.29 eV (K^+ $3p^4(^1D)4s^2$) to 12.88 eV (K^+ $3p^4(^1D)3d4s$) above the ground K^{2+} state. The positions of the lowest core excited and doubly excited states are indicated by arrows in Fig.6-3.

6-2.2 Comparison with Theory.

Comparison of the present results with the calculation by Younger[79] is shown in Fig.6-5. Younger calculated the cross section using the distorted-wave Born-exchange approximation at the incident electron energy range from one to five times of the threshold energy. This calculation includes the direct ejection of the 3s and 3p electrons, but does not include the indirect processes such as excitation-autoionization.

The agreement between the experiment and the distorted-wave calculation is rather good in magnitude, but it is poor in shape. The distorted-wave cross section shows more rapid rise near the threshold region and the energy where it has a maximum value is lower than the experimental results.

The theoretical estimation of the contribution of indirect processes in K^+ is not available up to now.

6-3. Results and Discussion of Cross Section for Sr^+ Single Ionization.

The experimental results of single ionization cross section for Sr^+ are shown in Fig.6-6 and their numerical values are listed in Table 6-3. Also shown in the figure are the crossed-beam results by Peart and Dolder[80]. An abrupt rise in the cross section curve is observed at an impact energy about 21 eV. An additional enhancement is found at about 32 eV in the present result, whereas the results of Peart and Dolder do not have this structure and they have another structure at about 50 eV, which has not been observed in the present results. Our results are 15 to 20% larger than those of Peart and Dolder at low impact energy, but 10 to 20% smaller at impact energies higher than 70 eV.

The abrupt rise at 21 eV suggests the onset of autoionization. This idea is supported by the theoretical calculation by Hansen[81], in which he reported the autoionizing levels in Sr^+ to be 21.60 eV and 27.13 eV for $4p^5 4d(^3P)5s(^2P)$ and $4p^5 4d(^1P)5s(^2P)$ states, respectively. Experimental results indicate that only the former transition is significant. These autoionizing levels are schematically shown in Fig.6-7 together with some other levels which can contribute to the single ionization. The position of the additional increase at 33 eV observed in the present study is near the 4p-ionization threshold energy 35.8 eV[82], therefore, this increase may be the contribution of the direct ionization of the 4p electron and/or 4p-excitation to the autoionizing levels. Dolderand Peart reported that the small hump in their results at about 50 eV are probably due to the contribution from the direct inner-shell ionization. The binding energies of the inner-shell electron in Sr^+ are 35.8 eV and 57.5 eV for the 4p and 4s electrons, respectively, according to ref.82), therefore the small hump observed in the results of Dolder and Peart can not be explained as a contribution from the inner-shell ionization.

Table 6-3. Numerical List of Sr^+ Single Ionization.

Impact Energy (eV)	Cross Section ($x10^{-17}cm^2$)	Uncertainty (±%)
11	0.00	----
12	1.31	10
13	1.52	9
14	2.53	8
15	3.90	7
16	5.30	7
17	7.18	7
18	8.03	7
19	8.92	7
20	9.50	7
21	10.26	7
22	11.86	7
23	14.05	7
24	16.66	7
25	20.05	7
26	24.64	7
27	26.30	7
28	26.94	7
29	26.84	7
31	27.15	7
33	28.94	7
35	28.51	7
37	28.80	7

Table 6-3. (Continued.)

Impact Energy (eV)	Cross Section ($x10^{-17}cm^2$)	Uncertainty (±%)
39	29.25	7
41	29.02	7
43	28.78	7
45	28.41	7
47	27.66	7
49	26.46	7
51	26.25	7
53	26.58	7
55	26.22	7
57	26.58	7
59	26.09	7
63	25.89	7
67	25.32	7
72	24.48	7
77	24.16	7
82	23.89	7
87	23.04	7
92	22.54	7
97	21.98	7
102	21.54	7
107	20.93	7
112	20.12	7
117	19.59	7
127	18.76	7

Table 6-3. (Continued.)

Impact Energy (eV)	Cross Section ($x10^{-17}cm^2$)	Uncertainty (±%)
137	17.65	7
147	17.34	7
157	16.51	7
167	16.73	7
177	16.21	7
187	15.49	7
197	15.17	7
217	14.41	7
237	13.22	7
257	12.48	7
277	11.84	7
297	11.22	7
317	11.11	7
337	10.52	7
367	9.92	7
397	9.27	7
447	8.47	7
497	7.94	7
547	7.59	7
597	7.22	7
697	6.67	7

However, because of the shortage of the knowledge of the autoionization levels in Sr^+, there is no evidence available which of the two results is more correct. The reason of the systematic discrepancies between the two experimental results can not be made clear at the moment.

Although many other autoionizing states may lie between 21 eV and 30 eV (for example, $4p^5 5s^2$ autoionizing state is at about 24 eV[82]), the identification of the $4p^5 4d5s$ state for the most prominent enhancement at 21 eV must be reasonable because the transition of the 4p --- 4d excitation will have the largest probability since the two electrons have the same principal quantum number and hence the overlap between their orbitals must be the most considerable.

6-4. Ba^+ Single Ionization.

6-4.1 Discussion of Results.

The experimental results of single ionization cross section for Ba^+ are shown in Fig.6-8 together with the results of Peart and Dolder[83], and Feeney et al.[84] Although the results of Peart and Dolder and Feeney et al. are in good agreement in both magnitude and shape, the present results are 15 to 20% smaller than the others.

An abrupt rise is found at an impact energy 16 eV, which has already been assigned to be the contribution of the $5p^5 5d(^3P)$ $6s(^2P)$ autoionizing state. The excitation energy to this state is calculated to be 16.26 eV by Hansen.[81] Some distinct structures are found in the energy region from 18 to 25 eV. Fig.6-9 shows the ionization cross section near the threshold region. The crossed-beam results of Peart et al.[85] are also shown, where they adopted the electron energy selector in place of the normal

electron gun used in the previous measurements[83] in order to enhance the energy resolution to make more detailed observations of the structures in the Ba^+ ionization curve. As shown in the figure, they succeeded in resolving the structures with the refined electron beam of 0.15 eV energy resolution. Although the electron energy selector has not been used in the present study, we also succeed in resolving the structures and the energy positions of these structures are in good agreement with those of Peart et al. These structures are believed to be the contributions of the many autoionizing states with the configuration $5p^5 5d6s$.

The numerical values for Ba^+ single ionization cross sections are listed in Table 6-4.

6-4.2 Comparison with Theory.

Griffin et al.[86] calculated the excitation-autoionization cross section of $5p^6 6s$ --- $5p^5 5d6s$ --- $5p^5$ + e in Ba^+. Their results are shown in Fig.6-10 together with the present experimental results. The theoretical autoionization cross section is added to an estimate of the direct ionization cross section calculated using the Lotz formula. They used the unitarized distorted-wave method to calculate the excitation cross sections to 23 autoionizing states of the configuration $5p^6 5d6s$. They identified 21 dipole-forbidden excited states which are located between 15.6 eV and 19.9 eV, and 2 dipole-allowed excited states $5p^5 5d(^1P)6s\ (^2P)$ at 21.8 eV. The agreement between the theory and the experiment is fairy good in both the magnitude and the shape at the energies below 22 eV and in the higher energy region above 40 eV. However, the distorted-wave calculation far overestimates the dipole-allowed excitation cross section to the $5p^5 5d(^1P)$

Table 6-4. Numerical List of Ba^+ Single Ionization.

Impact Energy (eV)	Cross Section ($x10^{-16}cm^2$)	Uncertainty (±%)
10.0	0.00	----
11.0	0.18	20
12.0	0.34	10
13.0	0.49	9
14.0	0.67	8
15.0	0.81	7
16.0	1.00	7
16.3	1.15	7
16.5	1.50	7
16.7	1.69	7
17.0	1.98	7
17.3	2.35	7
17.6	2.59	7
18.0	3.16	7
18.5	3.70	7
19.0	3.30	7
19.5	2.99	7
20.0	2.96	7
20.5	3.46	7
21.0	3.60	7
21.5	3.50	7
22.0	3.18	7
22.5	3.32	7

Table 6-4. (Continued.)

Impact Energy (eV)	Cross Section ($x10^{-16}cm^2$)	Uncertainty (±%)
23.0	3.68	7
24.0	3.38	7
25.0	3.43	7
26.0	4.03	7
27.0	4.04	7
28.0	4.02	7
30.0	3.74	7
31.0	3.68	7
32.0	3.25	7
33.5	3.37	7
35.0	3.48	7
36.0	3.25	7
37.0	3.39	7
38.0	3.45	7
40.0	3.70	7
42.0	3.60	7
44.0	3.54	7
46.0	3.55	7
48.0	3.67	7
53.0	3.62	7
58.0	3.59	7
63.0	3.50	7
68.0	3.43	7
73.0	3.35	7

Table 6-4. (Continued.)

Impact Energy (eV)	Cross Section ($x10^{-16}cm^2$	Uncertainty (±%)
78.0	3.36	7
88.0	3.25	7
98.0	3.14	7
108.0	3.10	7
118.0	2.92	7
128.0	2.68	7
138.0	2.58	7
148.0	2.25	7
158.0	2.42	7
178.0	2.34	7
198.0	2.13	7
228.0	2.01	7
258.0	1.80	7

$6s(^2P)$ state in the energy region around 22 eV.

CHAPTER 7

RESULTS AND DISCUSSION - DOUBLE IONIZATION

In this chapter, the results for double ionization cross sections are presented. The results for Na^+ and K^+ are already published[73] and this paper is bound to this thesis as Appendix-C.

Several double ionization processes are possible as listed in Table 1-1. Process 6, 7 and 8 in Table 1-1 are the one-electron-target processes, on the other hand, process 5 is the two-electron-target process, which is very difficult to calculate the cross section theoretically.[87] Therefore only a limited number of calculations for the double ionization cross section is reported previously especially for the two-electron-target process. Among the ion species presented in this chapter, it is only for Ba^+ that the theoretical cross section is available. So this chapter does not include the comparisons of experimental results with theory except for Ba^+.

7-1 Results and Discussion of Cross Section for Na^+ Double Ionization.

Cross sections for the Na^+ double ionization are shown in Fig.7-1 as a function of impact energy. The present data are the first systematic measurements with the crossed-beam technique. Sayle and Feeney[88] reported the maximum value of double ionization cross section for Na^+ to be 7×10^{-19} cm^2 at electron energy 400 eV; however the maximum cross section in our results is 9.6×10^{-19} cm^2 at electron energy 450 eV. As the cross section curve has not been published by Sayle and Feeney, there is no means to

make clear the cause of this discrepancy.

Numerical values of the cross sections for the Na^+ double ionization are listed in Table 7-1.

7-2 Results and Discussion of Cross Section for K^+ Double Ionization.

Results for the double ionization of K^+ are shown in Fig.7-2. A small but well reproducible increase in the cross section, which starts at impact energy about 300 eV, is observed. Considering that the ionization energy of the $L_{2,3}$-electrons are about 320 eV[82], we interpret this structure to be attributed to the contribution from the L-shell ionization-autoionization (Auger) process,

Numerical values of the cross sections for the K^+ double ionization are listed in Table 7-2.

7-3. Results and Discussion of Cross Section for Sr^+ Double Ionization.

The results of double ionization cross section for Sr^+ are shown in Fig.7-3 and their numerical values are listed in Table 7-3.

As shown in the figure, some structures and changes in slope are found in the present experimental results, i.e. a small enhancement at an impact energy about 60 eV, a small structure at about 140 eV and a small change in slope at about 160 eV. To find possible mechanisms for these structures, some energy levels which can contribute to the double ionization process in Sr^+ are shown in Fig.7-4. The long dashed line in the figure is the double ionization threshold energy, i.e. the excited states above this line can contribute to the double ionization cross section.

Table 7-1. Numerical List of Na^+ Double Ionization.

Impact Energy (eV)	Cross Section ($x10^{-19}cm^2$)	Uncertainty (±%)
100	0.00	-----
120	0.89	100
140	1.29	50
160	2.40	+24, -23
180	3.47	+20, -19
200	3.98	+16, -15
240	5.62	+14, +13
300	8.51	+13, +12
350	9.12	+13, +12
400	9.12	+13, +12
450	9.55	+13, +12
500	9.12	+13, +12
600	7.94	+13, +12
700	7.94	+13, +12
800	7.41	+13, +12
900	6.17	+13, +12
1000	6.46	+13, +12
1200	5.89	+13, +12
1300	5.13	+13, +12
1500	4.51	+13, +12

Table 7-2. Numerical List of K^+ Double Ionization.

Impact Energy (eV)	Cross Section ($x10^{-18}cm^2$)	Uncertainty ($\pm$%)
80	0.00	----
90	0.60	60
100	1.48	+33, -32
110	1.79	+20, -19
120	2.30	+15, -14
130	2.55	+14, -13
140	2.76	+14, -13
150	2.88	+13, -12
160	2.87	+13, -12
170	2.90	+13, -12
180	2.95	+13, -12
190	2.87	+13, -12
200	2.93	+13, -12
220	2.76	+13, -12
240	2.54	+13, -12
265	2.42	+13, -12
300	2.35	+13, -12
350	2.20	+13, -12
400	2.30	+13, -12
450	2.02	+13, -12
500	1.92	+13, -12
550	1.83	+13, -12
600	1.68	+13, -12

Table 7-2. (Continued.)

Impact Energy (eV)	Cross Section ($x10^{-18}cm^2$)	Uncertainty (%)
700	1.67	+13, -12
800	1.39	+13, -12
900	1.29	+13, -12
1000	1.27	+13, -12
1200	1.15	+13, -12
1400	1.05	+13, -12

Table 7-3. Numerical List of Sr^+ Double Ionization.

Impact Energy (eV)	Cross Section ($x10^{-18}cm^2$)	Uncertainty (±%)
53	0.00	----
54	0.09	100
55	0.33	12
56	0.44	10
57	0.64	8
58	0.98	8
59	1.36	7
60	1.79	7
61	2.06	7
62	2.89	7
63	3.62	7
64	4.20	7
65	4.91	7
67	6.12	7
69	7.82	7
71	9.36	7
73	10.94	7
75	12.25	7
77	13.09	7
79	14.09	7
81	15.09	7
83	15.56	7
85	16.56	7

Table 7-3. (Continued.)

Impact Energy (eV)	Cross Section ($x10^{-18}cm^2$)	Uncertainty (±%)
87	17.34	7
89	17.89	7
91	18.62	7
93	19.06	7
95	19.72	7
97	19.63	7
100	20.59	7
105	21.74	7
110	21.60	7
115	22.06	7
120	21.94	7
125	21.43	7
130	21.03	7
135	21.33	7
140	21.35	7
145	20.91	7
155	19.56	7
165	18.29	7
175	18.24	7
185	17.66	7
195	17.34	7
205	16.82	7
215	16.36	7
225	16.12	7

Table 7-3. (Continued.)

Impact Energy (eV)	Cross Section ($x10^{-18}cm^2$)	Uncertainty (±%)
235	15.60	7
245	15.31	7
255	14.97	7
275	14.14	7
295	13.65	7
315	13.08	7
335	12.40	7
355	12.13	7
375	11.67	7
395	10.91	7
415	10.62	7
435	10.60	7
455	10.30	7
475	9.51	7
495	9.18	7
525	8.96	7
555	8.44	7
595	7.91	7
645	7.35	7
695	6.74	7
745	6.19	7
795	5.91	7
895	5.23	7
995	4.87	7

These energy levels are adopted from the Auger electron spectroscopy[89] (labeled 'AS' in the figure) and the Hartree-Fock calculation of Clementi and Roetti[82] (labeled 'HF' in the figure).

From Fig.7-4, tentative identifications of the structures observed in the experimental results are done. Their energy positions observed at 60 eV, 140 eV and 160 eV correspond to those of $3d^{10}4s4p^65s$ state in Sr^{2+}, $3d^94s^24p^65s^25p$ state in Sr atom, and $3d^94s^24p^65s^2$ in Sr^+ and/or $3d^94s^24p^65s$ states in Sr^{2+}, respectively, all of which can contribute to the double ionization process. The 1st and 4th processes are the inner-shell ionization-autoionization, the 2nd is the resonance capture-multistep autoionization, and the 3rd is the inner-shell excitation-double autoionization and/or -auto double ionization.

For the confirmation of these identifications, further quantitative investigations of the energy levels and the excitation cross sections are necessary.

7-4. Ba^+ Double Ionization.

The double ionization results for Ba^+ are presented in this chapter. Some ionization processes, which can contribute to the double ionization, are identified in the experimental results. The processes include the direct double ionization, i.e.,

$$e + Ba^+(KLM4s^24p^64d^{10}5s^25p^66s) \text{ ---- } Ba^{3+}(4d^{10}5s^25p^5) + 3e \text{ , } \text{----------(7-2)}$$

and the direct single ionization of 4d and 5s electrons followed by autoionization, i.e.,

$$e + Ba^+(KLM4s^24p^64d^{10}5s^25p^66s) \text{ ---- } Ba^{2+*}(4d^95s^25p^66s) + 2e$$
$$\text{└---- } Ba^{3+}(4d^{10}5s^25p^5) + e \text{ , } \text{---------(7-3)}$$

and

$$e + Ba^{+}(KLM4s^2 4p^6 4d^{10} 5s^2 5p^6 6s)$$
$$\text{---- } Ba^{2+*}(4d^{10} 5s^1 5p^6 6s) + 2e$$
$$\text{└---- } Ba^{3+}(4d^{10} 5s^2 5p^5) + e \text{ , ---------(7-4)}$$

where the superscript * indicates the excited state.

Addition to the above processes, the experimental results suggest the contribution of the 4d-excitation-double autoionization and/or 4d-excitation-auto-double ionization, such as

$$e + Ba^{+}(KLM4s^2 4p^6 4d^{10} 5s^2 5p^6 6s)$$
$$\text{---- } Ba^{+*}(4d^9 5s^2 5p^6 6s^2) + e$$
$$\text{└---- } Ba^{2+*}(4d^{10} 5s^1 5p^6 6s) + e$$
$$\text{└---- } Ba^{3+}(4d^{10} 5s^2 5p^5) + e \text{ --(7-5)}$$

and,

$$\text{└---- } Ba^{3+}(4d^{10} 5s^2 5p^5) + 2e \text{ . --------(7-6)}$$

Taking into account the theoretical calculation for the processes (7-3) and (7-4) using the distorted wave Born-exchange approximation by Younger, it is recognized that the contributions from two step double ionization processes such as the processes (7-3) and (7-4) are dominant in the case of Ba^+ double ionization.

Following sections deal with the bases of the above discussion and the comparison with the theory.

7-4.1. Discussion of the Cross Section.

Results of double ionization cross section for Ba^+ are shown in Fig.7-5. Fig.7-6 shows the results in an expanded scale near the threshold. The results show some characteristic features; the cross section begins to increase from its threshold (45.5 eV), additional increases can be found at impact energies about 50 eV and 90 eV, the cross section has a sharp maximum at about 120 eV, and there is a small shoulder at around 200 eV. These features

suggests the contributions from the indirect double ionization processes such as the excitation-autoionization process. To find possible indirect ionization mechanisms, some energy levels which can contribute to the double ionization process in Ba^+ are shown in Fig.7-7. The dashed line in the figure is the double ionization threshold energy, i.e. the excited states above this line can contribute to the double ionization cross section. These energy levels are adopted from the Hartree-Fock calculation in references 90) and 91).

The double ionization cross section curves for $I^+(5p^4)$[92], $Xe^+(5p^5)$[92], $Cs^+(5p^6)$[93], and $Ba^+(5p^66s)$ are compiled in Fig.7-8. It can be found that these cross section curves have very similar shapes except that only the curve for Ba^+ has the additional increase near the threshold.

For I^+ and Xe^+, Achenbach et al.[92] reported that the sharp maxima could be the contributions from the 4d direct ionization-autoionization (process of the type shown in equation (7-3)) and they estimated the 4d-partial ionization cross section from the estimation of the direct double ionization cross sections using a fitting procedure. Figure 7-9 shows their attempt to estimate the 4d ionization cross section. Solid lines in the figure represent their estimation for the contributions from the direct double ionization which are obtained by a fitting procedure with the fitting function

$$\sigma(E) = A\frac{\ln(E/P_i)}{E\ P_i}\left(1 - B\exp\left(-C\left(\frac{E}{P_i} - 1\right)\right)\right) , \quad \text{------} \quad (7\text{-}1)$$

where E is the impact energy, P_i is the double ionization threshold energy and A, B and C are the fitting parameters. They obtained the partial cross section for 4d-ionization by subtrac-

ting the direct part (represented by the solid lines in Fig.7-9) from the measured total cross sections. The resulting 4d ionization cross section curve has only one sharp peak and the cross section is close to zero at impact energy about 230 eV.

An experimental approach to determine directly the 4d-ionization cross section has been done by Takayanagi et al.[94),95)] They measured the partial ionization cross section of 4d-electrons in Xe atom by measuring the emitted electrons from the 4d-hole states via autoionization processes, in other technical term, the $N_{4,5}OO$ Auger electron emissions in Xe. Their results are shown in Fig.7-10. The cross sections increase rapidly from the threshold and form a fairly sharp maximum followed by a broad maximum at about 500 eV. The cross section curve reveals a characteristic of the double maxima. Characteristic features in the cross section curves of I^+, Xe^+, Cs^+ and Ba^+ (Fig.7-8), i.e. a rapid rise from the threshold, a sharp maximum, and a distinct shoulder at higher energy, are considered to be a reflection of the features of double maxima in the 4d-ionization curves of respective species. These experimental observations strongly suggests that not only the sharp peak at 125 eV, but the small shoulder around 200 eV are also the contributions from the 4d-ionization-autoionization in the cross section curve in Ba^+.

Although the sharp peak in the cross section curve begins at impact energy about 90 eV, the 4d ionization energy is reported to be 109 eV from the Hartree-Fock calculation[90)]. This difference can be understood by the contribution from the excitation-double autoionization and/or the excitation-auto-double ionization (processes of the type shown in equations (7-5) and (7-6)). Calculated energy levels of core excited $Ba^+(4d^9 5s^2 5p^6 6s^2\ ^2D_{5/2,3/2})$ states are about 93 eV and 96 eV above Ba^+ ground

state[91]. These excited states are high enough to decay with the emission of additional two electrons, which results in the double ionization. Other excitation processes may be possible to contribute the double ionization below the 4d-ionization threshold, however, data of the energy levels of such excited states are not available up to now.

In addition to the 4d-direct ionization, direct ionization of 5s electron can contribute to the double ionization (processes of the type shown in equation (7-4)), whose binding energy calculated using Hartree-Fock method is 45 eV[90], whereas the double ionization threshold is about 45 eV. As the binding energy of 5s electron is very close to the double ionization threshold energy, it may be difficult to distinguish the respective contributions of the 5s-ionization-autoionization and direct double ionization. Anyway, the small increase in the slope found in the present results at about 50 eV should be interpreted as an appearance of the 5s-ionization contribution.

Table 7-4 lists the numerical values of the experimental results for Ba^+ double ionization.

7-4.2 Comparison with Theory.

Reliable quantum method to calculate the direct double ionization cross section has not been developed up to now. In this section, the experimental results for Ba^+ double ionization are compared with the theoretical calculation of the direct single ionization cross sections for 4d and 5s electrons by Younger using the distorted wave Born-exchange approximation (DWBEA)[90].

The method of Younger's calculation is described in detail in the previous papers[96-98]. So a brief outline of his method will be presented here.

Table 7-4. Numerical List of Ba^+ Double Ionization.

Impact Energy (eV)	Cross Section ($x10^{-17}cm^2$)	Uncertainty (±%)
44.5	0.00	----
45.5	0.01	100
46.5	0.07	12
47.5	0.14	8
48.5	0.23	8
49.5	0.32	7
50.5	0.38	7
51.5	0.47	7
52.5	0.57	7
53.5	0.68	7
54.5	0.82	7
55.5	0.89	7
56.5	1.04	7
57.5	1.11	7
59.5	1.30	7
61.5	1.42	7
63.5	1.53	7
65.5	1.64	7
67.5	1.72	7
69.5	1.80	7
71.5	1.91	7
73.5	1.97	7
75.5	2.02	7

Table 7-4. (Continued.)

Impact Energy (eV)	Cross Section ($x10^{-17}cm^2$)	Uncertainty (±%)
77.5	2.10	7
79.5	2.16	7
81.5	2.22	7
83.5	2.31	7
85.5	2.44	7
87.5	2.67	7
89.5	2.87	7
91.5	3.21	7
93.5	3.61	7
96.5	4.05	7
99.5	4.34	7
103.5	4.87	7
108.5	5.22	7
113.5	5.46	7
118.5	5.45	7
123.5	5.36	7
128.5	5.03	7
133.5	4.86	7
138.5	4.67	7
143.5	4.45	7
153.5	4.23	7
163.5	4.05	7
173.5	3.96	7
183.5	3.94	7

Table 7-4. (Continued.)

Impact Energy (eV)	Cross Section ($x10^{-17}cm^2$)	Uncertainty (±%)
193.5	3.78	7
203.5	3.81	7
213.5	3.62	7
223.5	3.51	7
233.5	3.47	7
243.5	3.45	7
258.5	3.31	7
273.5	3.17	7
293.5	3.03	7
318.5	2.86	7
343.5	2.67	7
373.5	2.49	7
393.5	2.48	7
423.5	2.30	7
453.5	2.26	7
493.5	2.08	7
543.5	1.97	7
593.5	1.85	7
643.5	1.80	7
693.5	1.71	7

The target ion is described by a Hartree-Fock wave function. Incident and scattered partial waves are computed in the potential of the initial target state, whereas the ejected partial waves are computed in the term-dependent Hartree-Fock potential of residual ion. For the 4d ionization, only the dominant dipole excitation of $4d^{10}$ --- $4d^{9}kf$ channel is computed and the ground state configuration interaction of the type $4d^{10} + 4d^{8}4f^{2}$ is included. Electron exchange among the two free electrons in the final state is accounted for by using the maximum-interference exchange approximation of Peterkop.[99]

Younger's DWBEA results are shown in Fig.7-11 together with the present experimental results. The long dashed curve and the short dashed curve in the figure represent the calculated ionization cross sections for 5s and 4d electrons, respectively, and the solid line represents the sum of the 5s and 4d ionization cross section, i.e. calculated contribution to the double ionization from the inner-shell ionization-autoionization processes.

Both the calculated 5s and 4d ionization curves rise rapidly near the respective ionization thresholds. A very sharp resonance is found for the 4d ionization, whereas the experiment indicates a much broader resonance feature. This resonance, named 'giant resonance', is a shape resonance which arises from a double well nature of the potential of the scattering partial wave.

For I^{+}, Xe^{+} and Cs^{+}, Younger's DWBEA results agree well with the experimental results in both magnitude and shape.[98] The agreement between the present experimental results and the DWBEA calculation is poorer than those for I^{+}, Xe^{+} and Cs^{+}. This disagreement may be due to the added complication introduced by the presence of a weakly bound 6s electron in Ba^{+}.[90] For the other cases, the valence electrons are tightly bound and the polariza-

tion of the target by the incident electron is expected to be weaker than that in Ba^+.

Although the agreement between the experiment and the theory seems to be poor for Ba^+ compared to the other ion species up to now, we believe that the Younger's DWBEA calculation has succeeded in reproducing and interpreting the experimental results qualitatively.

CHAPTER 8

CONCLUSION

8-1. Summary of Results.

Absolute cross sections of single and double ionization by electron impact for singly charged alkali and alkaline earth ions have been measured using the crossed-beam apparatus, which has been designed and constructed by the author himself in cooperation with several other members for the electron-ion collision team of the atomic physics group of Sophia University. The cross sections have been obtained by monitoring the product doubly or triply charged ions with the use of the single particle detection technique. Many possible systematic effects have been carefully studied, and the cross sections have been demonstrated to have the correct functional dependence on the experimentally measurable quantities.

The results of the single ionization cross section for Na^+ are well reproduced by the Lotz formula which estimates the contributions from the direct ejections of the 2s and 2p electrons, while the experimental results of single ionization for K^+ suggests the contribution from the excitation-autoionization processes. The autoionizing levels are adopted from the identifications by Aizawa et al.[78], where they studied the autoionizing levels in K^+ by measuring the ejected electrons in low energy K^+ - He collisions.

Single ionization cross sections for Sr^+ and Ba^+ shows large contributions from the 4p --- 4d and the 5p --- 5d excitation-autoionization, respectively. The contributions of these autoionization processes are estimated to exceed about 2 and 3 times of

those of direct single ionization processes in Sr^+ and Ba^+, respectively. The present results for Sr^+ shows systematic discrepancies with the previous crossed-beam results by Peart and Dolder[80], whose reason can not be made clear at the moment.

Double ionization cross section results presented in this thesis are the first systematic measurements up to now. Double ionization results for Na^+ have shown that only the direct double ionization process is dominant. For the K^+ double ionization, the contribution from the L-shell direct ionization followed by autoionization have been found. Results of double ionization cross sections for Na^+ and K^+, together with the results of other alkali metal ions, Li^+,[100] Rb^+,[101] and Cs^+,[93] are shown collectively in Fig.8-1. From this figure one can find a systematics in which the cross section increases with atomic number Z of the ion. In order to display a general trend of the systematic variation of the double ionization process with atomic number Z, the ratios of the double ionization cross section to the single ionization cross section are plotted as functions of impact energy in Fig.8-2, for the same species of alkali metal ions as in Fig.8-1. These ratios are generally known to become constant at higher impact energies when the direct ionization process is dominant.[30),102] The ratios for Li^+ and Na^+ ions tend to become constant with increasing the electron energy. On the other hand, those of K^+, Rb^+ and Cs^+ tend to increase further with the impact energy, which suggest the influence of indirect processes as the excitation-autoionization and/or the inner-shell ionization-autoionization.

The experimental results of the double ionization for Sr^+ suggest the contribution of inner-shell ionization-autoionization ($M_{4,5}$-NN Auger) and/or inner-shell excitation-double autoioniza-

tion ($M_{4,5}^{*}$-NN Auger). This idea can not be confirmed because of the shortage of the knowledge of the energy levels and the theoretical calculation for the cross sections in Sr^{+}.

The curve of the double ionization cross sections for Ba^{+} has an a very distinguished shape in which cross section increases at impact energies about 50 eV and 90 eV, a sharp maximum at about 120 eV, and a distinct shoulder at around 200 eV. These characteristic features are analyzed and identified as contributions of the 5s and 4d ionizations followed by autoionization with the aid of the theoretical calculation using the distorted-wave Born-exchange approximation (DWBEA) by Younger.[90] A very sharp resonance found in the experimental results have been explained as the contribution from the 4d direct ionization by the theory. This resonance is the shape resonance and named 'giant resonance'. This identification is supported by the direct measurements of 4d-ionization cross sections in Xe atom by Takayanagi et al.[94),95)]

The 'giant resonance' feature has not been observed in the Sr^{+} double ionization results. The disappearance of the giant resonance in Sr^{+} is consistent with the experimental results of 3d-ionization cross sections in Kr atom, whose configuration is $KL3s^{2}3p^{6}3d^{10}4s^{2}4p^{6}$, measured by Takayanagi et al.[94),95)] (Fig.8-3), which have proved nonexistence of such resonance-like features.

8-2 Suggestions for Further Study

As the measurements for alkali ions were done in the early state of the present work, the experimental results contains relatively large errors. Therefore it is to be desired that these measurements will be refined in order to investigate the indirect

ionization processes found in the results of the single and double ionization for K^+ in more detail.

For the single ionization of the alkaline earth ions except for Be^+ and Mg^+, the contributions from the np --- nd excitation-autoionization process have been found to be dominant by the previous workers[80] and our group. These cross sections are compiled in Fig.8-4. The abrupt rise found in the results of Ca^+, Sr^+ and Ba^+ are attributed to the np --- nd excitation-autoionization. The Ba^+ results shows some distinct structures in the energy region from 18 eV to 25 eV, however, such structures are not found in the results of Ca^+ and Sr^+. As shown in chapter 6-4.2, Griffin et al.[86] succeeded in reproducing the structures due to the np --- nd transition followed by the autoionization in Ba^+. They also calculated the single ionization cross sections for Ca^+ [86] and their results shows some structures similar to those found in Ba^+, although such structures are not observed in the experimental results of Peart and Dolder[80]. It is worth measuring carefully the single ionization cross section for Ca^+ especially at low impact energy in order to find whether the theoretical prediction is correct or not.

In the results of Ba^+ double ionization, the experimental ionization function curve can not be interpreted completely by the sum of the 5s and 4d ionization curve calculated by Younger using the DWBEA method, as shown in Fig.7-11. The experimental curve shows a huge broad peak followed by a distinct shoulder, in spite of a sharp single peak in the calculated curve. In our opinion, the partial cross section curve for the 4d-ionization in Ba^+ does behave very similarly with that in Xe atom, for which the partial 4d-ionization curve has been experimentally investigated.[94),95] The 4d-ionization curve in Xe atom reveals the

double maximum character, where the first peak has a width of more than 50 eV (see Fig.7-10) as described in chapter 7-4.1. Not only for the difference in the shape of the curve, there are some discrepancies in the position of the resonance structure between the experiment and theory. For instance, the abrupt rise in the cross section is observed at around 90 eV in the experimental curve, whereas the calculated threshold of the 4d-ionization is 109 eV. This discrepancy suggests the importance of the contribution from other processes, such as the 4d-excitation-double autoionization. Further investigations in both the theoretical and experimental sides are desired to clarify the behavior of the partial cross sections for ionization and excitation of the 4d and other inner-shell electrons in Ba^+.

As the 4d-ionization threshold energy in Ba^+ is 109 eV, while the triple ionization threshold is 102 eV.[103], the 4d-ionization event can contribute to the triple ionization. Because the contribution from the direct triple ionization may be very small compared to that from the 4d-ionization-double autoionization in Ba^+, it will be very useful to measure the triple ionization cross section for the further investigation on the 4d-ionization function.

APPENDIX-A

CHARACTERISTICS OF SURFACE IONIZATION TYPE ION SOURCE

In this appendix, some characteristics of the ion source used in the present study and a discussion for the possible metastable fraction in the product ion are given.

A-1 Ionization Efficiency.

The process of surface ionization can be characterized by the degree of ionization, expressed as

$$\alpha = \frac{n_i}{n_a} , \quad \text{---------- (A-1)}$$

or the surface ionization efficiency given by

$$\beta = \frac{n_i}{n_0} , \quad \text{---------- (A-2)}$$

where n_i and n_a are the numbers of ions and atoms leaving the surface, respectively, and n_0 is the number of particles incident on the surface, i.e.,

$$n_0 = n_i + n_a . \quad \text{---------- (A-3)}$$

The degree of ionization is related to the ionization efficiency as

$$\alpha = \frac{\beta}{1 - \beta} , \quad \text{---------- (A-4)}$$

and

$$\beta = \frac{\alpha}{1 + \alpha} \quad \text{(A-5)}$$

When thermal equilibrium between adsorbed atoms and the ionizing metal is assumed, the degree of ionization is given by the Saha-Langmuir formula as follows,

$$\alpha = \frac{g_i}{g_a} \exp\left(\frac{e(W - I)}{kT}\right) , \quad \text{(A-6)}$$

where W is the work function of the ionizing metal, I the ionization potential of the adsorbed atom, T is the surface temperature, k is the Boltzmann constant, and g_i and g_a are the statistical weights of the ionic and the atomic state, respectively. The ratio g_i/g_a is equal to 1/2 for alkali elements and 2 for alkaline earth elements in the ground states. Table A-1 lists the ionization potentials of alkali and alkaline earth elements and the work functions of commonly used ionizing metals. The ionization efficiencies for Sr and Ba on Re as functions of ionization temperature is shown in Fig.A-1.

A-2. Estimation of Metastable Fraction.

The first excited state of Ba^+ is $Ba^+(5s^25p^65d\ ^2D_{3/2,5/2})$, which lie at above 0.60 eV and 0.70 eV from the ground state of Ba^+, i.e. $Ba^+(5s^25p^66s\ ^2S_{1/2})$. These excited states are the metastable states, so there is a possibility that the primary ion beam may include some fraction of excited states. This metastable fraction can be estimated by using the Saha-equation as follows,

Table A-1. Ionization potentials I of alkali and alkaline earth elements and work functions W of ionizing metals.[65]

Element	I (eV)	Ionizing metal	W (eV)
Cs	3.87	Ta	4.10
Rb	4.16	Mo	4.24
K	4.32	W	4.52
Ba	5.21	Re	4.96
Na	5.14	Ir	5.27
Li	5.36	Pt	5.32
Sr	5.70		
Ca	6.11		

$$\frac{N^+(^2D_{3/2})}{N^+(^2S_{1/2})} = \frac{4}{2}\exp\left(-\frac{0.60\text{eV}}{kT}\right) = \begin{matrix} 0.06 \text{ (at T = 2000°)} \\ 0.08 \text{ (at T = 2200°)} \end{matrix} \quad \text{(A-7)}$$

for J=3/2 state, and

$$\frac{N^+(^2D_{5/2})}{N^+(^2S_{1/2})} = \frac{6}{2}\exp\left(-\frac{0.70\text{eV}}{kT}\right) = \begin{matrix} 0.05 \text{ (at T = 2000°)} \\ 0.08 \text{ (at T = 2200°)} \end{matrix} \quad \text{(A-8)}$$

for J=5/2 state, where $N^+(^2D_{3/2})$, $N^+(^2D_{5/2})$ and $N^+(^2S_{1/2})$ are the fraction of the excited states of J=3/2 and J=5/2, and the ground state, respectively. As a result, about 10 % of the primary ion beam can be in metastable states at the ionizer temperature about 2000 K. However, in the present results, the contribution from the ion beam in metastable states to the cross section seems to be negligibly small. This may be due to a large energy spread of the electron beam (about 1 eV) while the excitation energy of these metastable states are 0.6 to 0.7 eV.

In the case of Sr^+, the first excited state are $Sr^+(4s^24p^64d\ ^2D_{3/2,5/2})$, which lie above 1.80 and 1.84 eV from the ground state Sr^+ $(4s^24p^65s\ ^2S_{1/2})$, respectively. By the calculation using the Saha-equation, the metastable fraction in the Sr^+ ion beam is estimated to be less than 0.01 % at ionizer temperature of around 2000 K. Therefore it is concluded that the contribution from the metastable Sr^+ ion can be negligible.

APPENDIX - B

DIAGRAM OF ELECTRIC CIRCUIT

As described in the previous chapters, some electric circuits for the data acquisition and the measurements of the experimental parameters have been made by the author. The diagrams of these electric circuits are given as appendix-B.

The data acquisition system (see chapter 4-9 and Fig.4-17.) is divided into 5 units and their circuit diagrams are given in Fig.B-1 for the control pulse generator unit, in Fig.B-2 for the multiplexer unit and the counter unit, in Fig.B-3 for the chopping pulse driver unit, and in Fig.B-4 for the timer unit.

A circuit diagram for the current integrator (see chapter 5-1 and Fig.5-1) is given in Fig.B-5.

APPENDIX-C

"Measurements of Cross Sections for Single and Double Ionization of Na^+ and K^+ by Electron Impact"

Journal of the Physical Society of Japan,
Vol.55, No.5, May, 1986, pp.1411-1414.

Journal of the Physical Society of Japan
Vol. 55, No. 5, May, 1986, pp. 1411-1414

Measurements of Cross Sections for Single and Double Ionization of Na^+ and K^+ by Electron Impact

Takato HIRAYAMA, Kazutaka ODA, Youji MORIKAWA, Tetsuo ONO, Yoshikazu IKEZAKI, Toshinobu TAKAYANAGI, Kazuyoshi WAKIYA and Hirosi SUZUKI

Department of Physics, Sophia University, Kioicho 7-1, Chiyoda-ku, Tokyo 102

(Received December 13, 1985)

Cross sections for single and double ionization of K^+ and Na^+ by electron impact have been measured as a function of electron energy from their respective threshold to approximately 1500 eV with the use of the electron-ion crossed-beam technique. The results for single ionization of Na^+ and K^+ are in good agreement with the previous crossed-beam data within the experimental uncertainties. Contributions from an autoionization and an L-shell direct ionization followed by autoionization (Auger effect) have been found in the results of single and double ionization cross sections for K^+.

Measurements of absolute ionization cross sections by electron impact for various ions have been extensively done in recent years. However in the case of double ionization, there are limited numbers of reports available up to now. We have measured cross sections of single and double ionization for Na^+ and K^+ ions using the crossed-beam technique.

As the detail of the apparatus and the experimental procedure will be described in a forthcoming paper, only their brief outlines are presented here. Schematic view of the apparatus is shown in Fig. 1. It consists of an ion source equipped with a mass-selector, an ion-

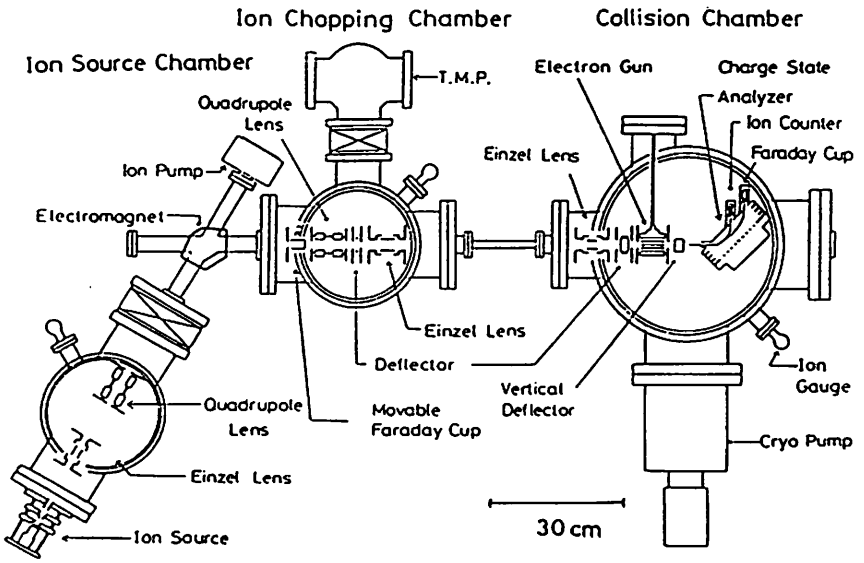

Fig. 1. Schematic diagram of the crossed-beam apparatus.

chopping chamber, and a collision chamber which includes an electron collision device and a charge state analyzer with detectors. The three parts are connected with various types of ion lenses and slit systems. These chambers are evacuated separately, providing ultimate pressures of about 3×10^{-8} Pa, 2×10^{-7} Pa and 2×10^{-6} Pa, in the collision chamber, the chopping chamber and the ion source chamber, respectively.

An ion beam is generated in a thermionic emission type ion source[1] and is accelerated to 2 keV. The ions are mass-selected by an electro-magnet and focused to 1 mm diameter and collide with an electron beam at a right angle. After the collision region, primary and product ions are separated by a parallel-plate electrostatic analyzer according to their charge state and detected by a Faraday cup and a product ion counter, respectively. The ion counter consists of a channel electron multiplier (Ceratron EMT6081B, MURATA) and an entrance aperture, whose diameter is the same as that of the entrance cone of the multiplier. The product ions are accelerated with a voltage of about 3.5 kV before entering the entrance cone. The potential of the entrance aperture is adjusted so that the counting efficiency of the ion counter gives the maximum value. The ion current at the collision volume was 1 to 10 nA at 2 keV of energy, while the electron current was about 0.1 mA for 100 eV. The double beam chopping technique[2] is used for the separation of true signals from background signals. Typical S/N ratio was 1 to 10 and the acquisition time was 300 to 600 sec in the single ionization measurements and 600 to 1200 sec in the double ionization measurements.

To obtain the cross section, a form factor, which represents the overlap integral of the beam current profiles, must be determined.[2] An L-shape scanner with a narrow slit moving vertically through the two beams is used to measure the form factor.

Direct measurements of the detection efficiencies of the ion counter for the product ions, which is necessary to deduce the absolute cross sections from the counting rate, have not been performed because doubly or triply ionized ions were not available with our present ion source. However the detection efficiencies for the product Na^{2+} and K^{2+} ions of the incident energies, 9 keV, were supposed to be approximately unity, because our data for single ionization cross sections for both Na^+ and K^+ ions give the best agreement in absolute value with those by Peart and Dolder,[3] when we assume the efficiencies to be unity. As for the Na^{3+} and K^{3+}, which are produced in the double ionization process, the detection efficiencies must be closer to unity, as the efficiencies are generally larger for the ions with higher charge and larger kinetic energy.[4]

Uncertainties in the absolute values of cross sections are deduced from the quadrature sum of the estimated error in the counting efficiency and those in the directly measured quantities, i.e. ion current, electron current, counting rate of product ions, the form factor, and others. Dominant parts of the errors are involved in the form factor and the counting efficiency, which are estimated to be $\pm7\%$ and $+0$ to -5%, respectively. Uncertainties in counting statistics are about 1% near the maximum cross sections. The overall uncertainty is estimated to be -10% to $+14\%$.

The results for single ionization of Na^- are shown in Fig. 2. Our results are in good agreement with the previous crossed beam data of Peart and Dolder[3] and Hooper *et al.*[5] within the experimental uncertainties. A curve by the calculation using the semiempirical formula of Lotz[6] is also shown in Fig. 2.

The results for single ionization of K^- are shown in Fig. 3, together with the results of Peart and Dolder[3] and Hooper *et al.*[5] Although, our results and those of Peart and Dolder are in good agreement, results of Hooper *et al.* are about 13% smaller than ours in the energy region where the cross sections show their maximum. A curve by the Lotz calculation, which includes contributions by both the 3p and 3s ionizations, is also shown in Fig. 3.

In our results an abrupt rise is observed near the threshold, which is attributable to the excitation-autoionization of K^+. Aizawa *et al.*[7] studied the autoionizing states of K^- in the ejected electron spectra resulting from low energy K^++He collisions. They identified five core excited autoionizing states, which are

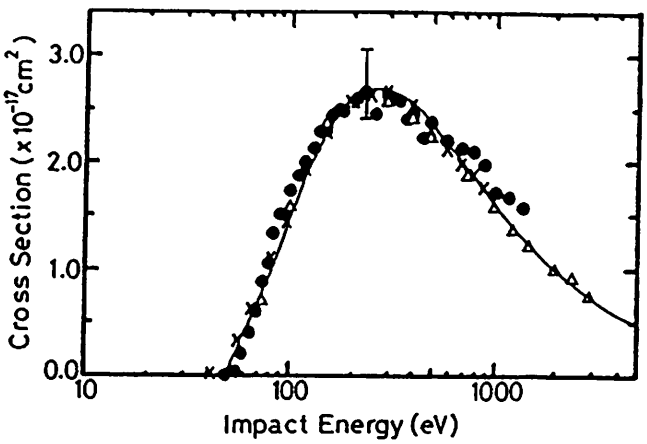

Fig. 2. Single ionization cross sections for Na^+. Closed circles—present results, open triangles—Peart and Dolder,[3] crosses—Hooper *et al.*,[5] solid line—Lotz calculation.[6]

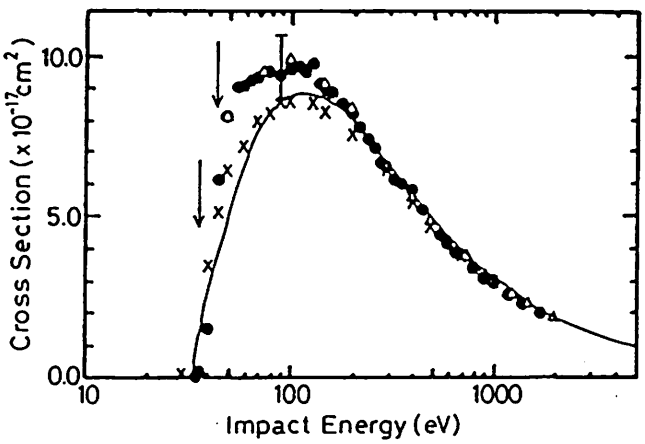

Fig. 3. Single ionization cross sections for K^-. Symbols are the same as in Fig. 2. Arrows show the thresholds of core excited and doubly excited autoionization state. (See text)

situated raging from 5.28 eV (K^- $3s3p^64s$ ^1S) to 10.81 eV (K^- $3s3p^64d$ ^1D) above the ground K^{2+} ($J=3/2$) state. Besides these, they identified three doubly excited autoionizing states, which are from 11.29 eV (K^- $3p^4(^1D)4s^2(^1D)$) to 12.88 eV (K^- $3p^4(^1D)3d4s$) above the ground K^{2+} state. The positions of the lowest core excited and doubly excited states are indicated by arrows in Fig. 3.

Results for double ionization of Na^- and K^- are shown in Fig. 4 together with the results of other alkali metal ions, Li^-,[8] Rb^+,[9] and Cs^-.[10] From this figure one can find a systematics in which the cross section increases with atomic number Z of the ion.

For Na^- and K^+, the present data are the first systematic measurements with the crossed-beam technique. Sayle and Feeney[11] reported the maximum value of double ionization cross section of Na^+ to be 7×10^{-19} cm^2 at electron energy 400 eV; however the maximum cross section in our results is 9.6×10^{-19} cm^2 at electron energy about 450 eV. As the cross section curve of the results of Sayle and Feeney has not been published, the cause of this discrepancy cannot be made clear.

In the curve of K^+, a small but well reproducible increase in the cross section is observed at about 400 eV of impact energy. Considering that the ionization energies of L-

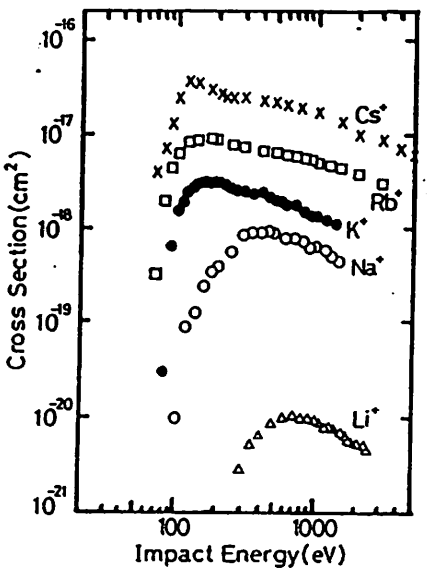

Fig. 4. Double ionization cross sections for Na^+ and K^+ together with the results for Li^+,[6] Rb^+ [9] and Cs^+.[10] The size of the error bar is almost the same as the diameter of the data circle.

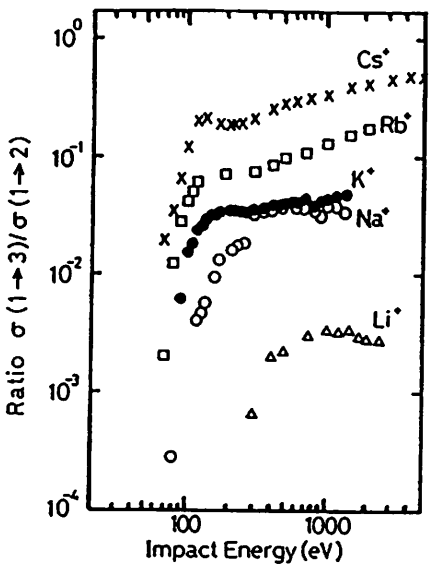

Fig. 5. Ratios of the double ionization cross sections to the single ionization cross sections for alkali metal ions.

shell electrons in K^+ to be 300 to 380 eV, this increase is attributed to the L-shell ionization followed by the Auger-effect, which cause the removal of two electrons from the parent ions. In order to display a general trend of the systematic variation of the double ionization cross sections with atomic number Z, the ratios of the double ionization cross section to the single ionization cross section are plotted as functions of impact energy in Fig. 5, for the same species of alkali metal ions as in Fig. 4. These ratios are generally known to become constant at higher electron energies when the direct ionization process is dominant.[12,13] The ratios for Li^+, Na^+ and K^+ ions tend to become constant with increasing the electron energy, except for that of K^+ which gives a slight increase at higher energies than 300 eV as shown in Fig. 5. On the other hand, those of Rb^+ and Cs^+ tend to increase further with the electron energy in the same energy regions, which suggest the influence of indirect processes as the excitation-autoionization or Auger-effect.

The authors wish to thank the members of ACE-IT group of the Institute of Plasma Physics, Nagoya University, for their stimulating and helpful discussions.

This work was financially supported by the Grant-in-Aid for Special Project Research and that for Fusion Research from the Ministry of Education, Science and Culture.

References

1) R. E. Weber and L. F. Cordes: Rev. Sci. Instrum. 37 (1966) 112.
2) K. T. Dolder: *Case Studies in Atomic Collision Physics*, ed. E. W. McDaniel and M. R. C. McDowell (North Holland, Amsterdam, 1969) p. 249.
3) B. Peart and K. T. Dolder: J. Phys. B1 (1968) 240.
4) D. H. Crandall, J. A. Ray and Carmen Cisneros: Rev. Sci. Instrum. 46 (1975) 562.
5) J. W. Hooper, W. C. Lineberger and F. M. Bacon: Phys. Rev. 141 (1966) 165.
6) W. Lotz: Z. Phys. 216 (1968) 241.
7) H. Aizawa, F. Koike, F. Sasaki, K. Wakiya and H. Suzuki: J. Phys. B18 (1985) 289.
8) B. Peart and K. T. Dolder: J. Phys. B2 (1969) 1169.
9) D. W. Hughes and R. K. Feeney: Phys. Rev. A23 (1981) 2241.
10) D. R. Hertling, R. K. Feeney, D. W. Hughes and W. E. Sayle II: J. Appl. Phys. 53 (1982) 5427.
11) W. E. Sayle II and R. K. Feeney: *Proc. 13th Int. Conf. Physics of Electronic and Atomic Collisions, Paris, 1977* (ICPEAC, Paris 1977) p. 1084.
12) B. L. Schram: Physica 32 (1966) 197.
13) A. Müller, C. Achenbach, E. Salzborn and R. Becker: J. Phys. B17 (1984) 1427.

ACKNOWLEDGEMENTS

I would like to express best gratitude to professor Hirosi Suzuki, Dr. Kazuyoshi Wakiya and Dr. Toshinobu Takayanagi for their encouragements, continuous discussions, and helpful suggestions throughout this work. I also thank professor Tadasu Susuki for his constant encouragements and support.

I am also grateful to the member of the ACE-IT group in the Institute of Plasma Physics, Nagoya University for their helpful advices. Especially, I am indebted to Dr. Shunsuke Ohtani of Institute of Plasma Physics and Dr. Atushi Matsumoto of Hiroshima Institute of Technology for their helpful discussions and useful suggestions.

Dr. Stephen M. Younger of Lawrence Livermore National Laboratory kindly provided the theoretical results on the Ba^+ double ionization prior to the publication and gave me valuable comments. I wish to thank Dr. Kunizo Onda of the Institute of Space and Astronautical Science for his valuable advices and comments on the theoretical aspects.

I also thank the KYOWA VACUUM Company for the construction of the fine apparatus used in the present work.

I am grateful to all the students of the atomic physics group of the Sophia University for their friendship, kind help, and encouragements, especially to Mr. Kazutaka Oda, Mr. Tetsuo Ono, Mr. Youji Morikawa, Mr. Yoshikazu Ikezaki, Mr. Shinji Kobayashi, Mr. Yasushi Kanno, Mr. Akihisa Arakawa, and Miss Makiko Miyagawa, who have been co-workers in my 6-year study carreer of the electron-ion collision experiment in Sophia University.

I wish to thank the Japan Securities Scholarship Foundation

for the financial support during my doctor course period.

Finally I must express my deepest gratitude to my parents for their continuous support.

REFERENCES

1) P.Lenard, Wied. Ann. 51 (1894) 225.

2) K.T.Dolder, M.F.A.Harrison and P.C.Thonemann, Proc.Roy.Soc. A264 (1961) 367.

3) C.Bottcher, D.C.Griffin, M.S.Pindzola and R.A.Phaneuf, "Indirect Processes in Electron-Ion Scattering", ORNL/TM-8868 (1983).

4) M.F.A.Harrison, in "Methods of Experimental Physics" Vol.7B, ed. W.L.Fite and B.Bederson, (New York, Academic Press, 1968) pp.699.

5) E.Salzborn, in "Physics of Ion-Ion and Electron-Ion Collisions", (Plenum, New York, 1983) pp239.

6) H.J.Kunze, Space Sci.Rev. 13 (1972) 565.

7) A.H.Gabriel and D.Jordan, in "Case Studies in Atomic Collision Physics", (North-Holland, Amsterdam, 1972) Vol.2. pp.221.

8) for example, G.H.Dunn, IEEE Trans.Nucl.Sci., NS-23 (1976) 929.

9) F.A.Baker and J.B.Hasted, Phil.Trans.R.Soc. A261 (1966) 33.

10) P.A.Redhead and C.P.Gopalaraman, Can.J.Phys. 49 (1971) 585.

11) E.D.Donets and V.P.Ovsyannikov, Reprint P7-10780, Joint Institute for Nuclear Research, Dubna/USSR, 1977.

12) M.F.A.Harrison, Brit.J.App.Phys., 17 (1966) 371.

13) M.F.A.Harrison, in "Methods of Experimental Physics", vol.7A, ed. B.Bederson and W.L.Fite, (Academic Press, 1968) pp.95.

14) K.T.Dolder, in "Case Studies in Atomic Collision Physics", Vol.1, ed. E.W.McDaniel and M.R.C.McDowell, (North-Holland, 1969) pp.249.

15) G.H.Dunn, in "Atomic Physics", ed. V.W.Hughes, V.W.Cohen, and

F.M.J.Pichanick, (Plenum Press, 1969) pp.417.

16) K.T.Dolder and B.Peart, Rep.Prog.Phys. 39 (1976) 693.

17) M.F.A.Harrison, in "Colliding Beam Studies of Atomic Collision Processes", chapter 4. (Inst.Phys.Conf. Ser.No.38)

18) D.H.Crandall, in "Physics of Ion-Ion and Electron-Ion Collisions", (Plenum, New York, 1983) pp.201.

19) E.Salzborn, in "Physics of Ion-Ion and Electron-Ion Collisions", (Plenum, New York, 1983) pp.239.

20) K.T.Dolder, in "Physics of Ion-Ion and Electron-Ion Collisions", (Plenum, New York, 1983) pp.373.

21) K.T.Dolder, M.F.A.Harrison and P.C.Thonemann, Proc.Roy.Soc. A264 (1961) 367.

22) R.G.Montague and M.F.A.Harrison, J.Phys. B16 (1983) 3045.

23) M.J.Diserens, M.F.A.Harrison and A.C.H.Smith, J.Phys. B17 (1984) L621.

24) R.G.Montague, M.J.Diserens and M.F.A.Harrison, J.Phya. B17 (1984) 2085.

25) R.G.Montague and M.F.A.Harrison, J.Phys. B17 (1984) 2707.

26) M.J.Diserens, Ph.D. Thesis (University College of London, 1984)

27) R.G.Montague and M.F.A.Harrison, J.Phys. B18 (1985) 1419.

28) A.Muller and R.Frodl, Phys.Rev.Lett. 44 (1980) 29.

29) A.Muller, K.Tinschert, C.Achenbach, E.Salzborn, R.Becker, and M.S.Pindzola, Phys.Rev.Lett. 54 (1985) 414.

30) A.Muller, C.Achenbach, E.Salzborn, R.Becker, J.Phys. B17 (1984) 1427.

31) A.Muller et al., unpublished (1985).

32) D.H.Crandall, R.A.Phaneuf, B.E.Hasselquist and D.C.Gregory, J.Phys. B12 (1979) L249.

33) D.H.Crandall, R.A.Phaneuf, R.A.Falk, D.S.Belic and G.H.Dunn,

Phys.Rev. A25 (1982) 143.

34) A.M.Howald, D.C.Gregory, F.W.Meyer, R.A.Phaneuf, A.Muller, N.Djuric, and G.H.Dunn, Phys.Rev. A33 (1986) 3779.

35) D.C.Griffin, C.Bottcher, M.S.Pindzola, S.M.Younger, D.C.Gregory and D.H.Crandall, Phys.Rev. A29 (1984) 1729.

36) M.S.Pindzola, D.C.Griffin, C.Bottcher, D.H.Crandall, R.A.Phaneuf and D.C.Gregory, Phys.Rev. A29 (1984) 1749

37) F.W.Meyer, Nucl.Instrum.Methods Phys.Res., Sect. B9 (1985) 532.

38) A.M.Howald, D.C.Gregory, R.A.Phaneuf D.H.Crandall and M.S.Pindzola, Phys.Rev.Lett. 56 (1986) 1675.

39) R.A.Phanefu and D.C.Gregory, Proceedings of the Joint Workshop of the US-Japan Fusion Collaborative Program, (Nagoya, 1986) to be published in IPPJ-AM (1986).

40) A.Danjo, A.Matsumoto, S.Ohtani, H.Suzuki, H.Tawara, K.Wakiya, and M.Yoshino, J.Phys.Soc.Jpn. 53 (1984) 4091.

41) H.Suzuki, Proceedings of the Joint Workshop of the Us-Japan Fusion Collaborative Program, (Nagoya, 1986) to be published in IPPJ-AM (1986).

42) I.Yamada et al., to be published.

43) K.T.Dolder and B.Peart, Rep. Prog. Phys. 39 (1976) 693.

44) P.Defrance, F.Brouillard, W.Claeys and G.Van Wassenhove, J. Phys. B14 (1981) 103.

45) A.Muller, K.Huber, K.Tinschert, R.Becker and E.Salzborn, J. Phys. B18 (1985) 2993.

46) N.F.Mott and H.S.W.Massey, "The Theory of Atomic Collisions" (Oxford University Press, 1965).

47) M.R.Rudge, Rev.Mod.Phys. 40 (1968) 564.

48) Y.K.Kim, in "Physics of Ion-Ion and Electron-Ion Collisions", (Plenum Press, New York, 1983) pp.101.

49) J.J.Thomson, Phil.Mag. 23 (1912) 449.

50) B.K.Thomson and D.J.Garcia, Phys.Rev. 179 (1969) 94.

51) M.Grizinski, Phys.Rev. 115 (1959) 374.

52) A.Burgess, Proceedings of 3rd International Conference on the Physics of Electronic and Atomic Collisions, ed. M.R.C.McDowell, (North Holland, 1964) pp.63.

53) K.Alder, T.Huus, B.Mottelson and A.Winter, Rev.Mod.Phys. 28 (1956) 432.

54) H.Bethe, Ann.d.Phys. 5 (1930) 325.

55) P.G.Burke and A.J.Taylor, Proc.Roy.Soc. A287 (1965) 105.

56) L.B.Golden and D.H.Sampson, J.Phys.B10 (1977) 2229.

57) D.H.Sampson and L.B.Golden, J.Phys.B11 (1978) 541.

58) S.M.Younger, Phys.Rev. A22 (1980) 111.

59) S.M.Younger, Atomic Data for Fusion, 6 (1981) 190.

60) R.F.Post, Plasma Physics, 3 (1961) 273.

61) M.J.Seaton, Proc.Phys.Soc. 79 (1964) 1105.

62) W.Lotz, Z.Phys. 206 (1967) 205.

63) W.Lotz, Z.Phys. 216 (1968) 241.

64) W.Lotz, Z.Phys. 232 (1970) 101.

65) L.Valyi, "Atom and Ion Sources", (John Wiley and Sons, London, 1977).

66) R.E.Weber and L.F.Cordes, Rev.Sci.Instrum. 37 (1966) 112.

67) K.N.Kingdon, J.Langmuir, Phys.Rev. 21 (1923) 380.

68) Y.Sakai, I.Katsumata and T.Oshio, Jpn.J.App.Phys. 22 (1983) 1048.

69) Lyon and B.Peart, J.Phys. E17 (1984) 920.

70) J.R.Pierce, Theory and Design of Electron Beams, (New York, London, Van-Nostrand, 1954).

71) K.Rinn, A.Muller, H.Eichenauer and E.Salzborn, Rev.Sci.Instrum. 53 (1982) 829.

72) S.Takagi, Y.Kawasumi, N.Noda and J.Fujita, Jpn.J.App.Phys. 22 (1983) 1453.

73) T.Hirayama, K.Oda, Y.Morikawa, T.Ono, Y.Ikezaki, T.Takayanagi, K.Wakaiya and H.Suzuki, J.Phys.Soc.Jpn. 55 (1986) 1411.

74) B.Peart and K.T.Dolder, J.Phys. B1 (1968) 240.

75) J.W.Hooper, W.C.Lineberger and F.M.Bacon, Phys.Rev. 141 (1966) 165.

76) D.L.Moores, J.Phys. B5 (1972) 286.

77) S.M.Younger, Phys.Rev. A23 (1981) 1138.

78) H.Aizawa, K.Wakiya, H.Suzuki, F.Koike and F.Sasaki, J.Phys. B18 (1985) 289.

79) S.M.Younger, Phys.Rev. A26 (1982) 3177.

80) B.Peart and K.Dolder, J.Phys. B8 (1975) 56.

81) J.E.Hansen, J.Phys. B8 (1975) 2759.

82) E.Clementi and C.Roetti, Atomic Data and Nuclear Data Tables, 14 (1974) 177.

83) B.Peart and K.T.Dolder, J.Phys. B1 (1968) 872.

84) R.K.Feeney, J.W.Hooper and M.T.Elford, Phys.Rev. A6 (1972) 1469.

85) B.Peart, J.G.Stevenson and K.T.Dolder, J.Phys. B6 (1973) 146.

86) D.C.Griffin, M.S.Pindzola and C.Bottcher, J.Phys. B17 (1984) 3183.

87) G.H.Dunn, in "The Physics of Ionized Cases SPIG, 1980", ed. M.Matic, (Boris Kidric Institute of Nuclear Sciences, Beograde, 1981), pp.49.

88) W.E.Sayle II and R.K.Feeney, Proc. 13th Int. Conf. Physics of Electronic and Atomic Collisions, Paris, 1977 (ICPEAC, Paris 1977) pp.1084.

89) W.Mehlhorn, B.Breuckmann and D.Hausamann, Phys.Scr. 16 (1977)

177.

90) S.M.Younger, (private communications)

91) T.B.Lucatorto, T.J.McIlrath, J.Sugar and S.M.Younger, Phys. Rev.Lett. 47 (1981) 1124.

92) Ch.Achenbach, A.Muller, E.Salzborn and R.Becker, Phys.Rev. Lett. 50 (1983) 2070.

93) D.R.Hertling, R.K.Feeney, D.W.Hughes and W.E.Sayle II, J. Appl.Phys. 53 (1982) 5427.

94) T.Takayanagi, C.Takayanagi, A.Nakashio and H.Kimura, submitted to J.Phys.B.

95) H.Suzuki, T.Takayanagi, K.Morita and Y.Iketaki, in "Electron-Molecule Collisions and Photoionization Processes", ed. V.McKoy, H.Suzuki, K.Takayanagi and S.Trajmar, (Verlag Chemie International Inc., 1983) pp.43.

96) S.M.Younger, Phys.Rev. A22 (1980) 111.

97) S.M.Younger, Phys.Rev.Lett. 56 (1986) 2618.

98) S.M.Younger, Phys.Rev. A, to be published.

99) R.K.Peterkop, Zh.Eksp.Teor.Fiz. 41 (1961) 1938, [Sov.Phys. JETP. 14 (1962) 1377.]

100) B.Peart and K.T.Dolder, J.Phys. B2 (1969) 1169.

101) D.W.Hughes and R.K.Feeney, Phys.Rev. A23 (1981) 2241.

102) B.L.Schram, Physica, 32 (1966) 197.

103) M.Ardenne, in "Tabellen zur Angewandten Physik", vol.1, (Berlin; VEB Deutscher Verlag der Wissen Shaften) pp.582.

104) R.A.Falk and G.H.Dunn, Phys.Rev. A27 (1983) 754.

105) D.H.Crandall, R.A.Phaneuf, R.A.Falk, D.S.Belic, G.H.Dunn, Phys.Rev. A25 (1982) 143.

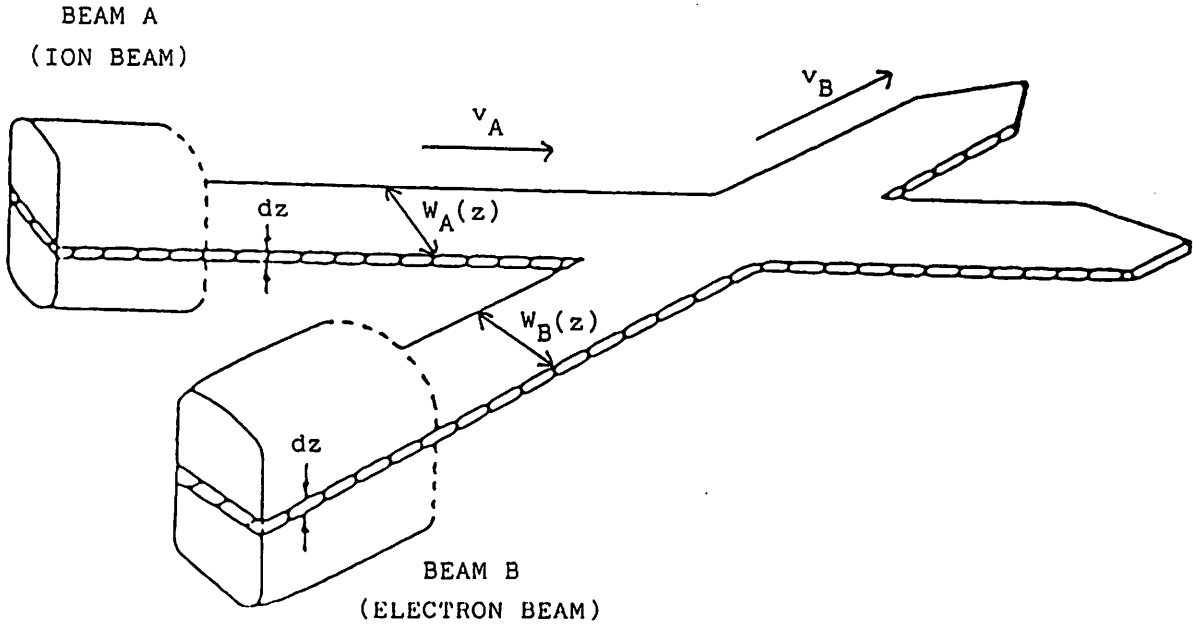

Fig.1-1. Beam configuration at the collision region.

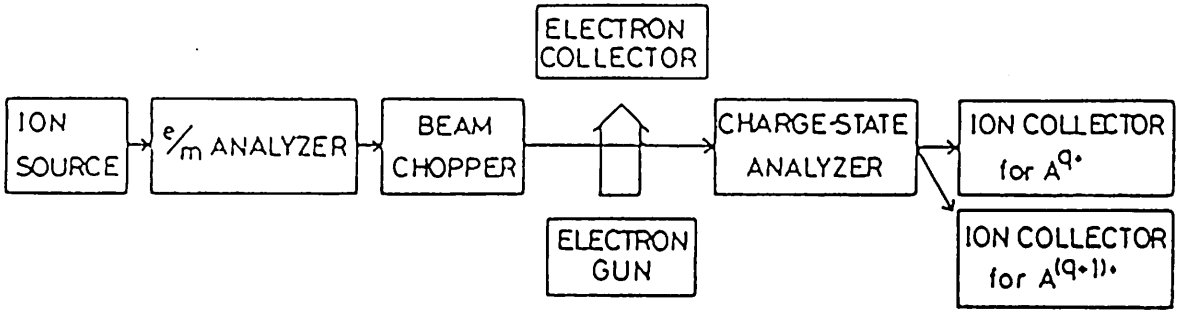

Fig.2-1. Principle of the crossed-beam apparatus.

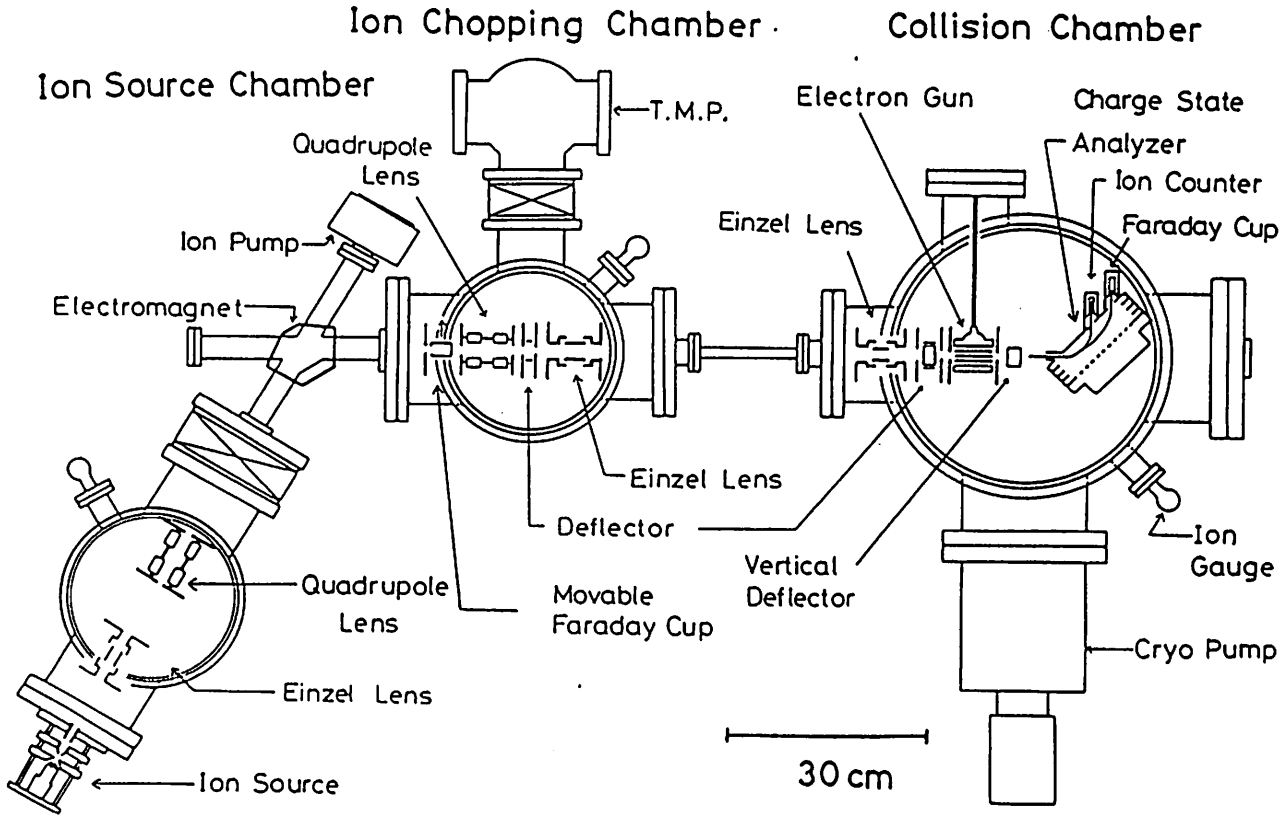

Fig.4-1. Schematic view of the crossed-beam apparatus used for the alkali measurements.

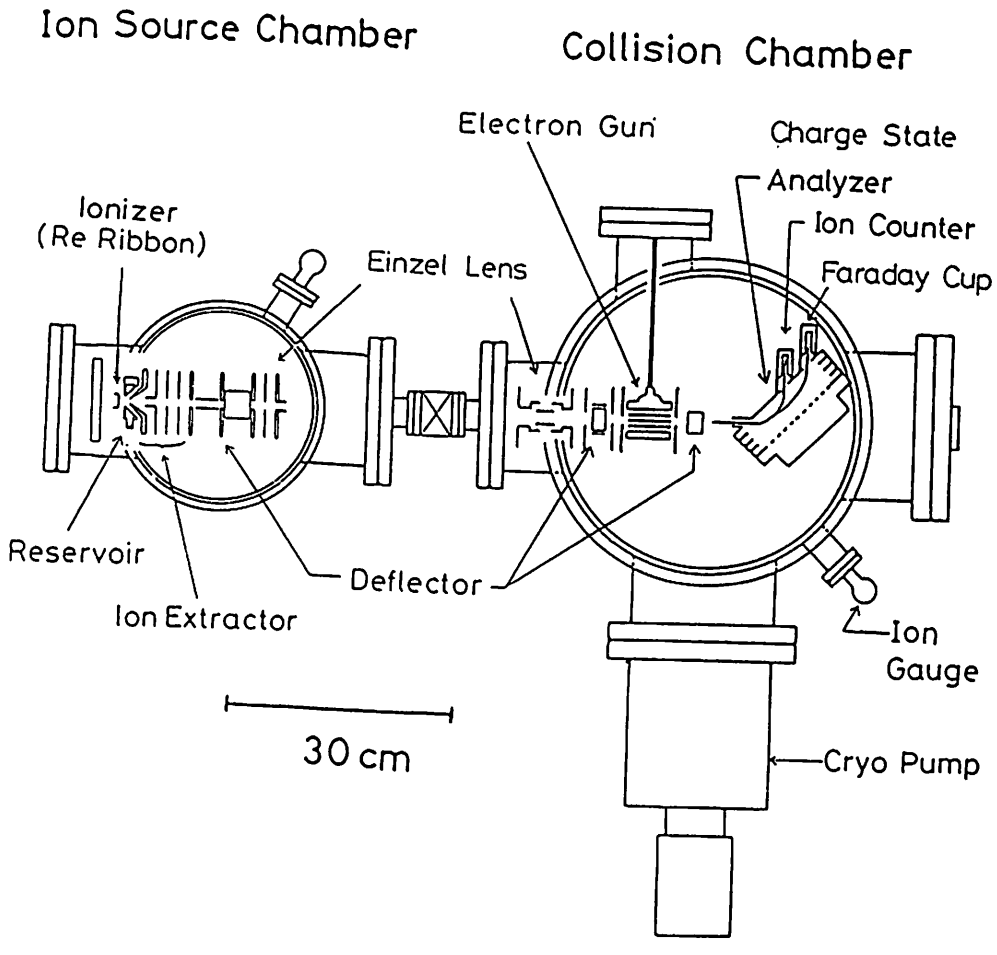

Fig.4-2. Schematic view of the crossed-beam apparatus used for the alkaline earth measurements.

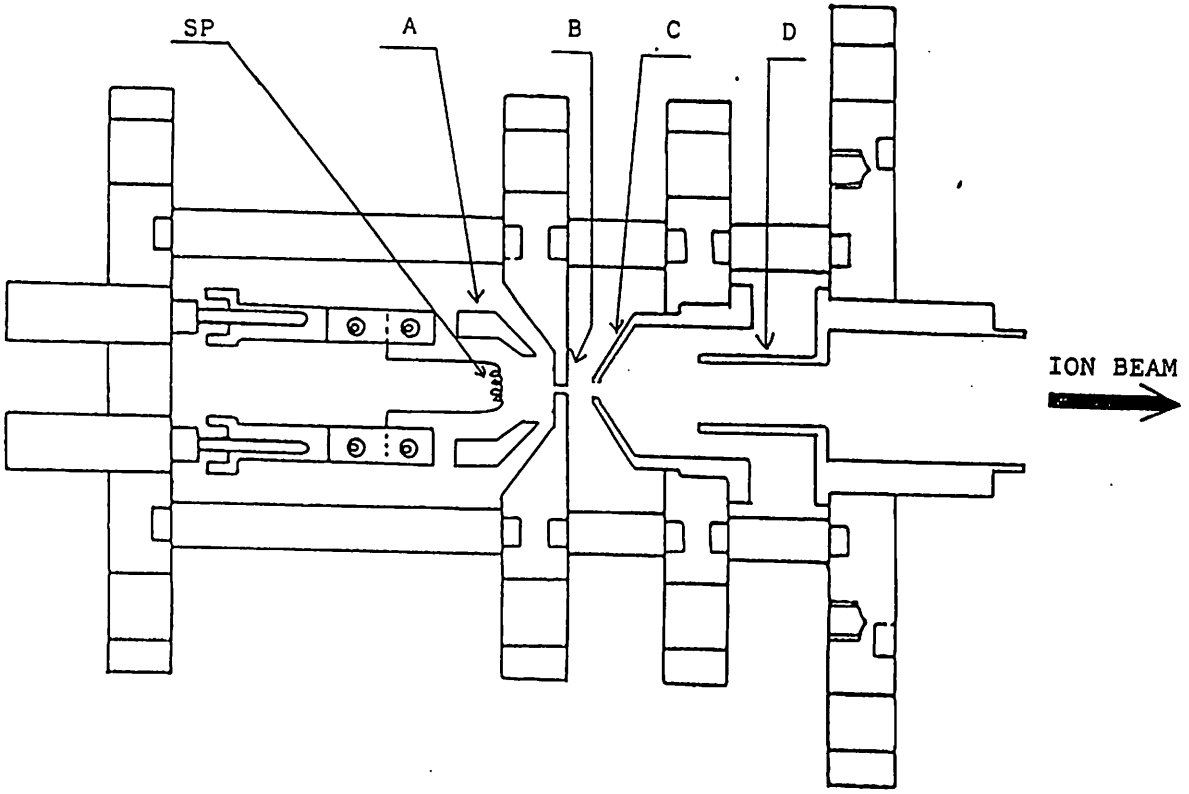

Fig.4-3. Schematic view of the thermionic emission type ion source.

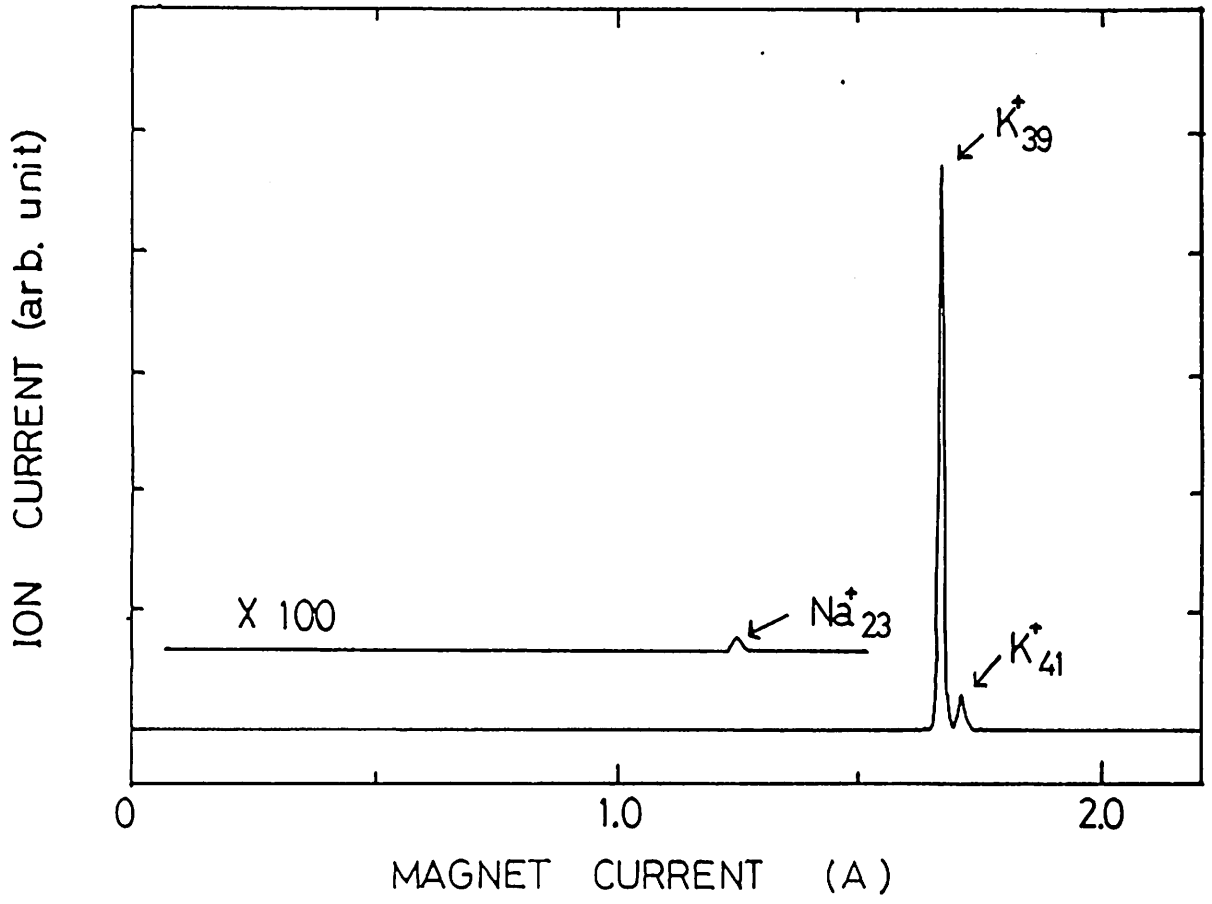

Fig.4-4. Mass spectrum for K^+ ion.

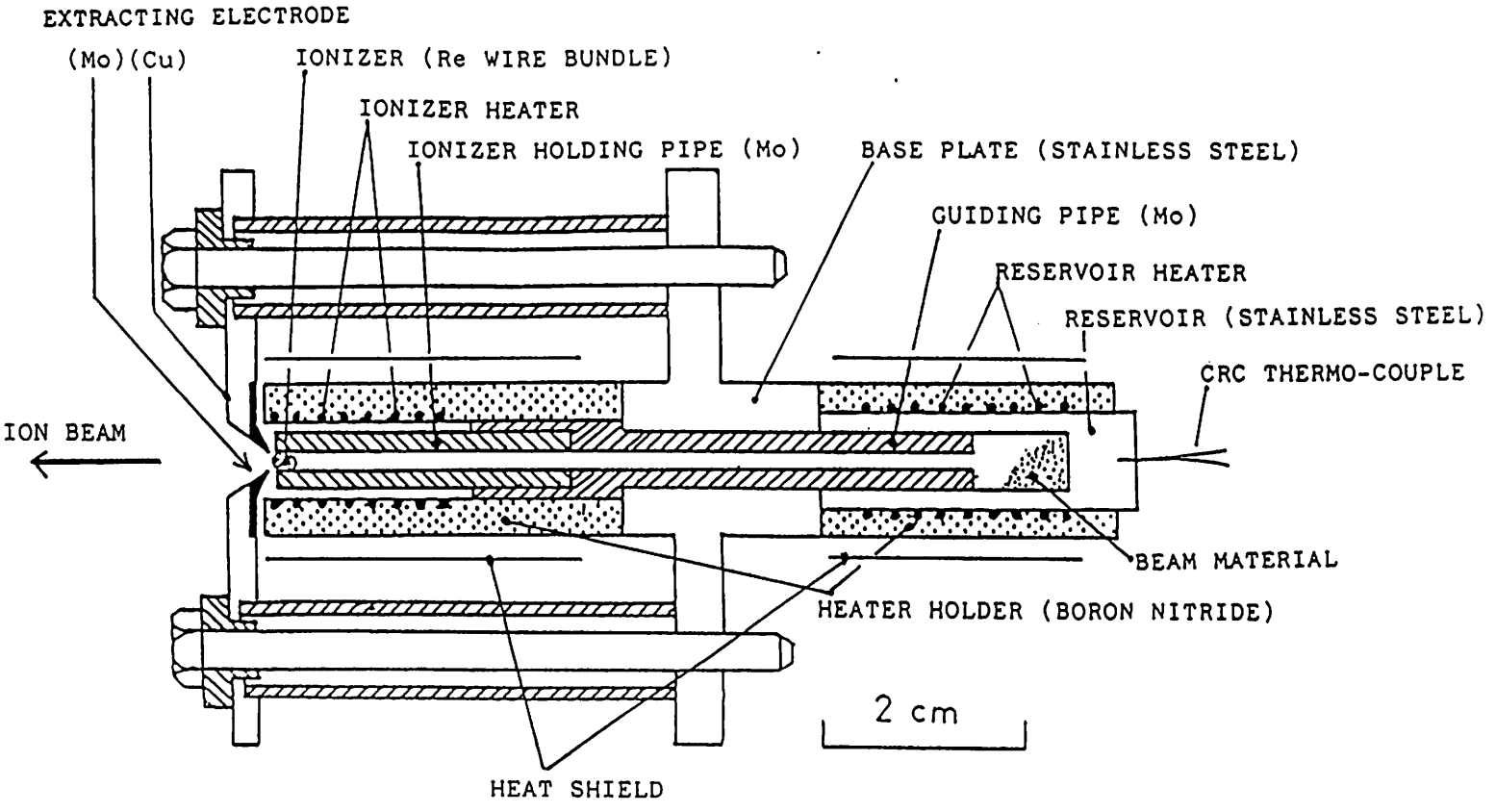

Fig.4-5. Schematic of the surface ionization type ion source.

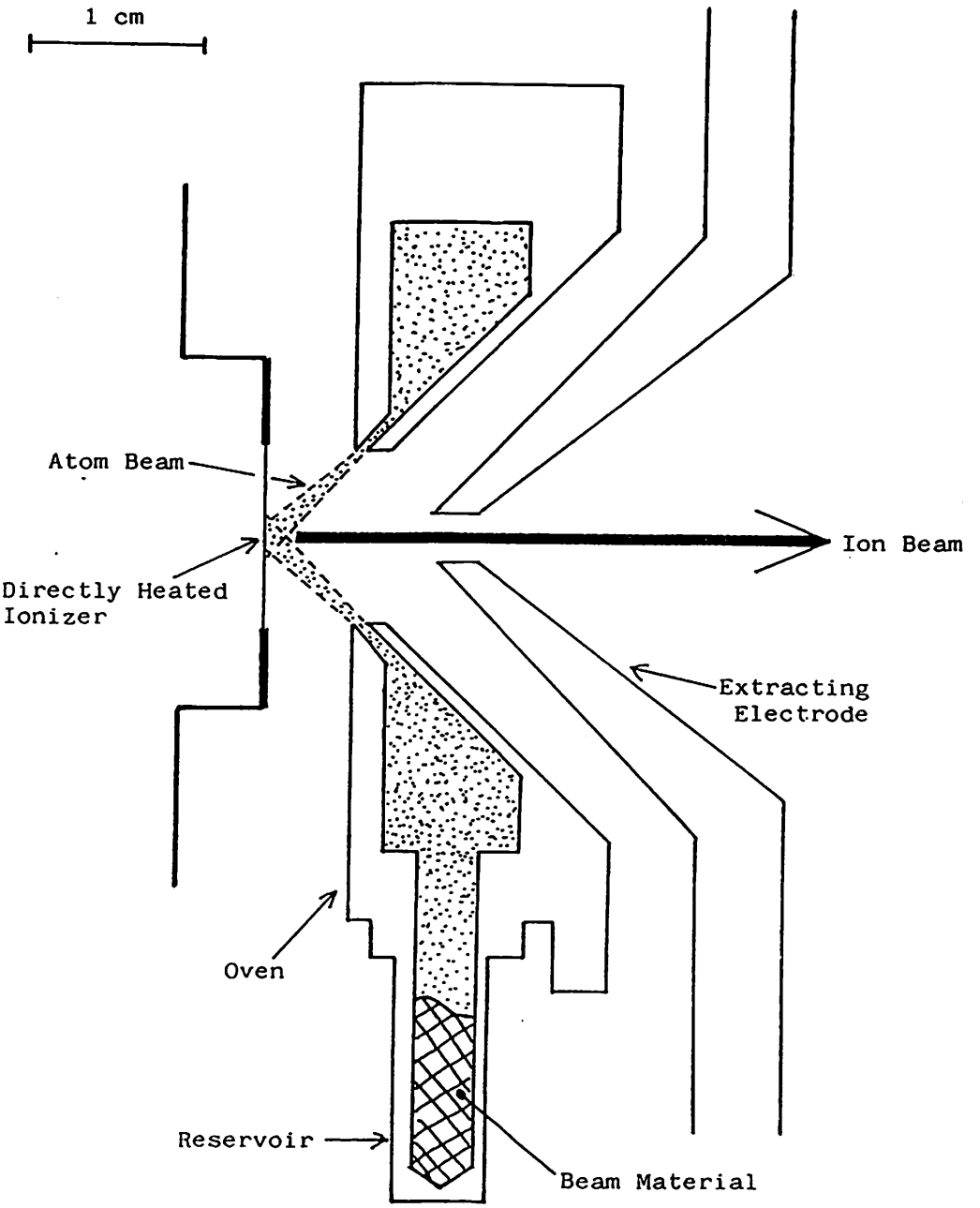

Fig.4-6. Schematic of the ionizer region of the surface ionization type ion source with circular slit.

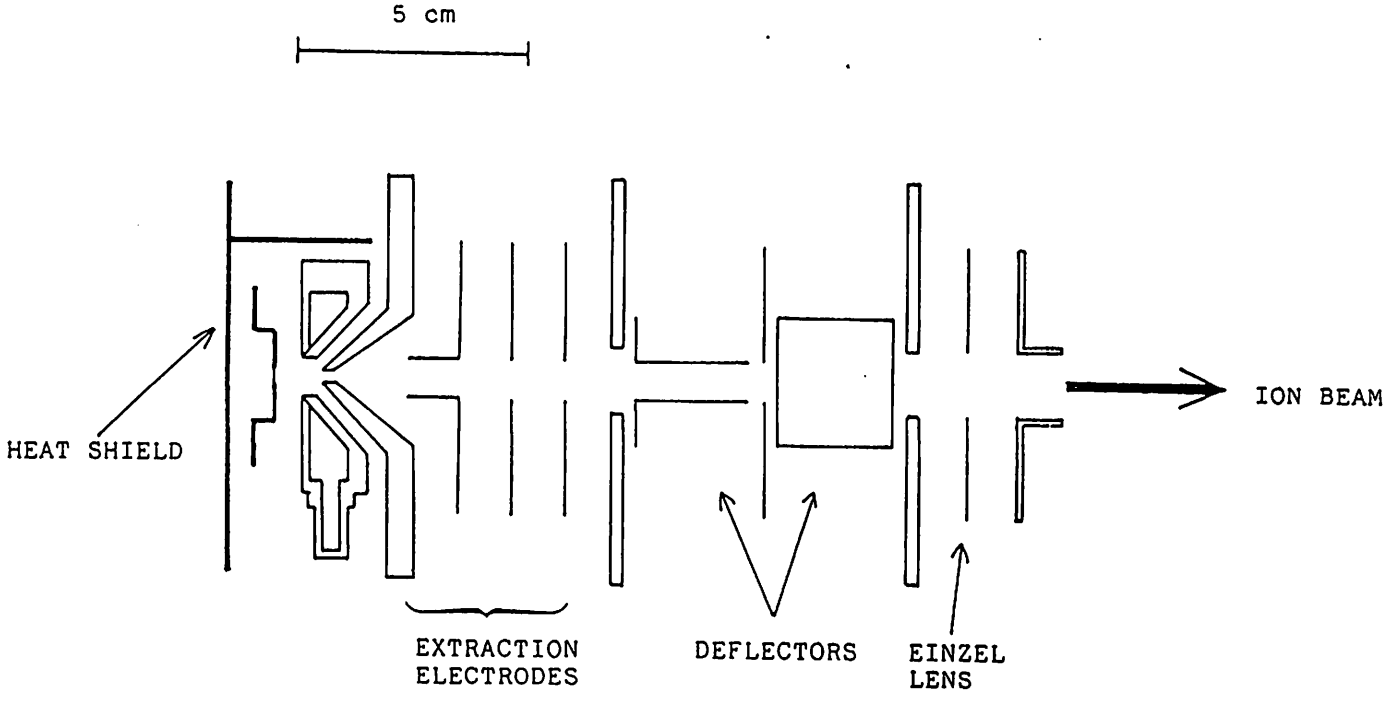

Fig.4-7. Surface ionization type ion source and lens optics in the ion source chamber.

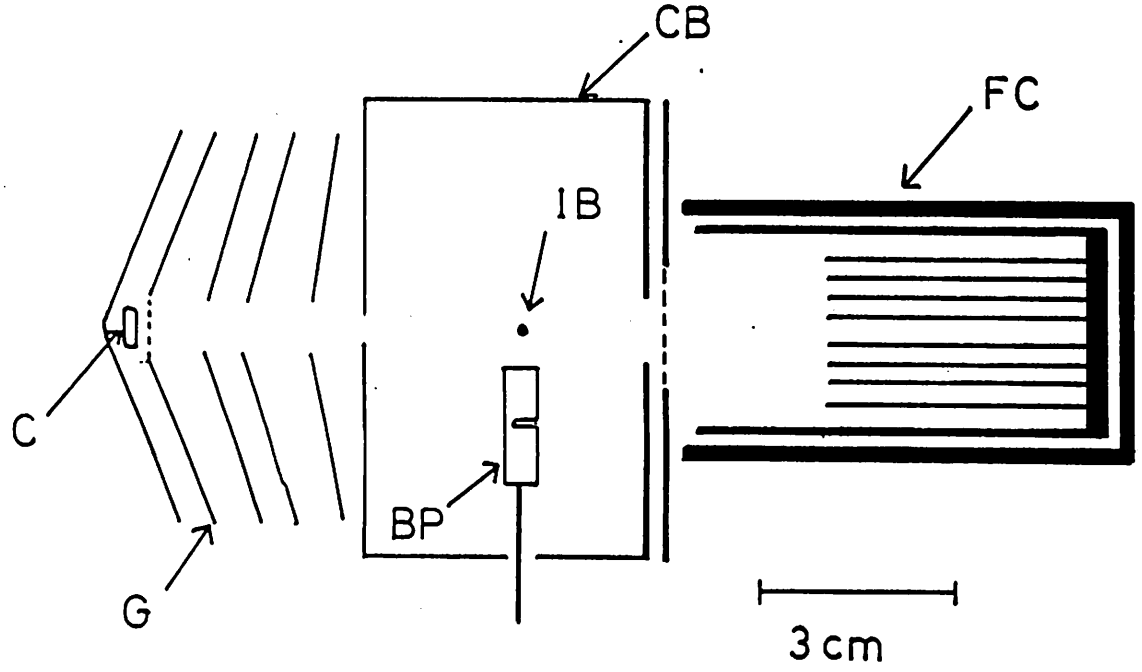

Fig.4-8. Side view of the electron gun including the collision region and the Faraday cup. C ; oxide-coated cathode, G ; Grid, BP ; Beam probe, IB ; Ion beam, CB ; Collision box, FC ; Faraday cup.

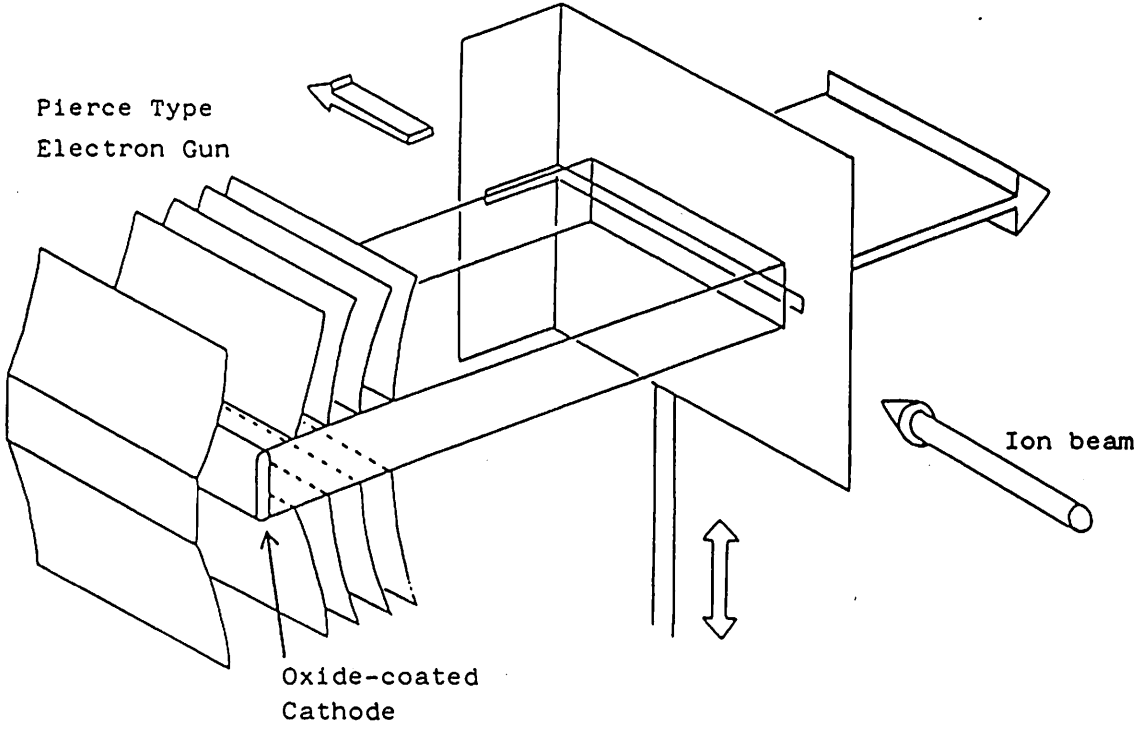

Fig.4-9. L-shape slit scanner.

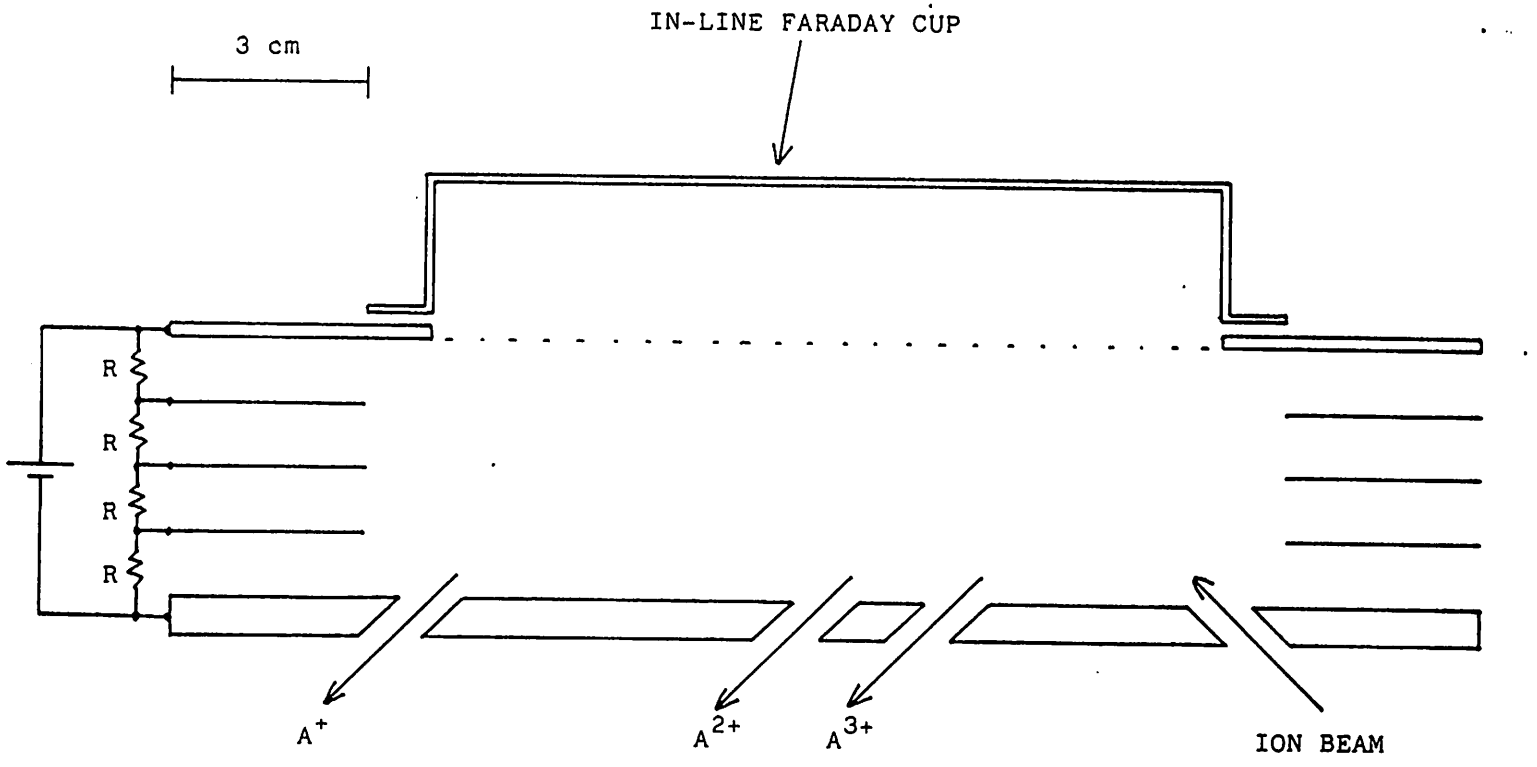

Fig.4-10. Schematic of the paralle plate charge state analyzer.

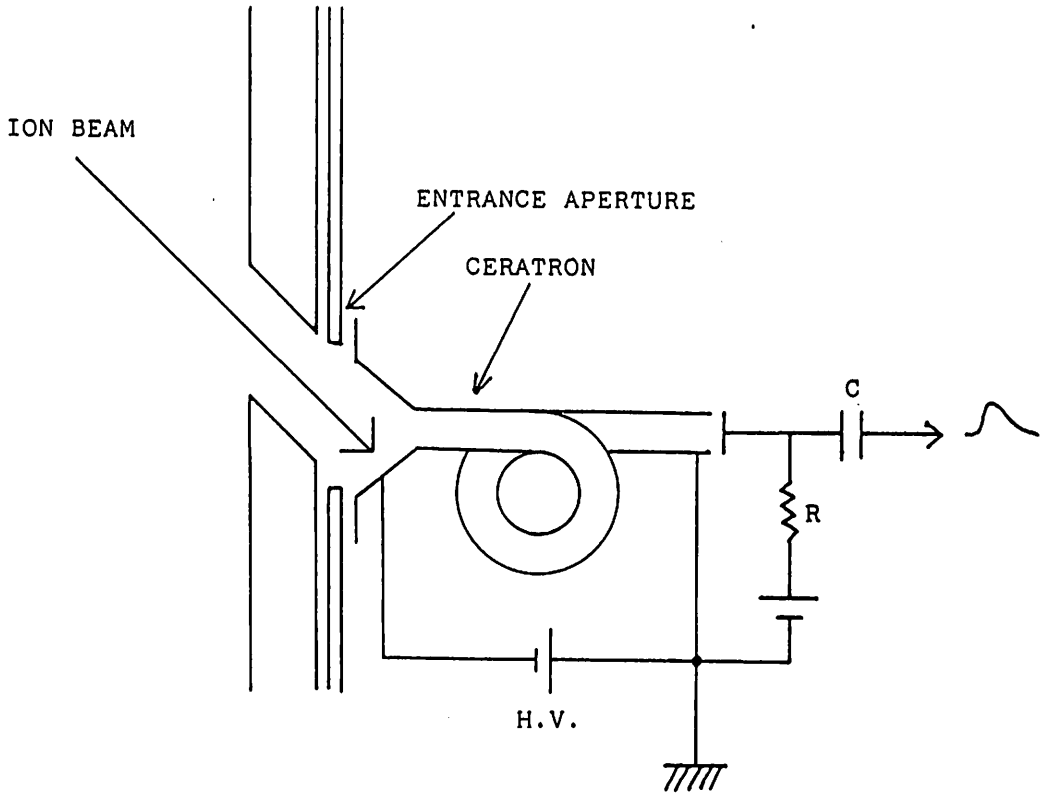

Fig.4-11. Direct incident type product ion detector.

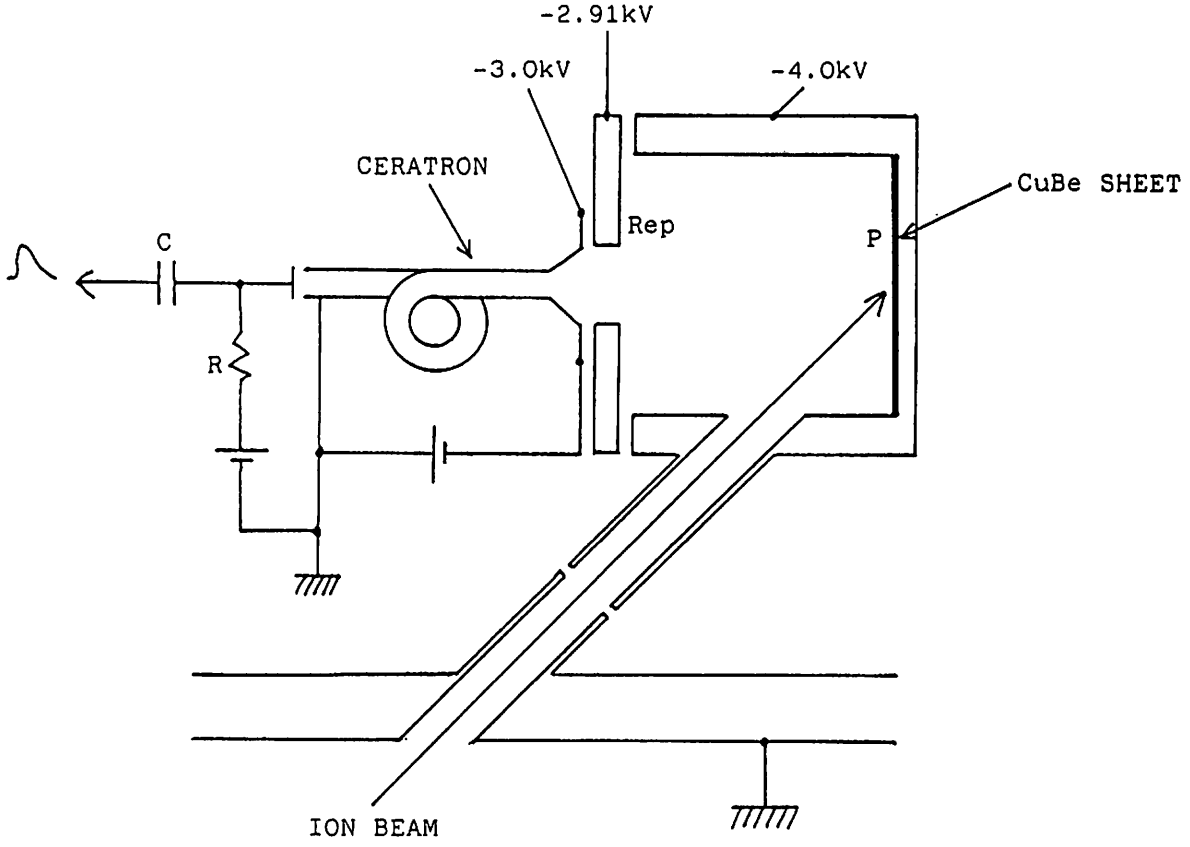

Fig.4-12. Product ion detector with secondary electron converter. P ; secondary electron converter made of CuBe, Rep ; repeller electrode. Typical operation voltages are also shown.

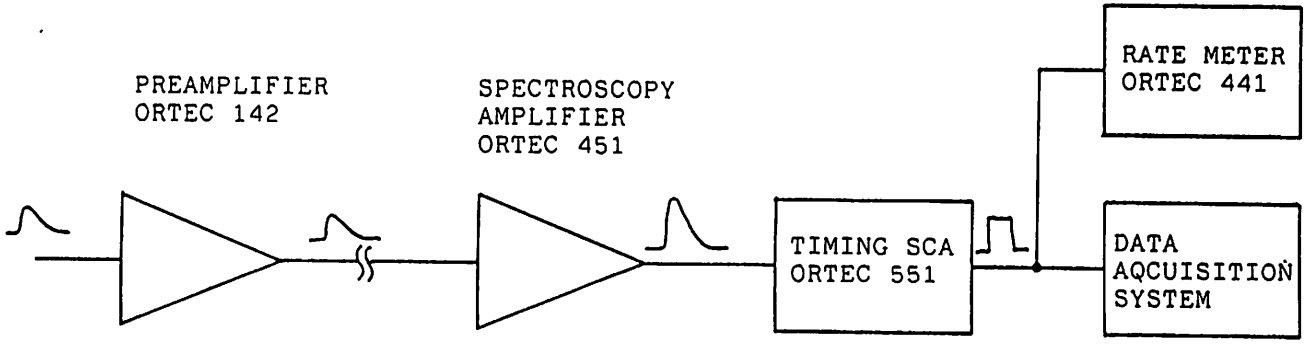

Fig.4-13. Pulse counting electronic chain.

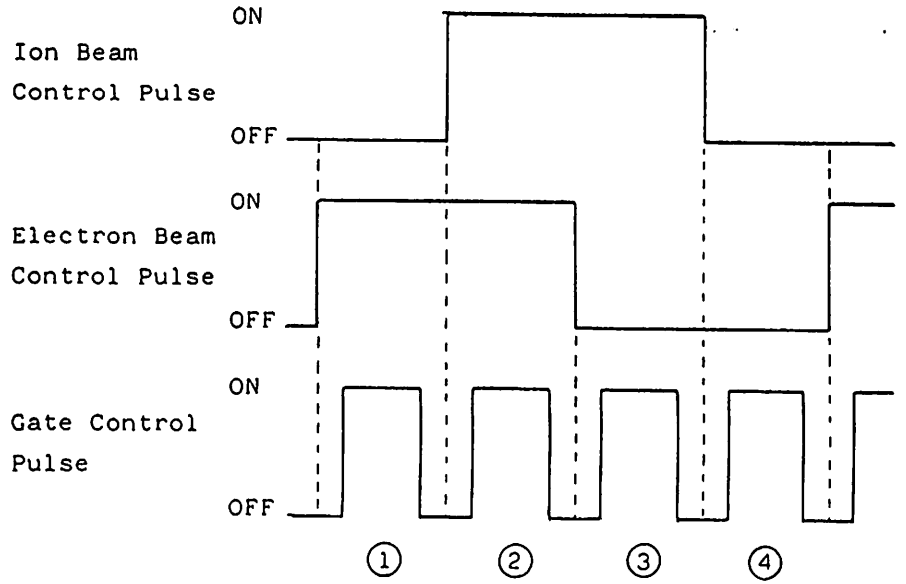

$S_T = (②+④) - (①+③)$

$S_i = ③ - ④$

$S_e = ① - ④$

$S_B = ④$

Fig.4-14. Pulsing sequence for the double beam chopping mode.

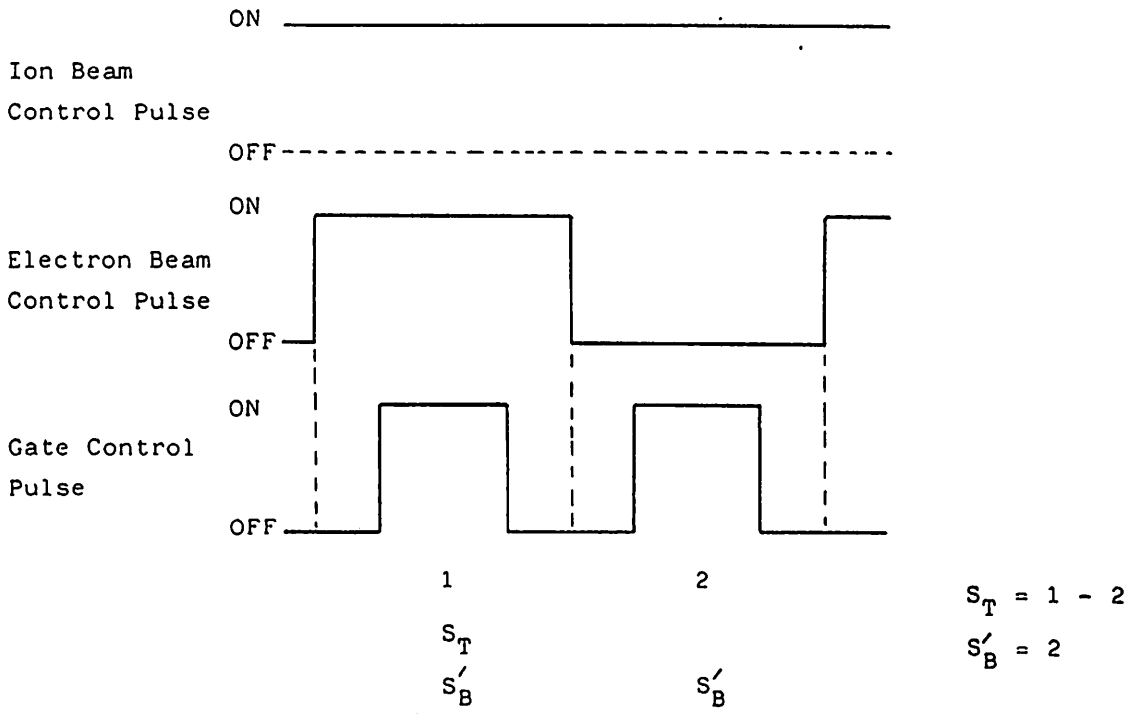

Fig.4-15. Pulsing sequence for the single beam chopping mode.

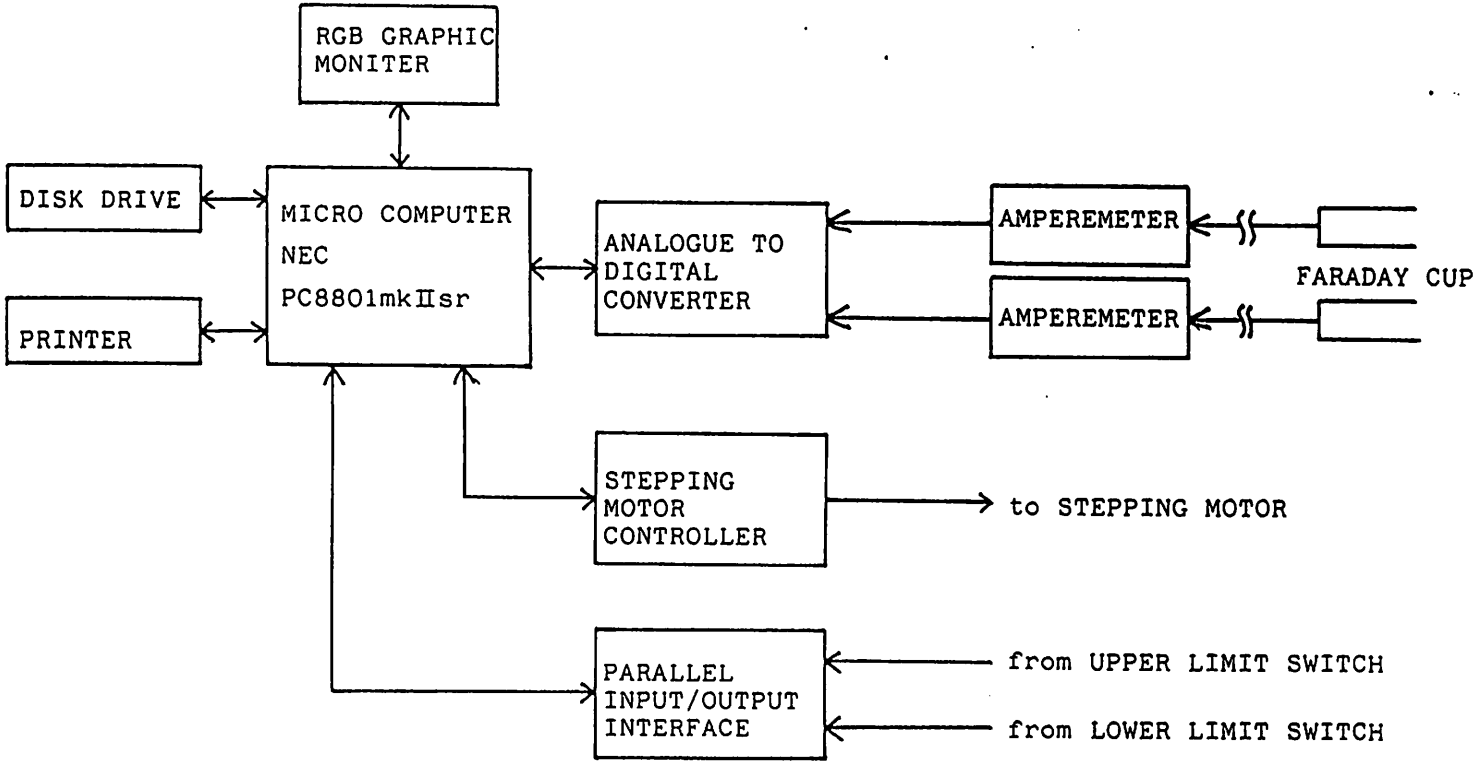

Fig.4-16.Block diagram of the system for the measurements of the form factor.

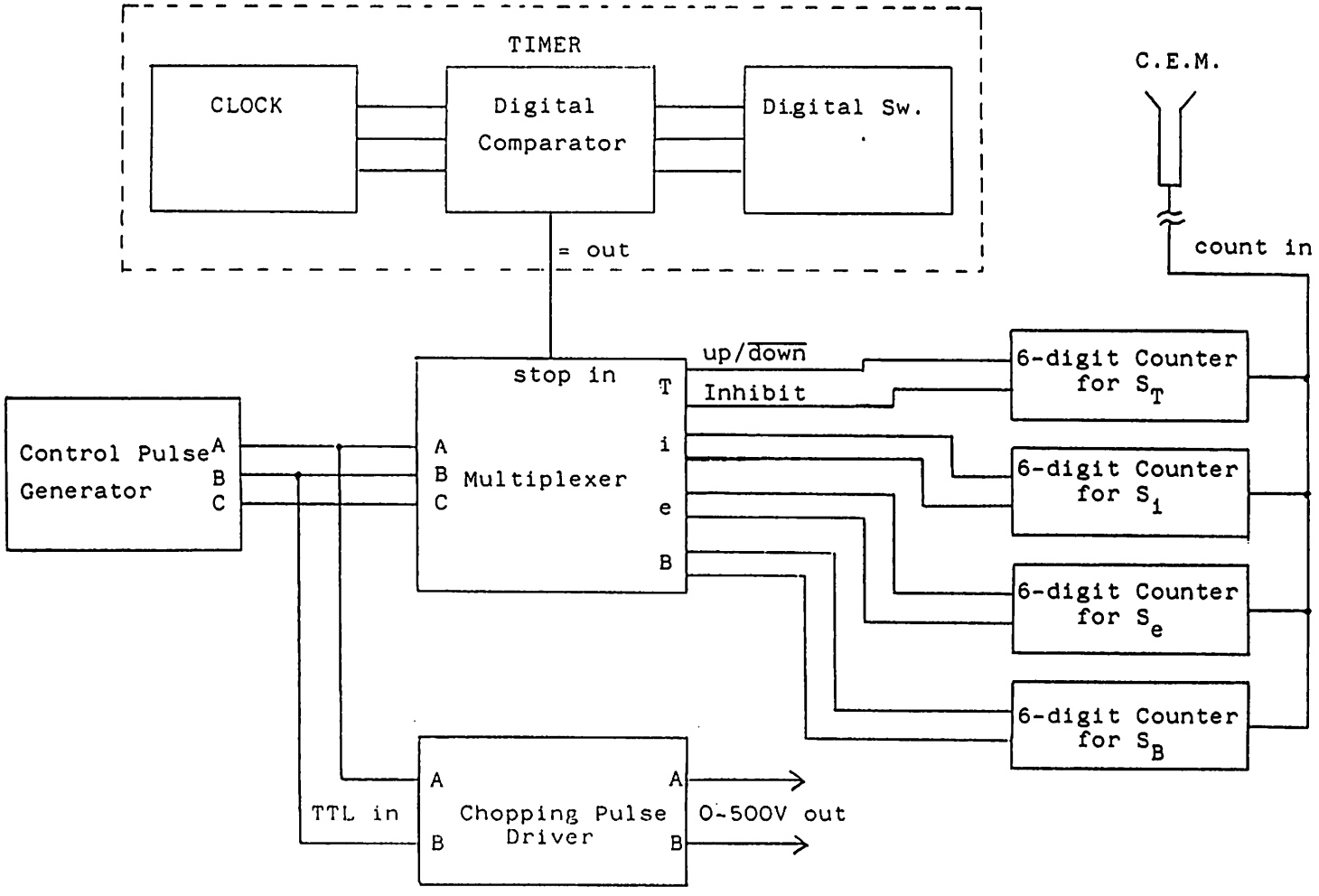

Fig.4-17. Block diagram of the data acquisition system.

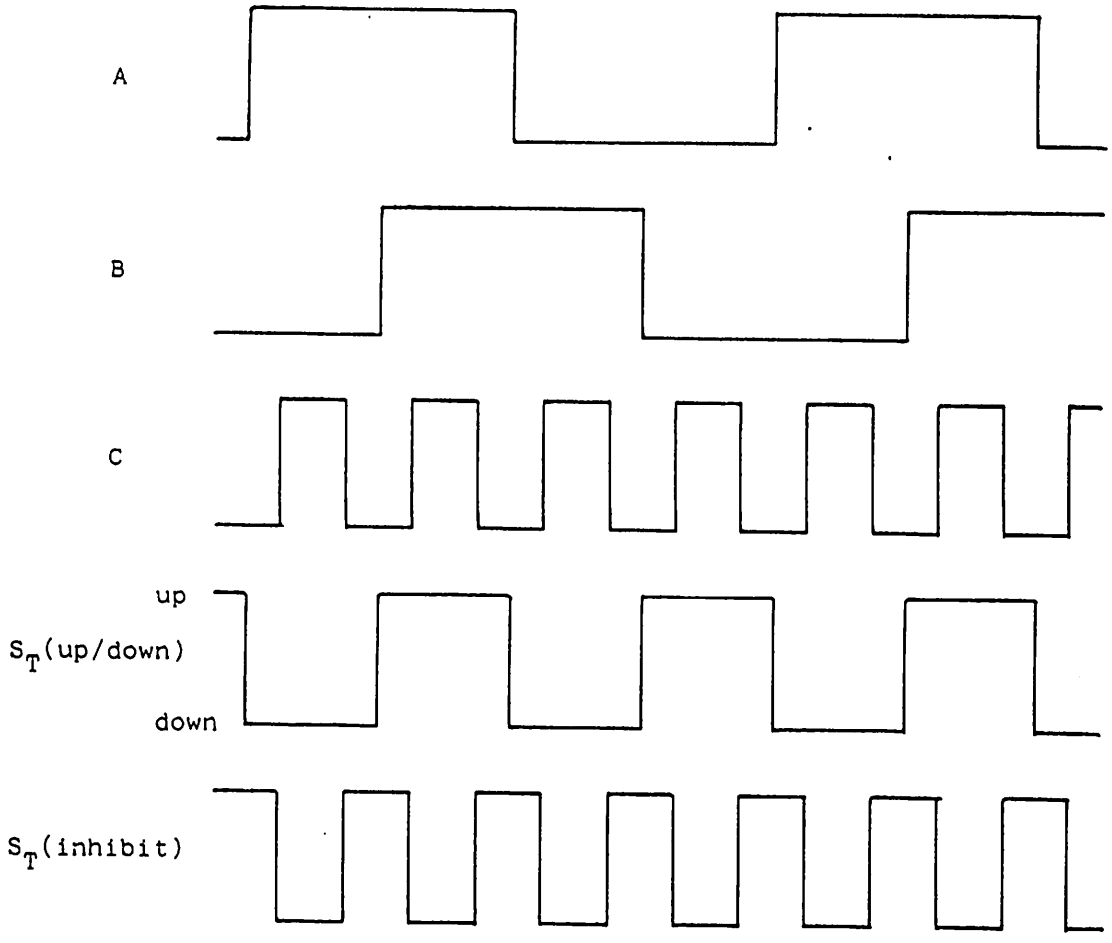

Fig.4-18. Control pulse sequence for S_T.

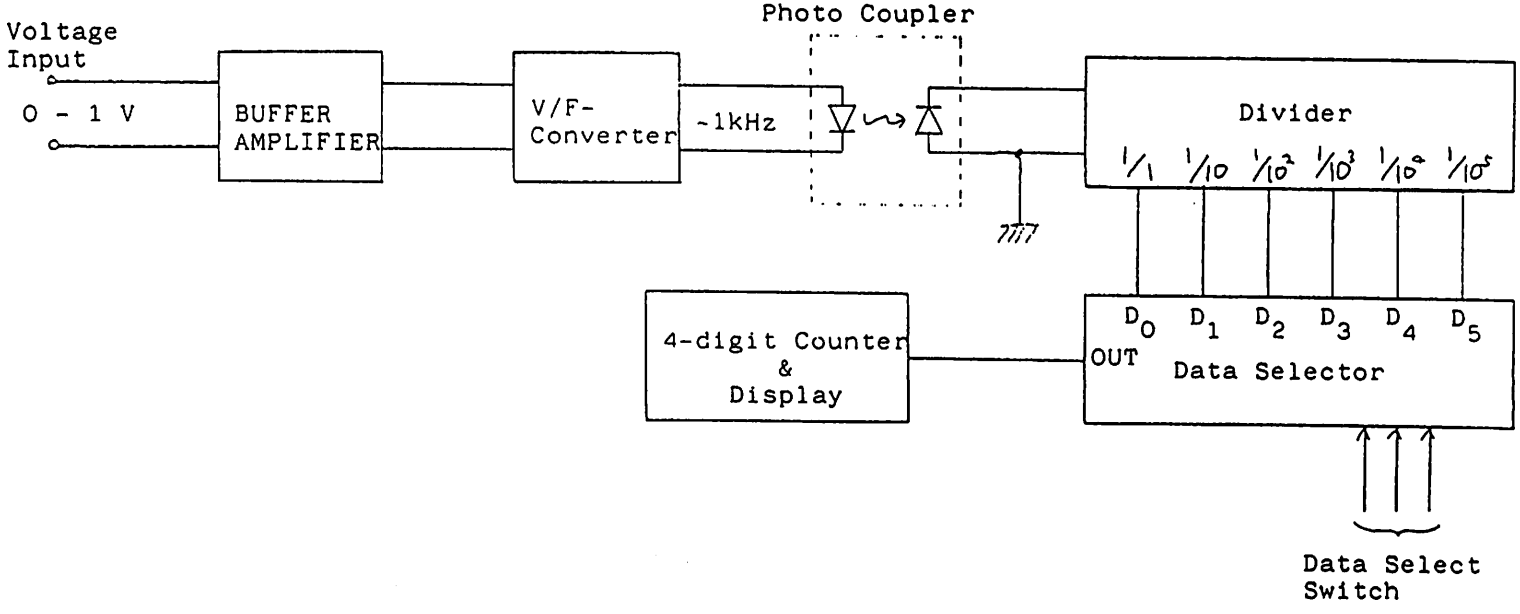

Fig.5-1. Block diagram of the current integrator.

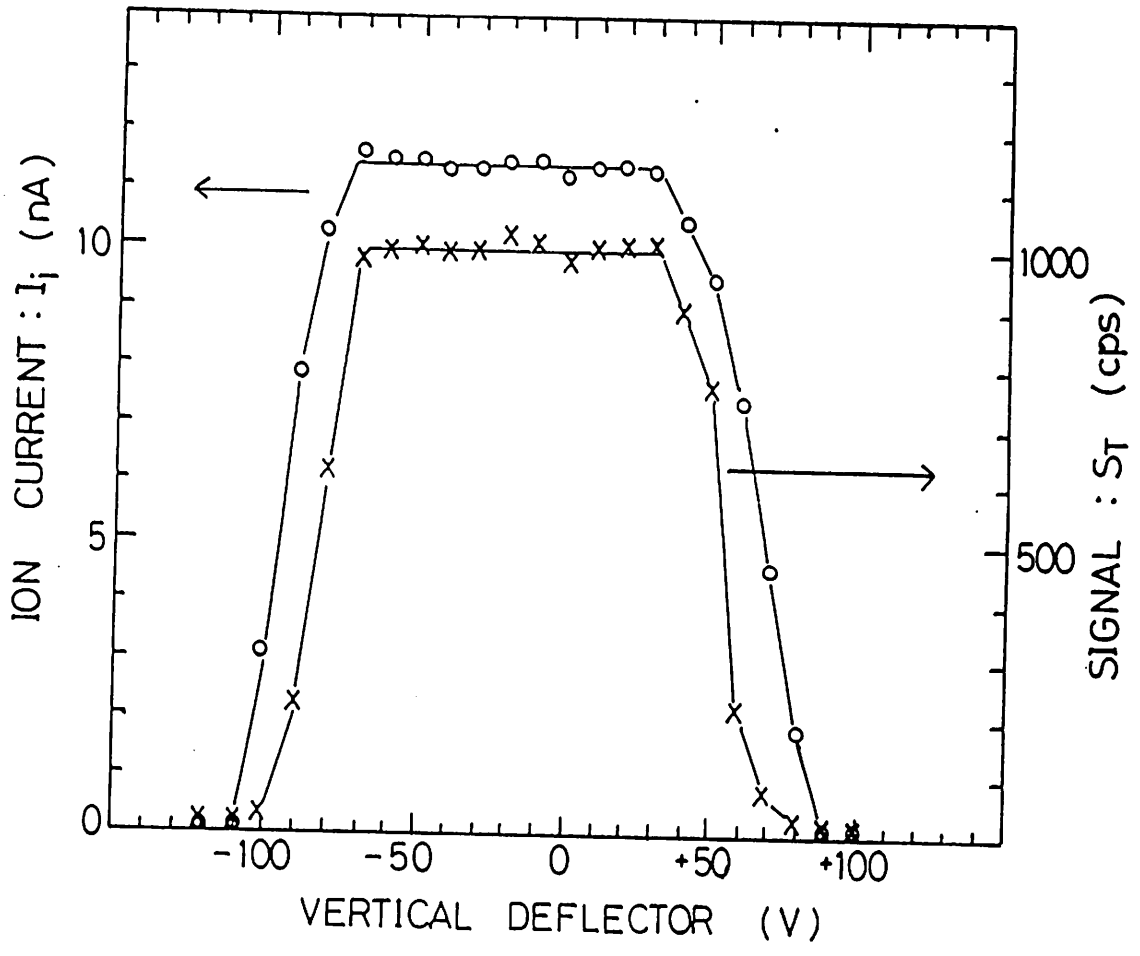

Fig.5-2. Vertical scanning of the ion beam for the transemission check.

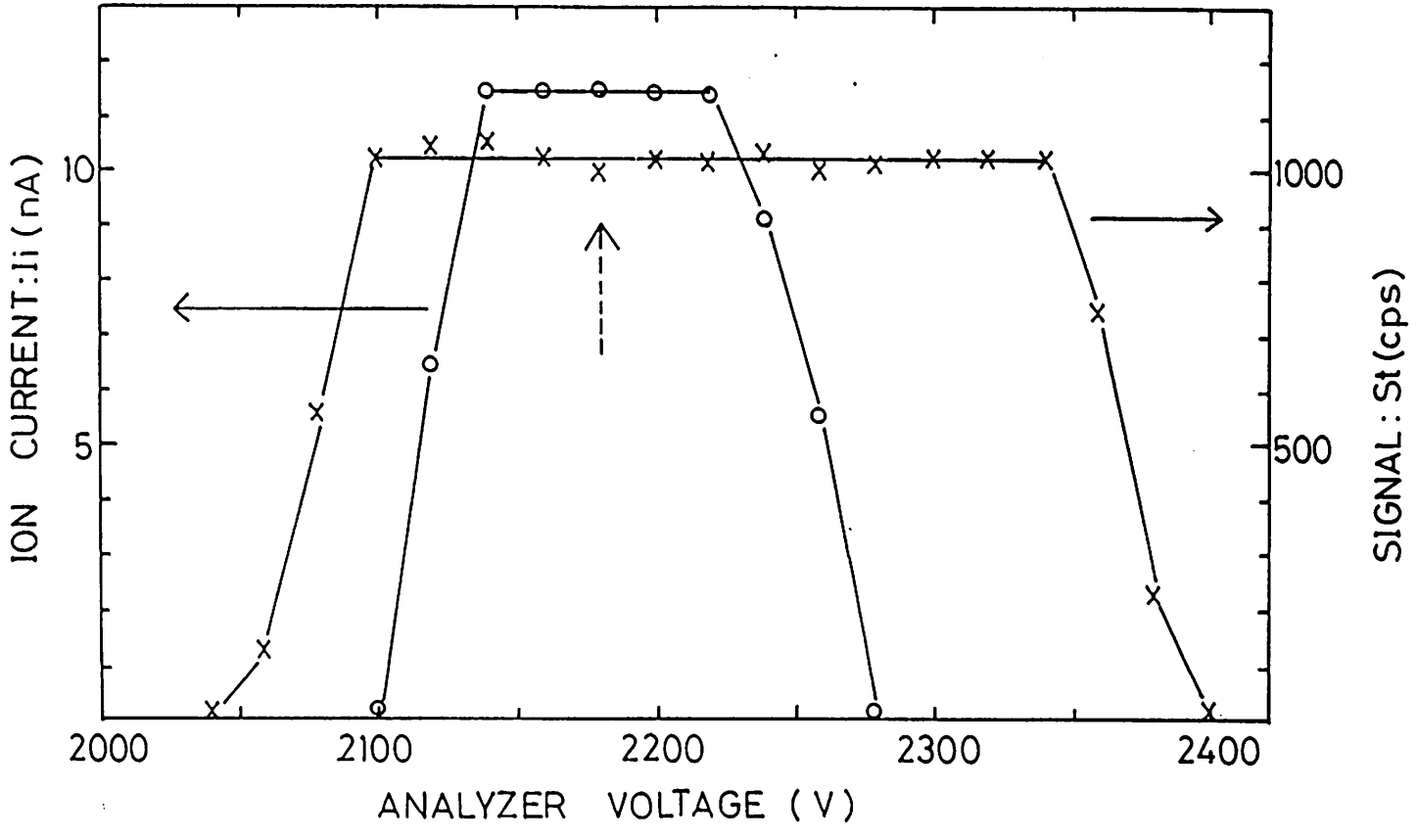

Fig.5-3. Horizontal scanning of the ion beam for the transmission check. The broken arrow indicates the operation voltage.

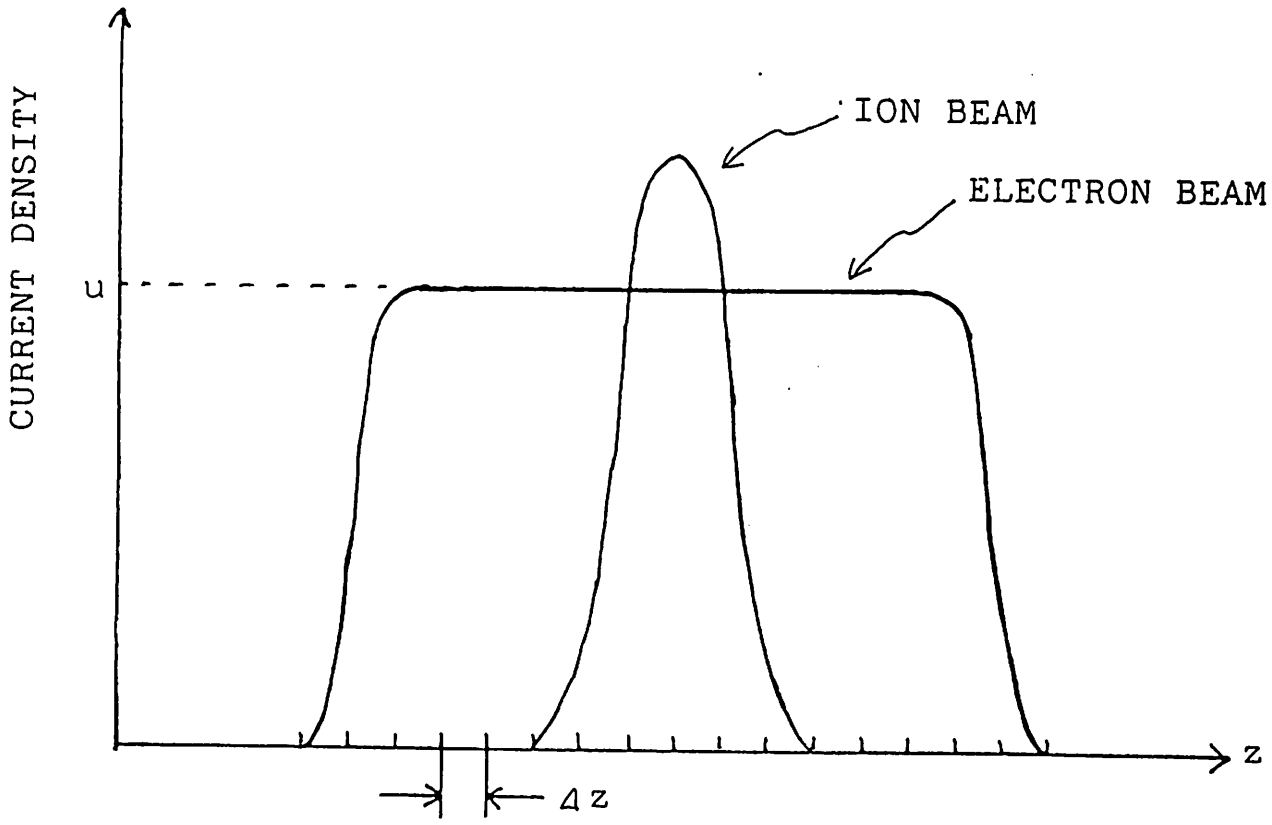

Fig.5-4. Density profile with top-flat electron beam.

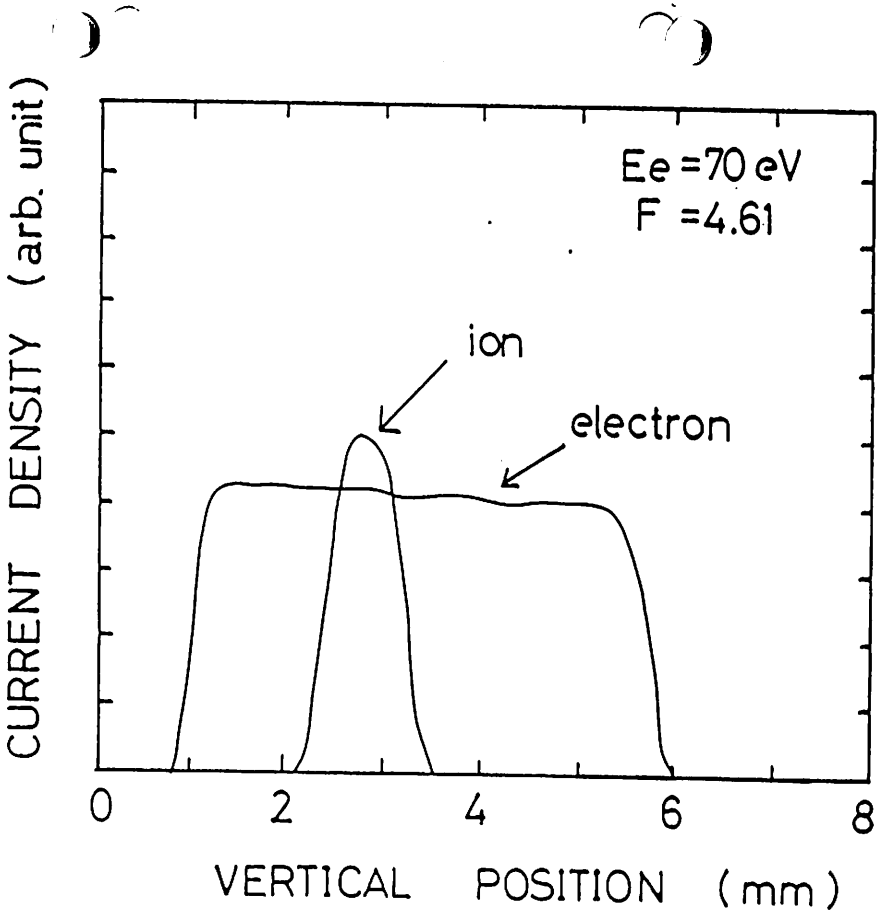

Fig.5-5. Typical example of the measured density profiles at electron energy 70 eV.

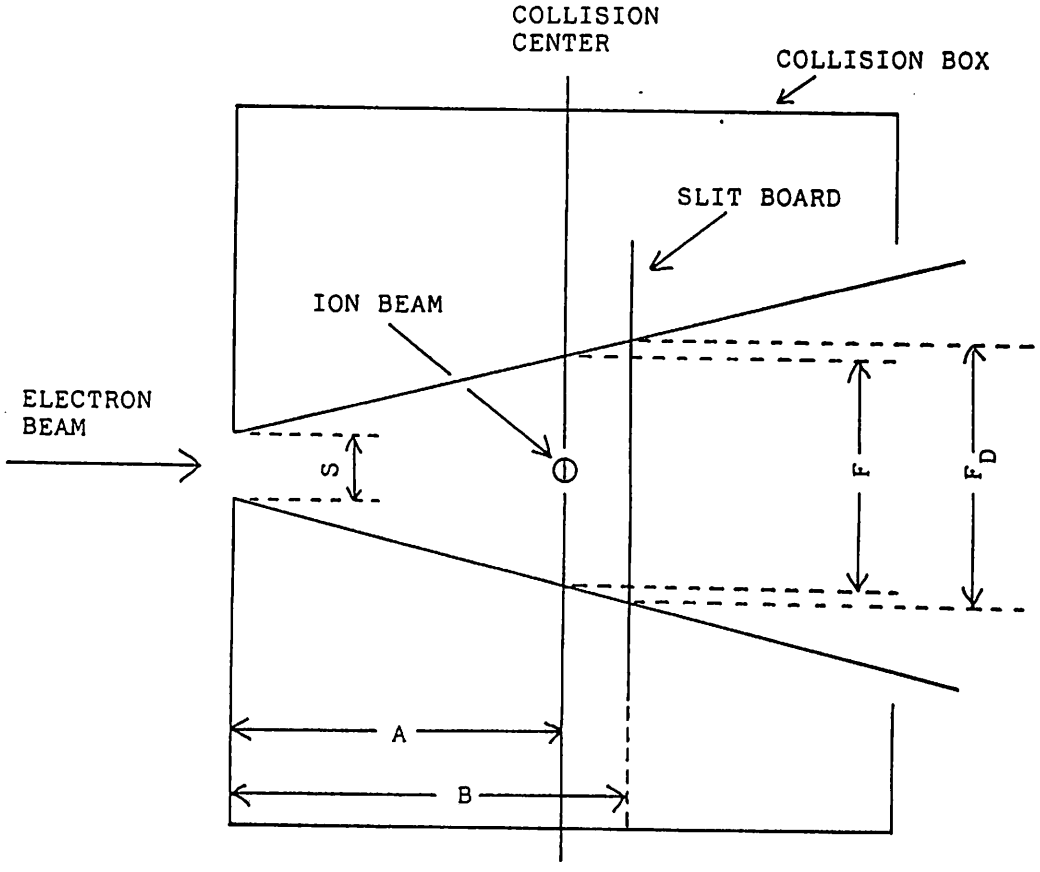

Fig.5-6. Geometrical interpolation of the form factor. The form factor at the collision region is calculated using the measured form factor F_D with the L-shape slit as $F = A(F_D-S)/B + S$. (see text)

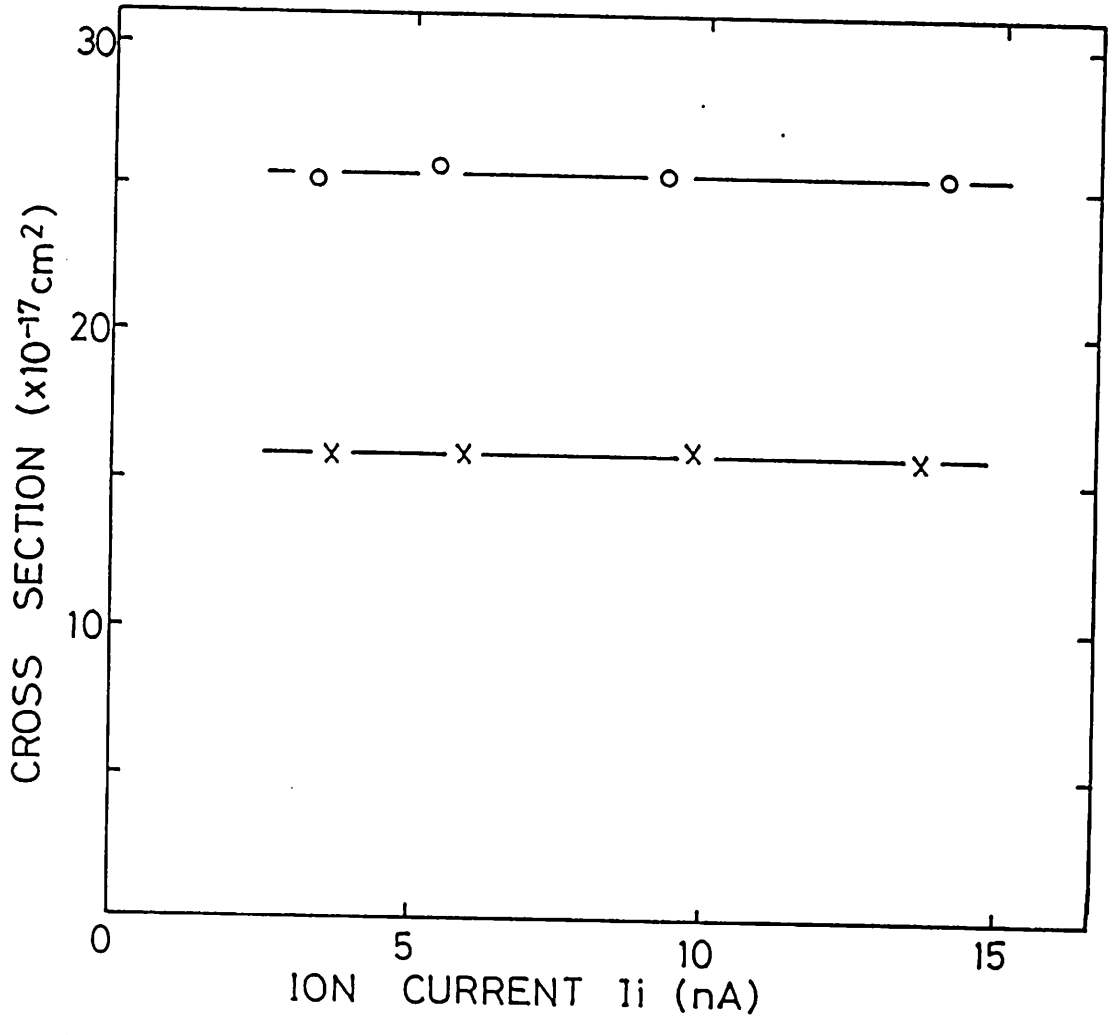

Fig.5-7. Cross section dependence on the ion current measured at the impact energies 50eV (open circles) and 200eV (crosses) in Sr^+ single ionization.

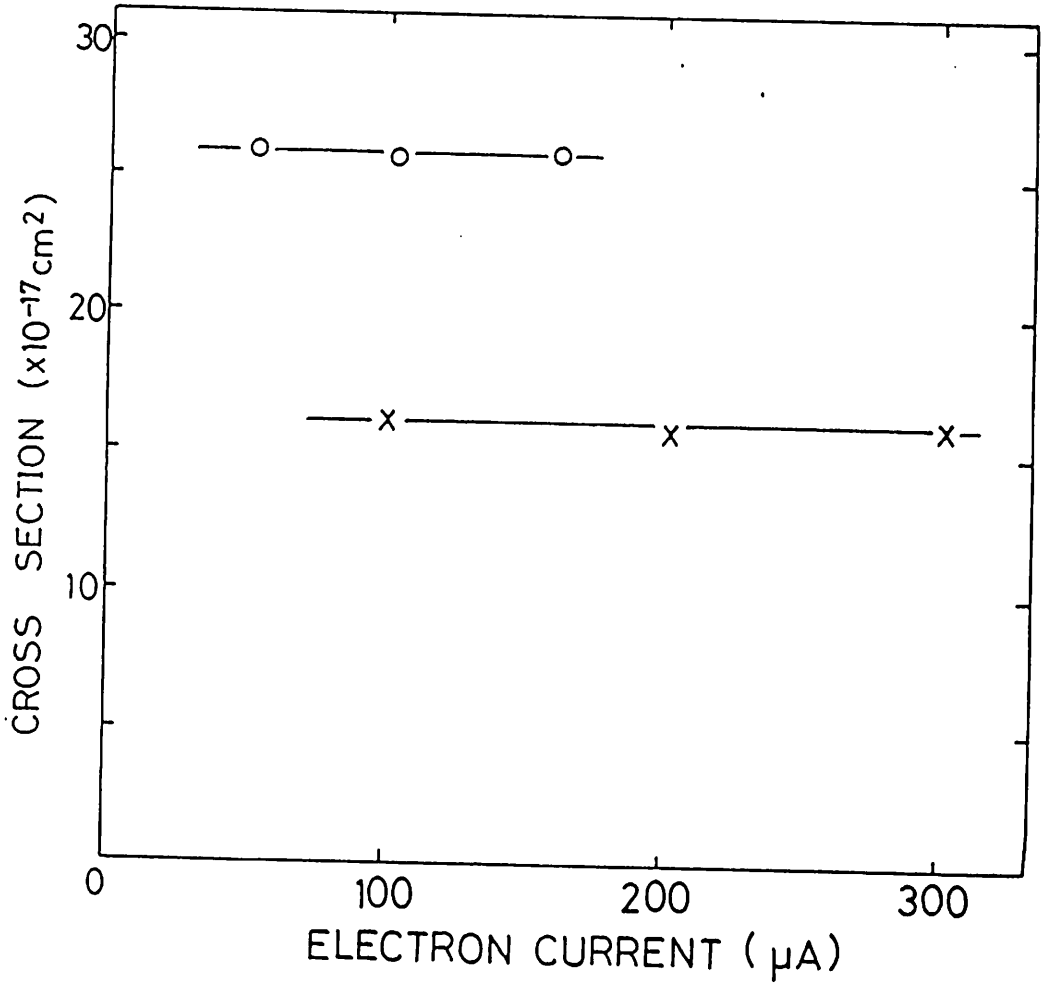

Fig.5-8. Cross section dependence on the electron current measured at the impact energies 50 eV (open circles) and 200 eV (crosses) in Sr^+ single ionization.

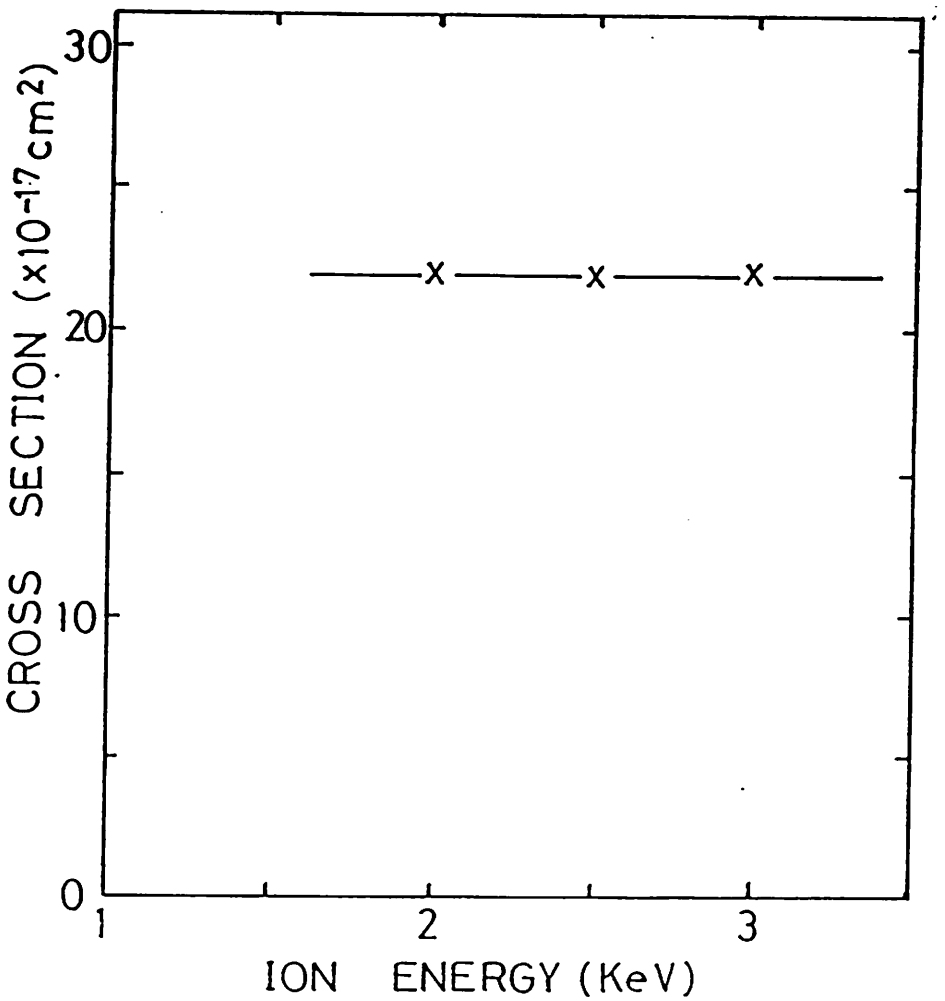

Fig.5-9. Cross section dependence on the ion energy measured at impact energy 100 eV in Sr^+ single ionization.

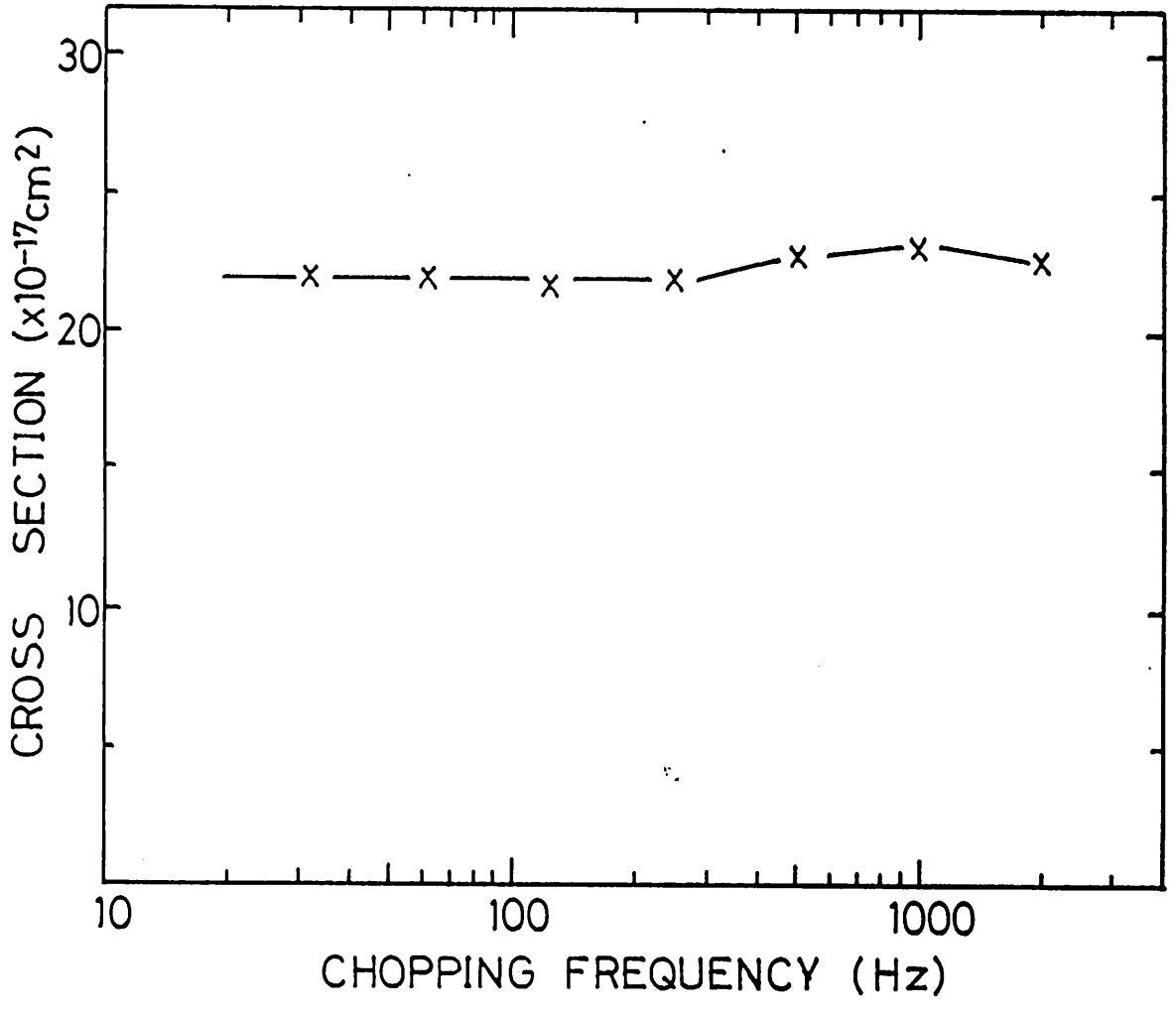

Fig.5-10. Cross section dependence on the chopping frequency measured at the impact energy 100 eV in Sr^+ single ionization.

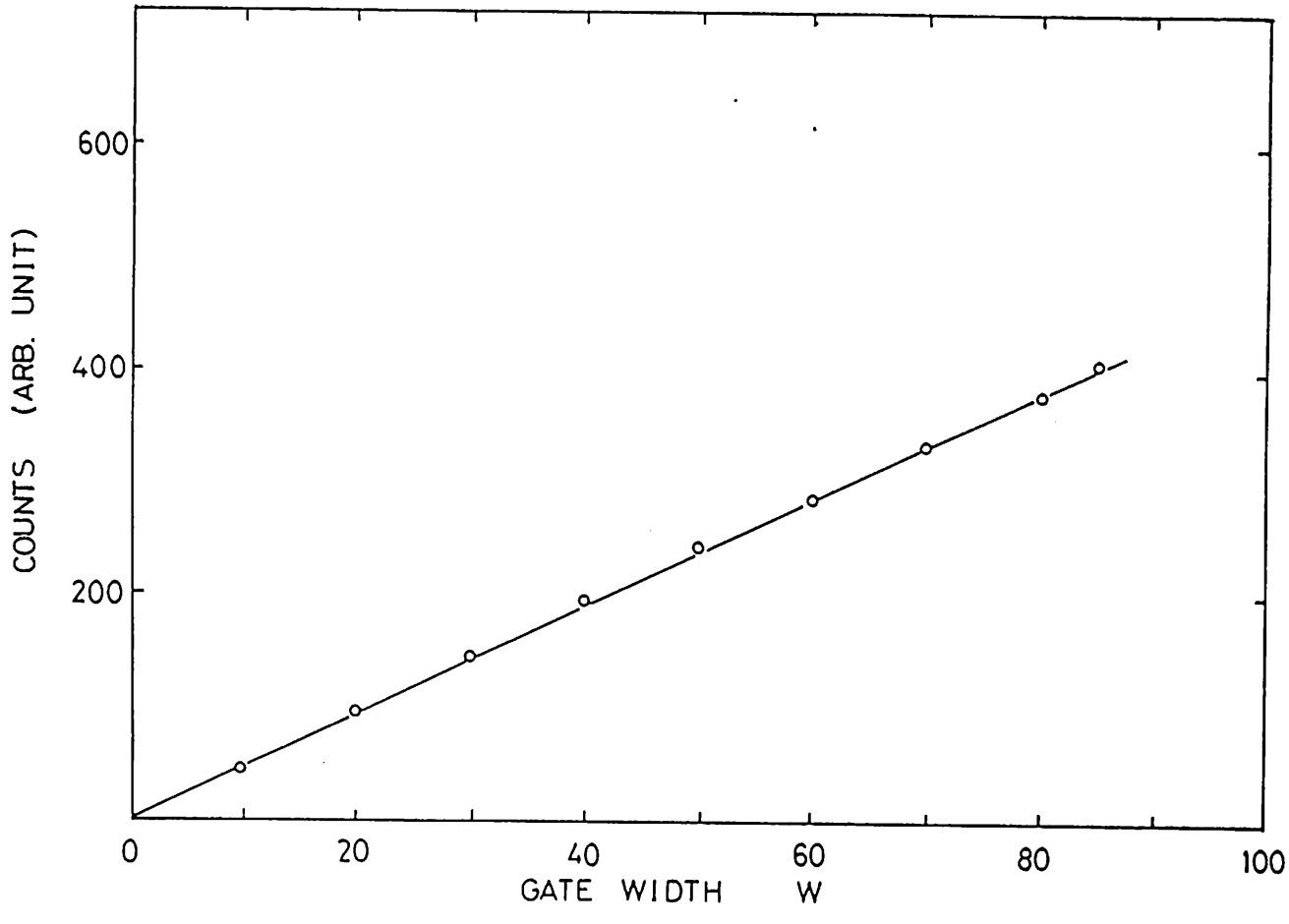

Fig.5-11. Relation between the width 'W' of the gate control pulse and the counts. W is varied by changing the end timing 'Re'. (See text)

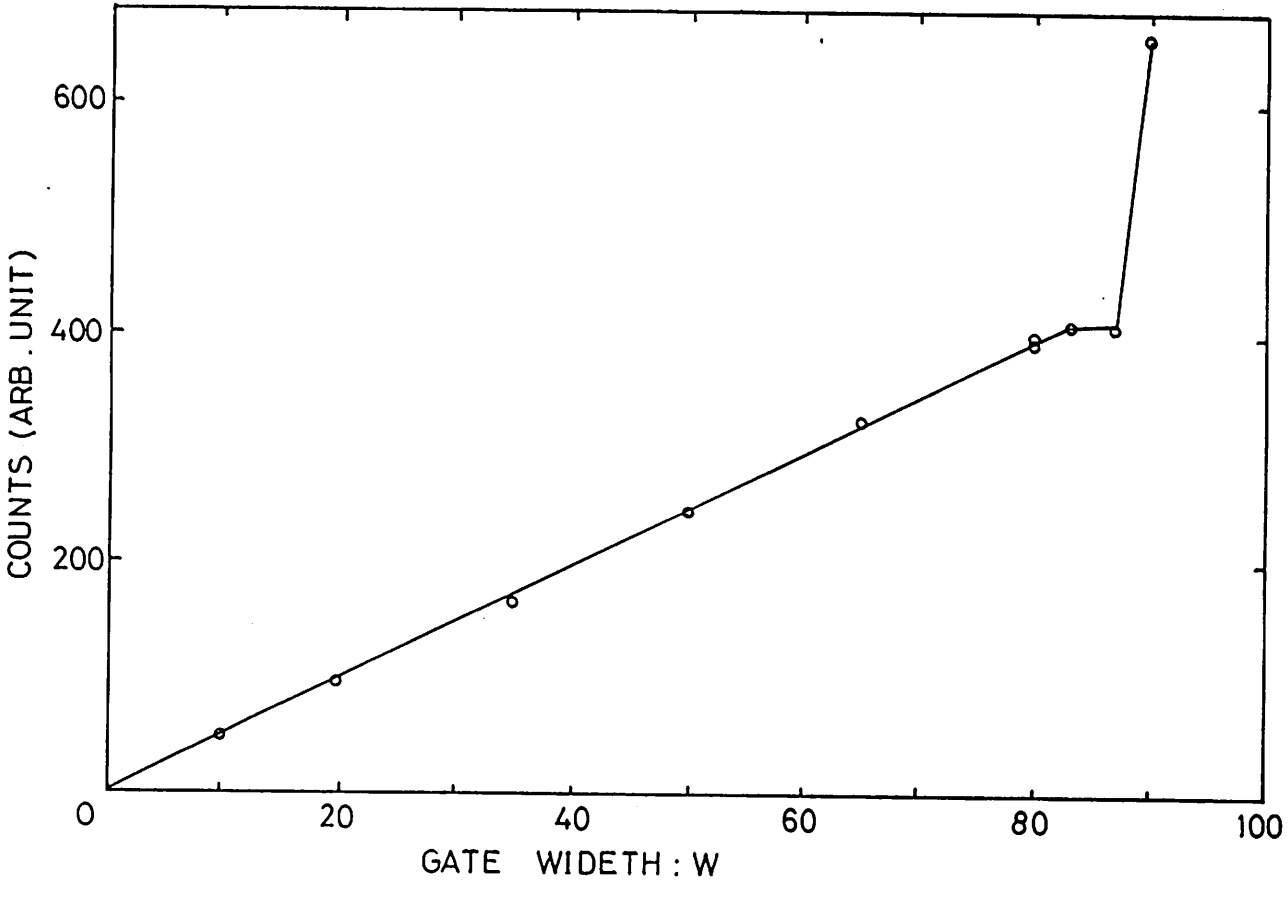

Fig.5-12. Relation between the width 'W' of the gate control pulse and the counts. W is varied by changing the start timing 'At'. (See text)

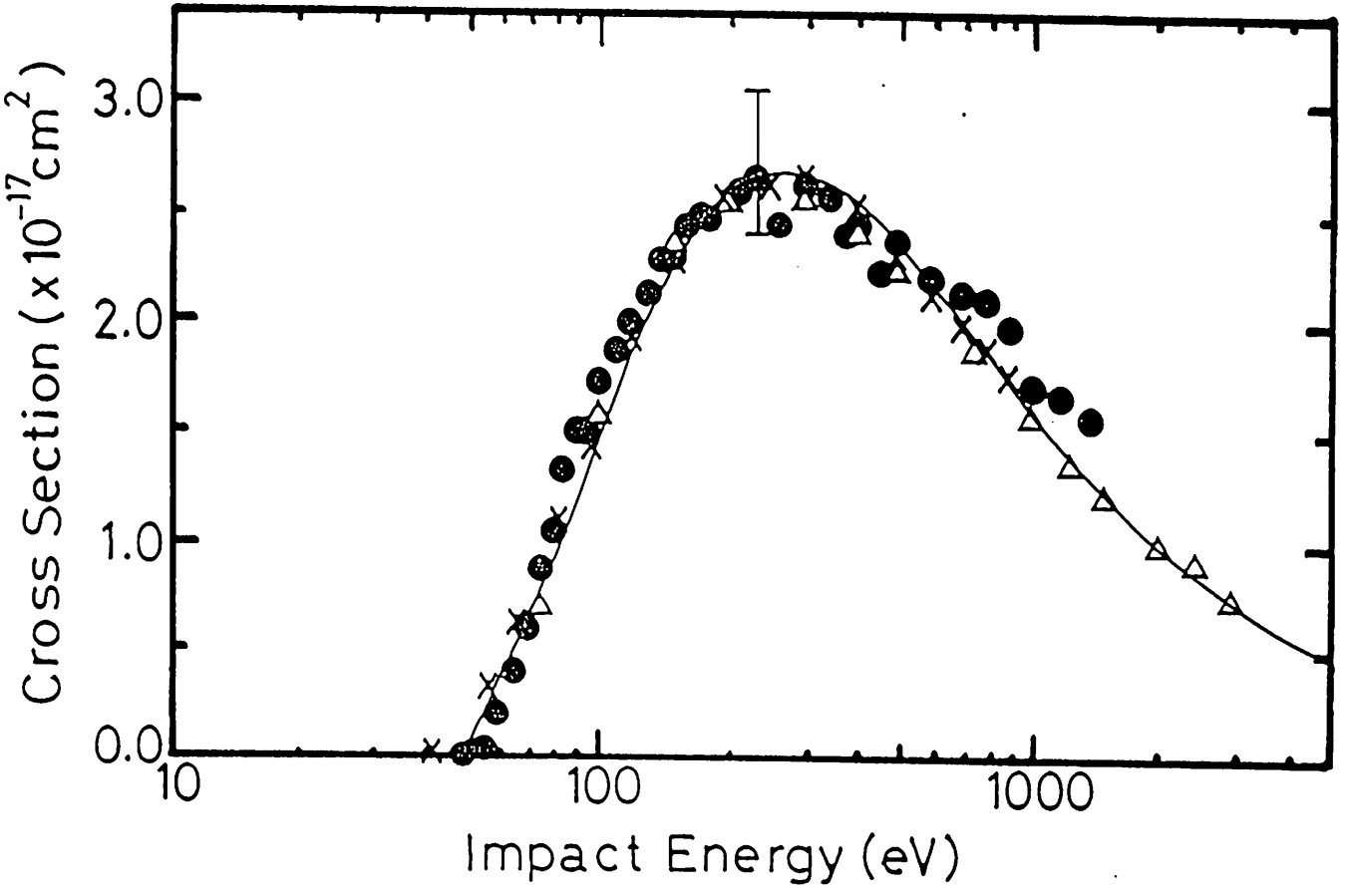

Fig.6-1. Single ionization cross section for Na^+. Closed circles -- present results, crosses -- Hooper et al.[75], triangles -- Peart and Dolder,[76] solid line -- Lotz calculation.[63]

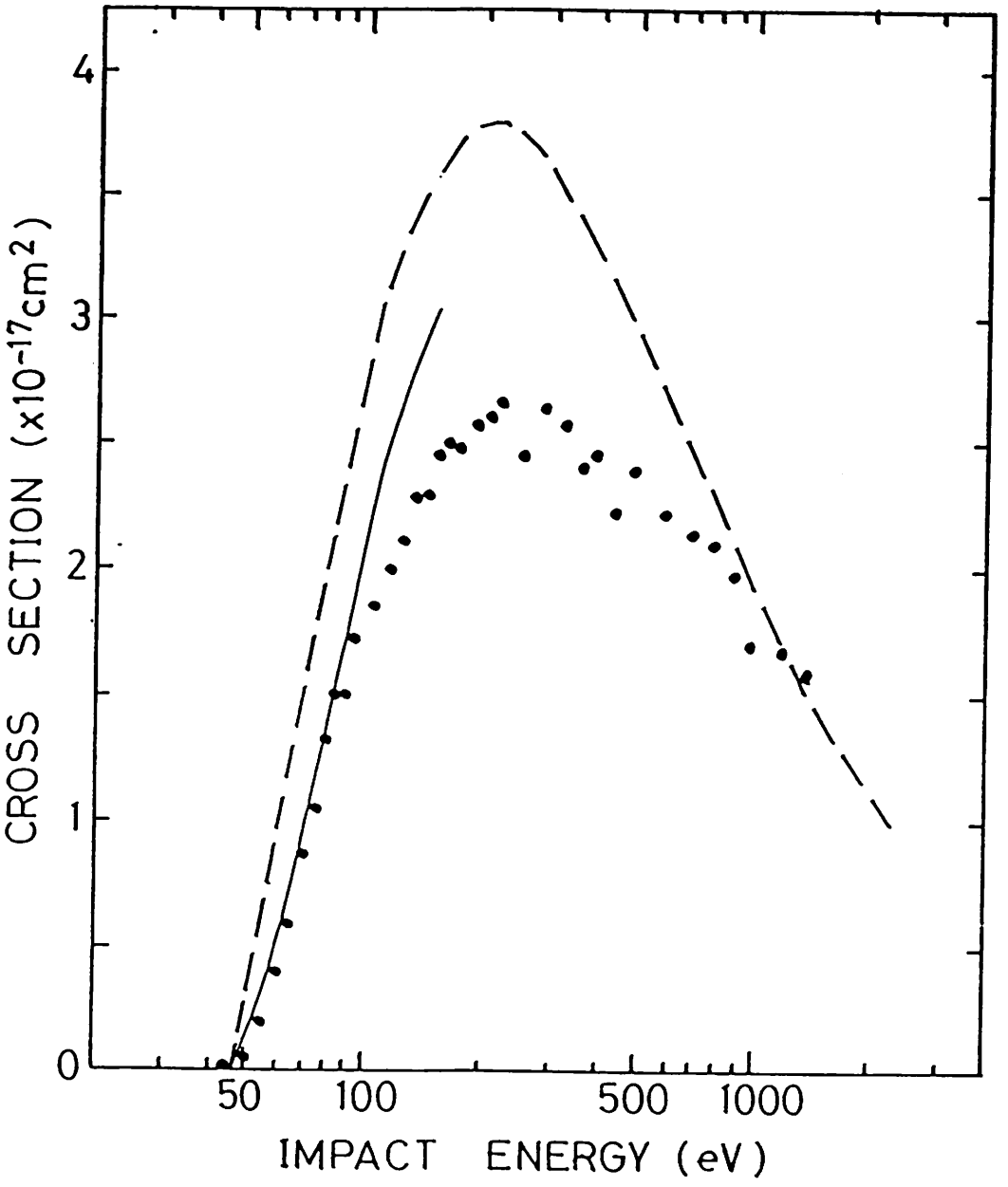

Fig.6-2. Comparison of the theoretical and experimental cross sections for Na^+ single ionization. Solid line -- distorted wave calculation by Younger[76], dashed line -- Coulomb-Born calculation by Moores,[77] closed circles -- present experiments.

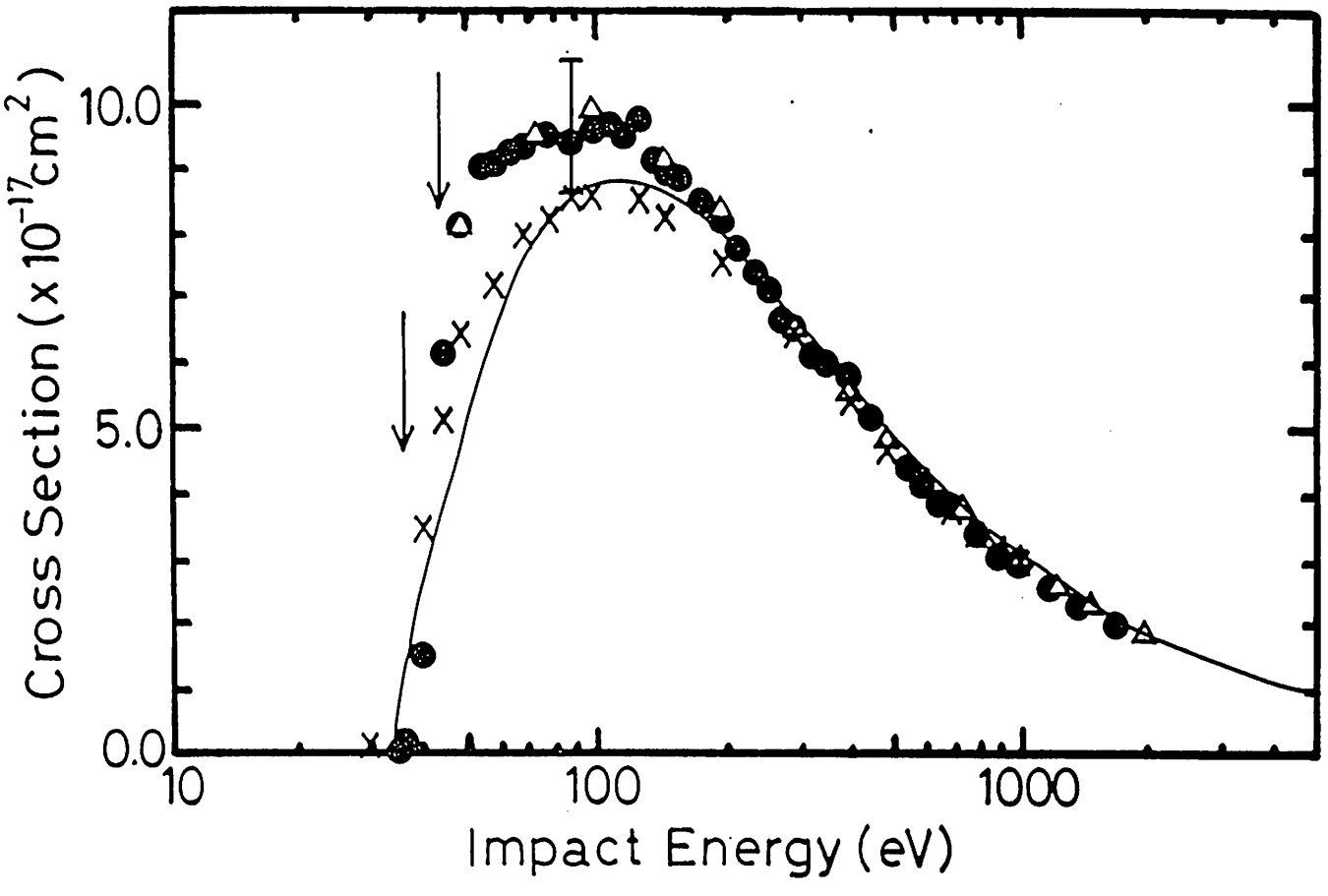

Fig.6-3. Single ionization cross sections for K^+. Symbols are the same as in Fig.6-1. Arrows show the thresholds of core excited and double excited autoionizing states. (See text)

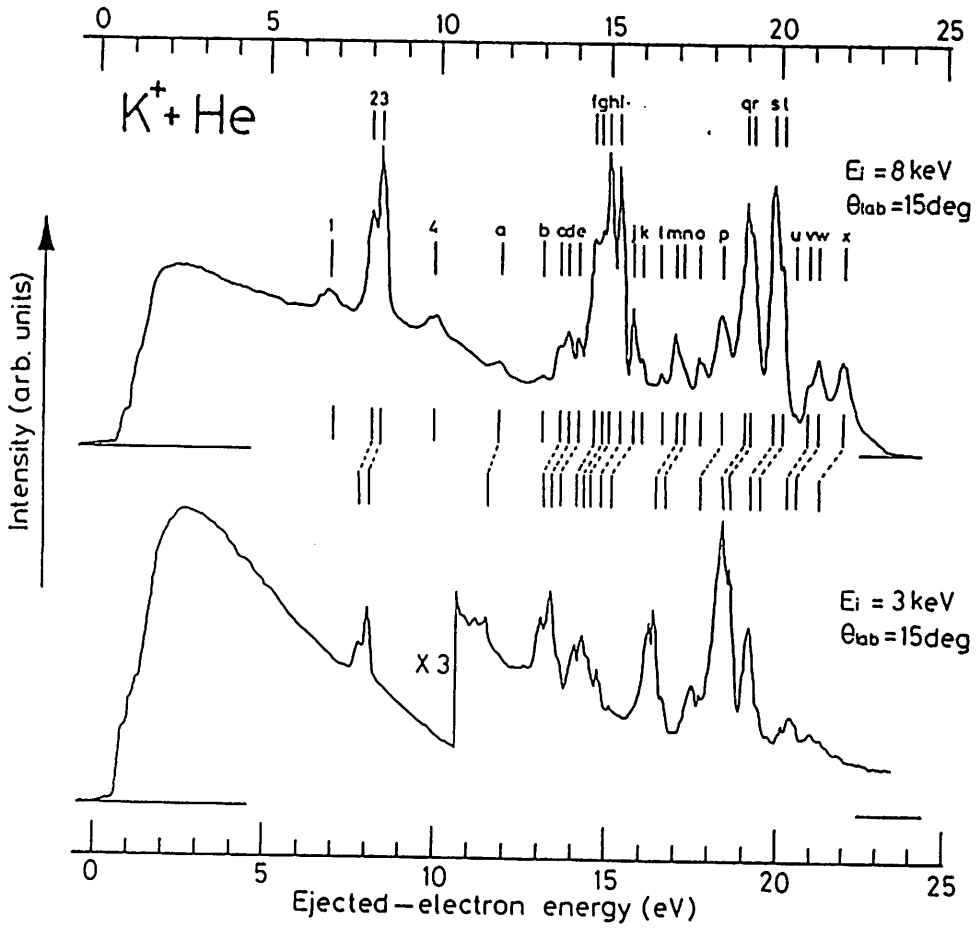

Fig.6-4. Ejected electron spectra from the autoionizing states in K^+ and K resulting from the low energy K^+ - He collisions from ref.78). Peaks 1 to 6, and a to j correspond to the core excited and doubly excited autoionizing states in K^+, and peaks k to v correspond to those in K atom. (See text)

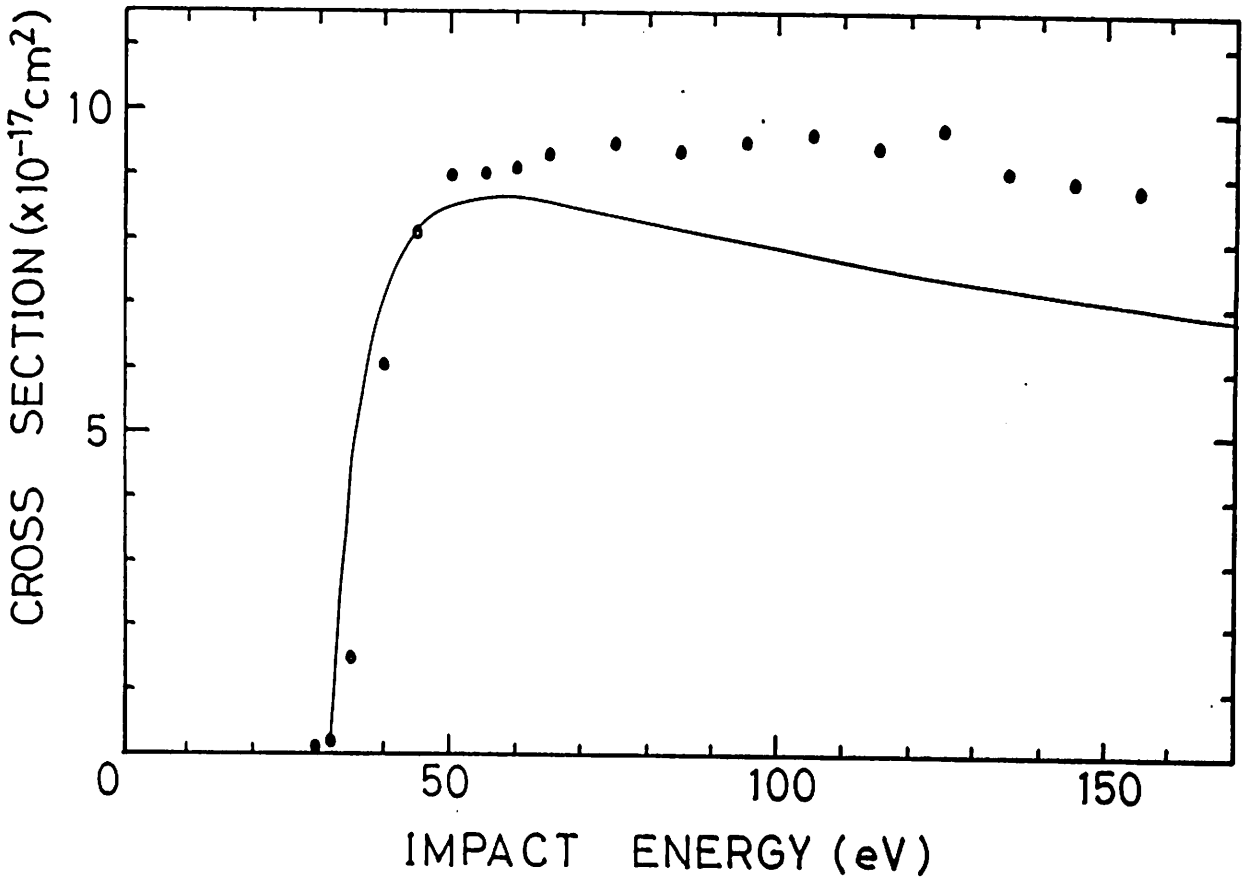

Fig.6-5. Comparison of the theoretical and experimental cross sections for K^+ single ionization. Solid line -- distorted wave calculation by Younger,[79] closed circles -- present experiments.

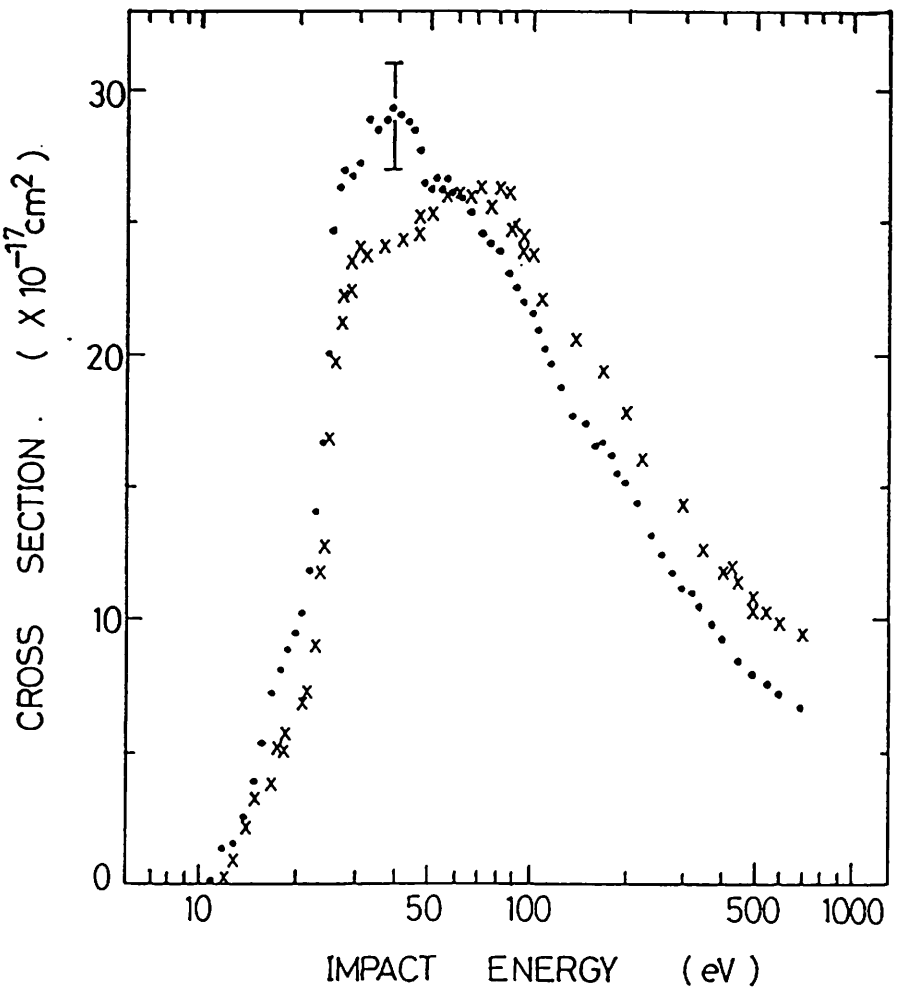

Fig.6-6. Single ionization cross sections for Sr^+. Closed circles -- present results, crosses -- Peart and Dolder.[80)]

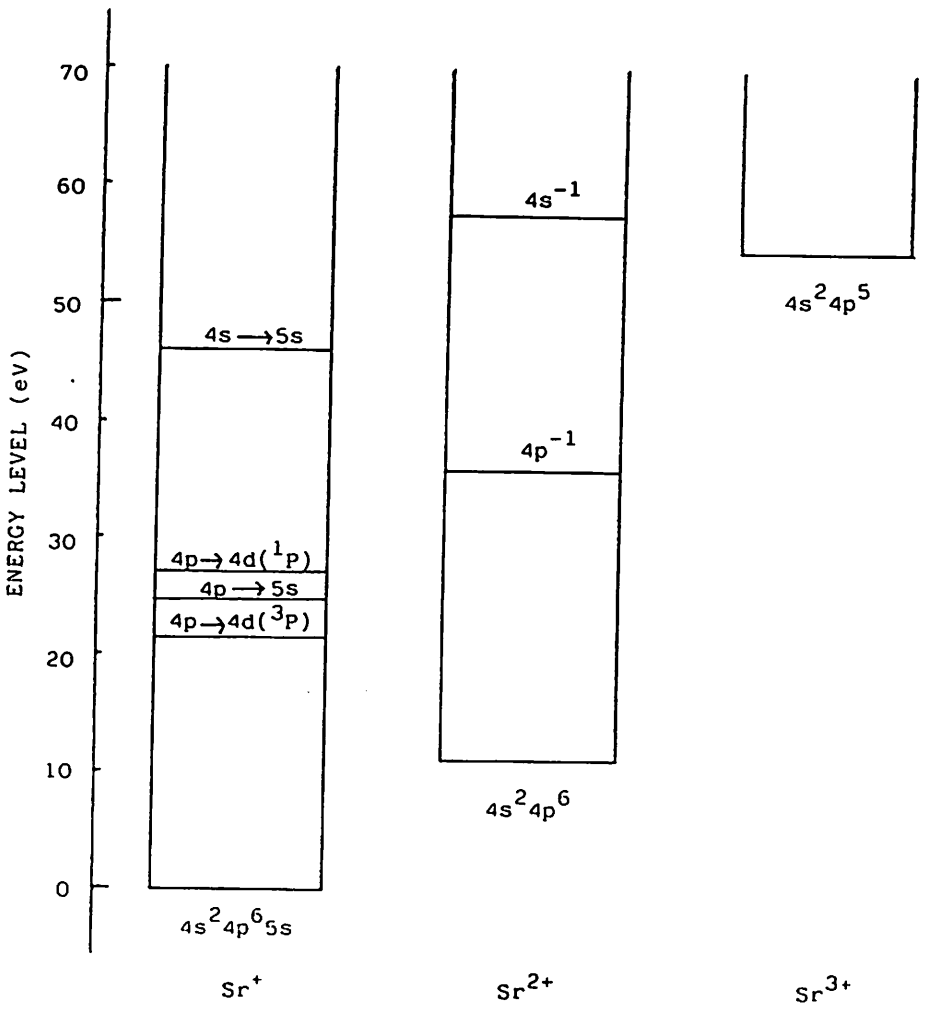

Fig.6-7. Autoionizing levels in Sr^{+}.

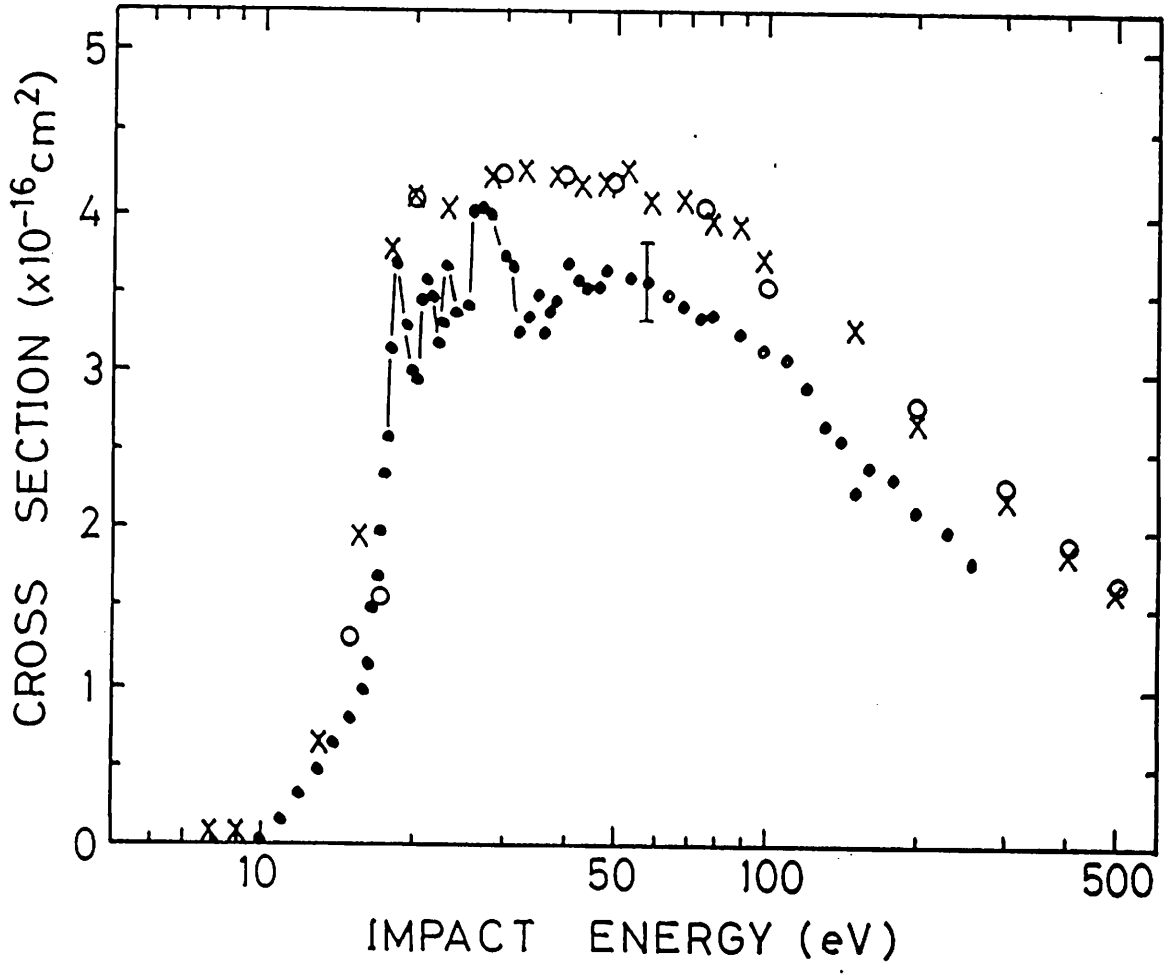

Fig.6-8. Single ionization cross sections in Ba^+. Solid points -- present results, crosses -- Feeney et al.[84], open circles -- Peart and Dolder.[83]

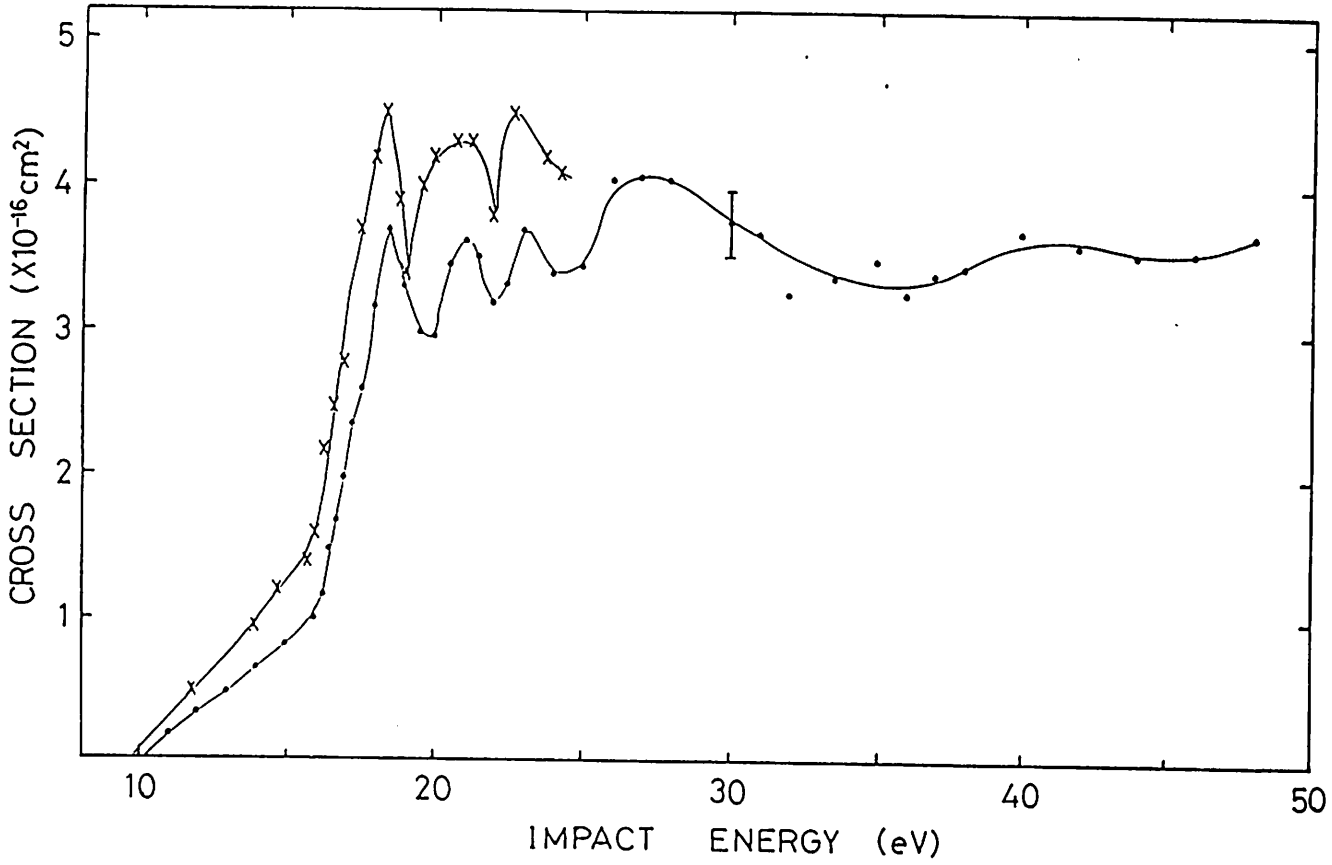

Fig.6-9. Ba^+ single ionization cross sections near the threshold region. Solid points -- present results, crosses -- Peart et al.[85)]

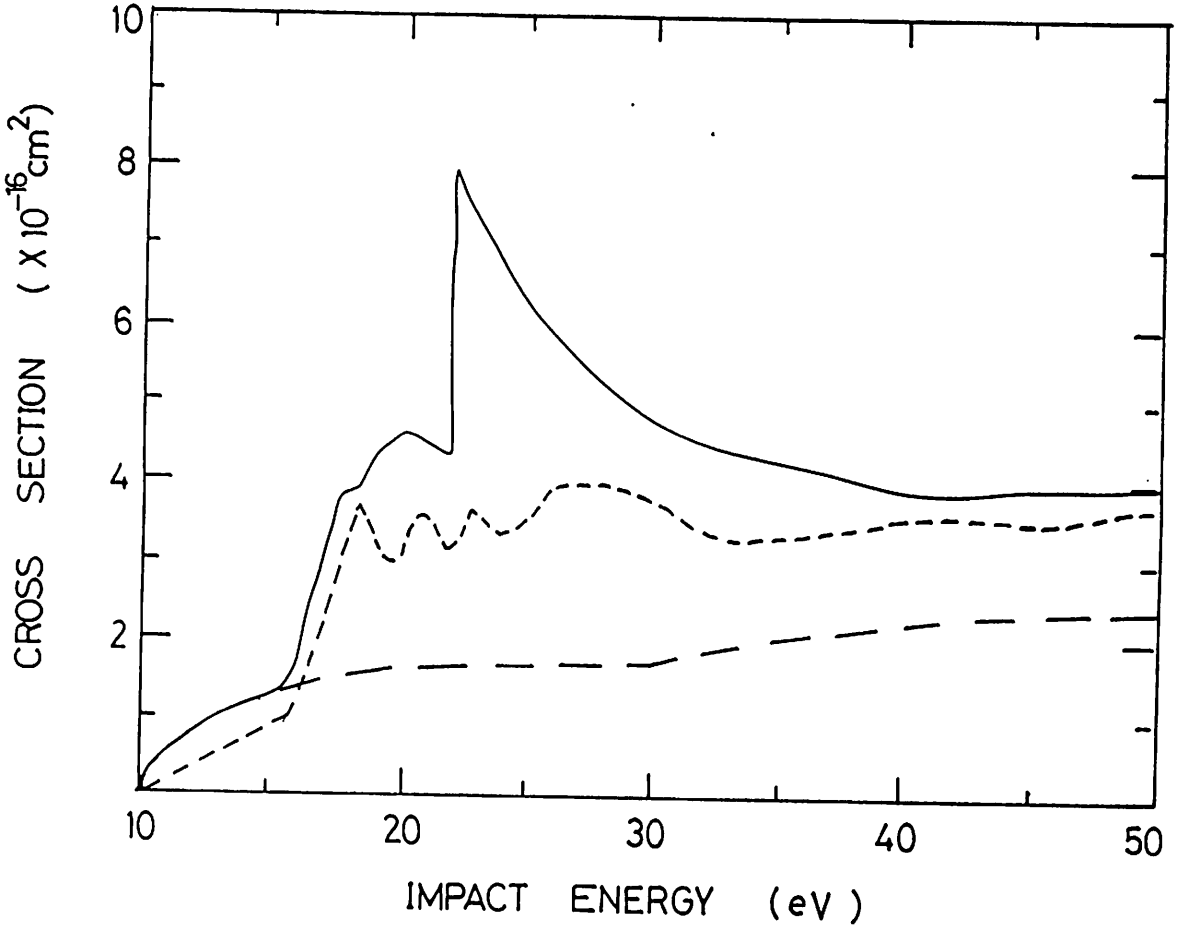

Fig.6-10. Comparison of the theoretical and experimental cross sections for the Ba^+ single ionization. Long dashed curve -- direct ionization cross section calculated from the Lotz formula, solid line -- distorted wave results[86] added to the Lotz values.

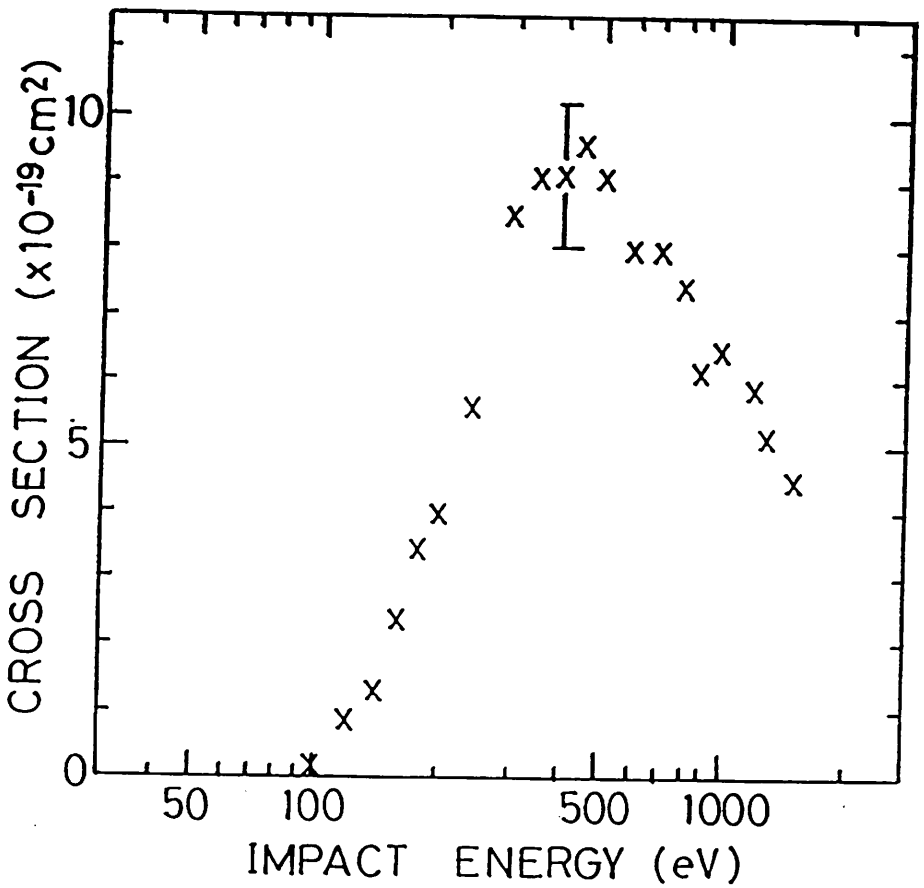

Fig.7-1. Double ionization cross sections for Na^+.

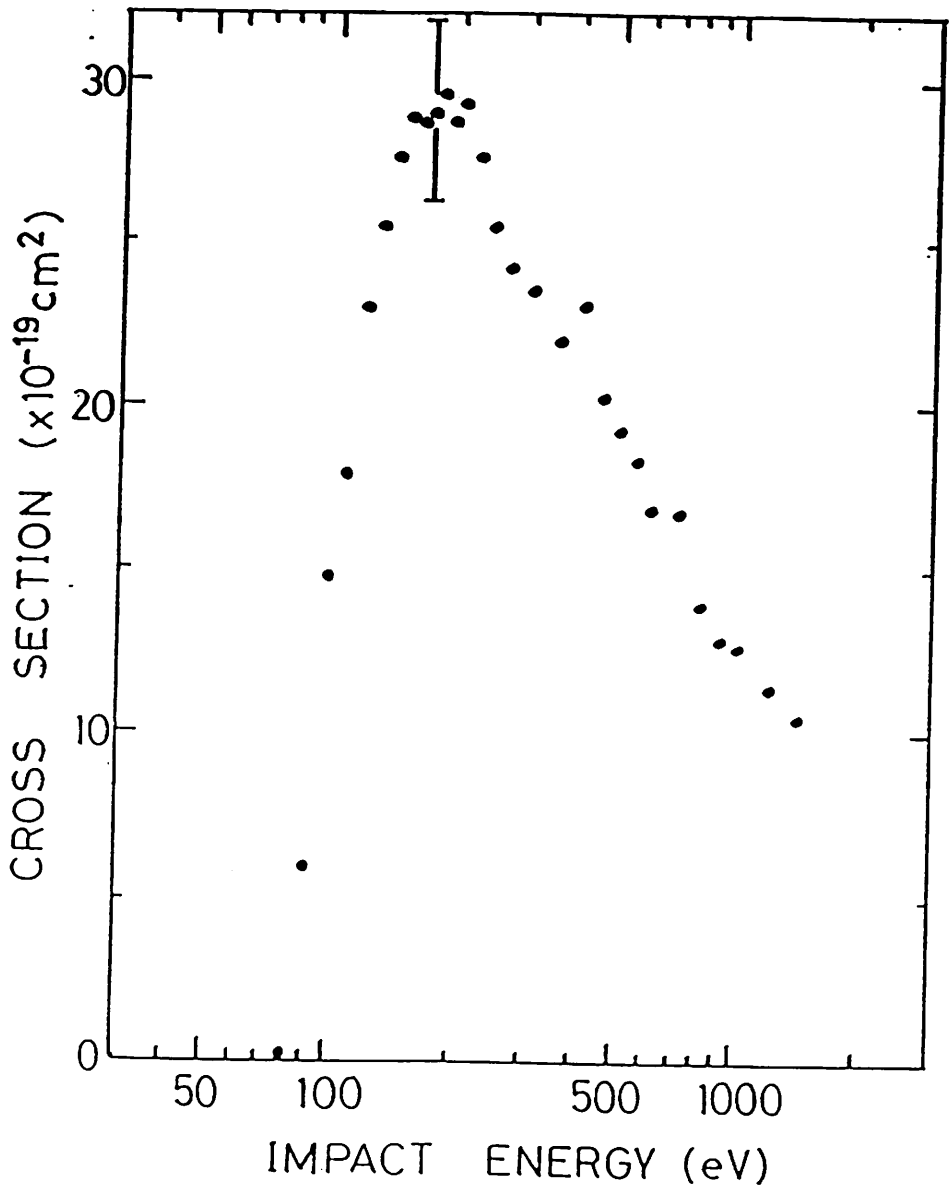

Fig.7-2. Double ionization cross sections for K^+.

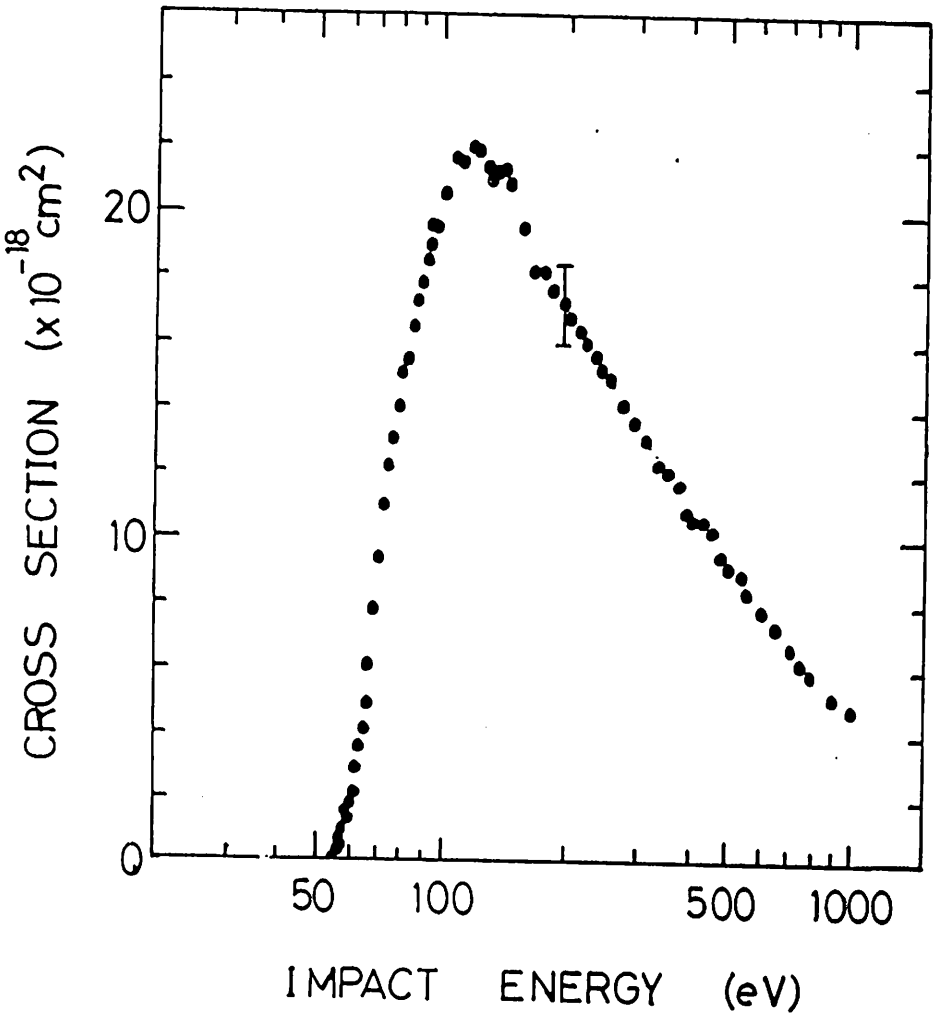

Fig.7-3. Double ionization cross sections for Sr^+.

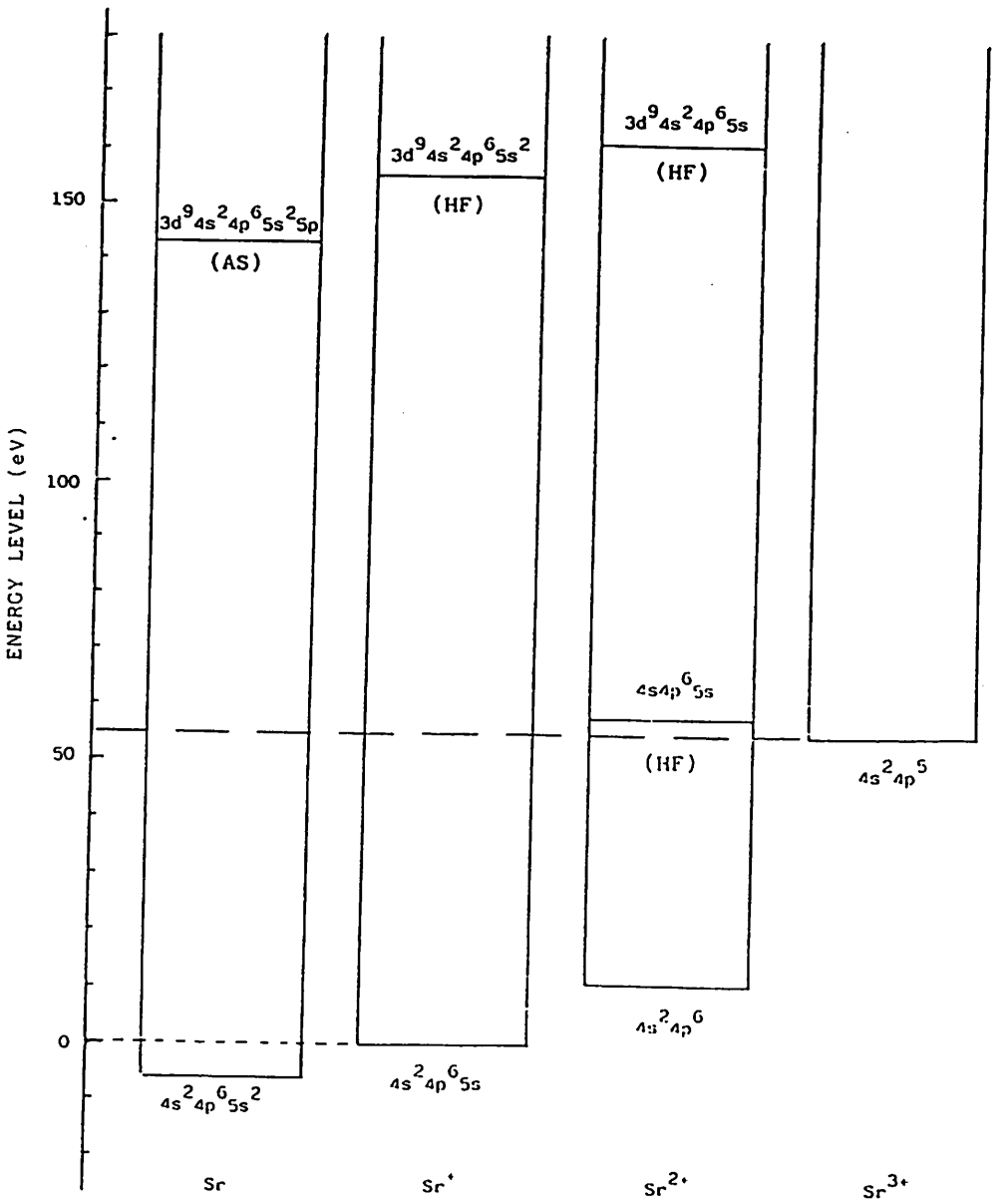

Fig.7-4. Energy diagram of Sr^+. Levels are adopted from the Auger electron spectroscopy (labeled 'AS') and the Hartree-Fock calculation (labeled 'HF').

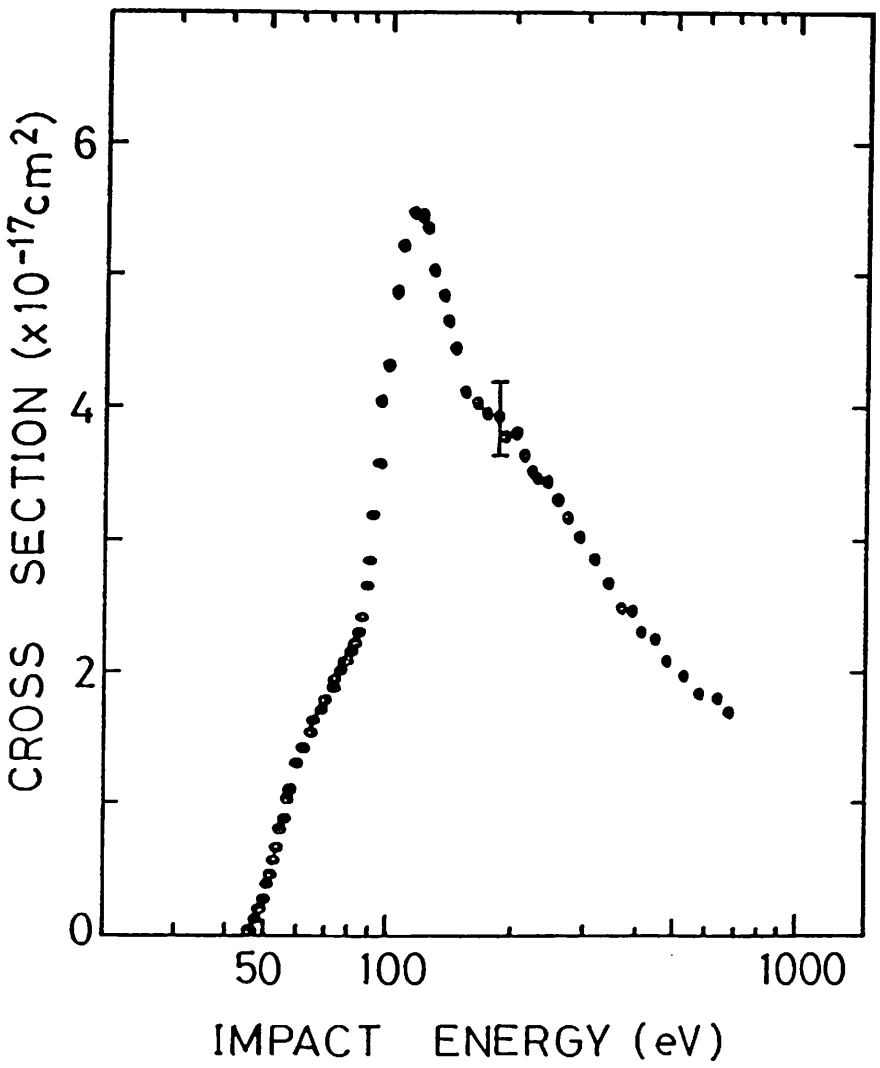

Fig.7-5. Double ionization cross sections for Ba^{+}.

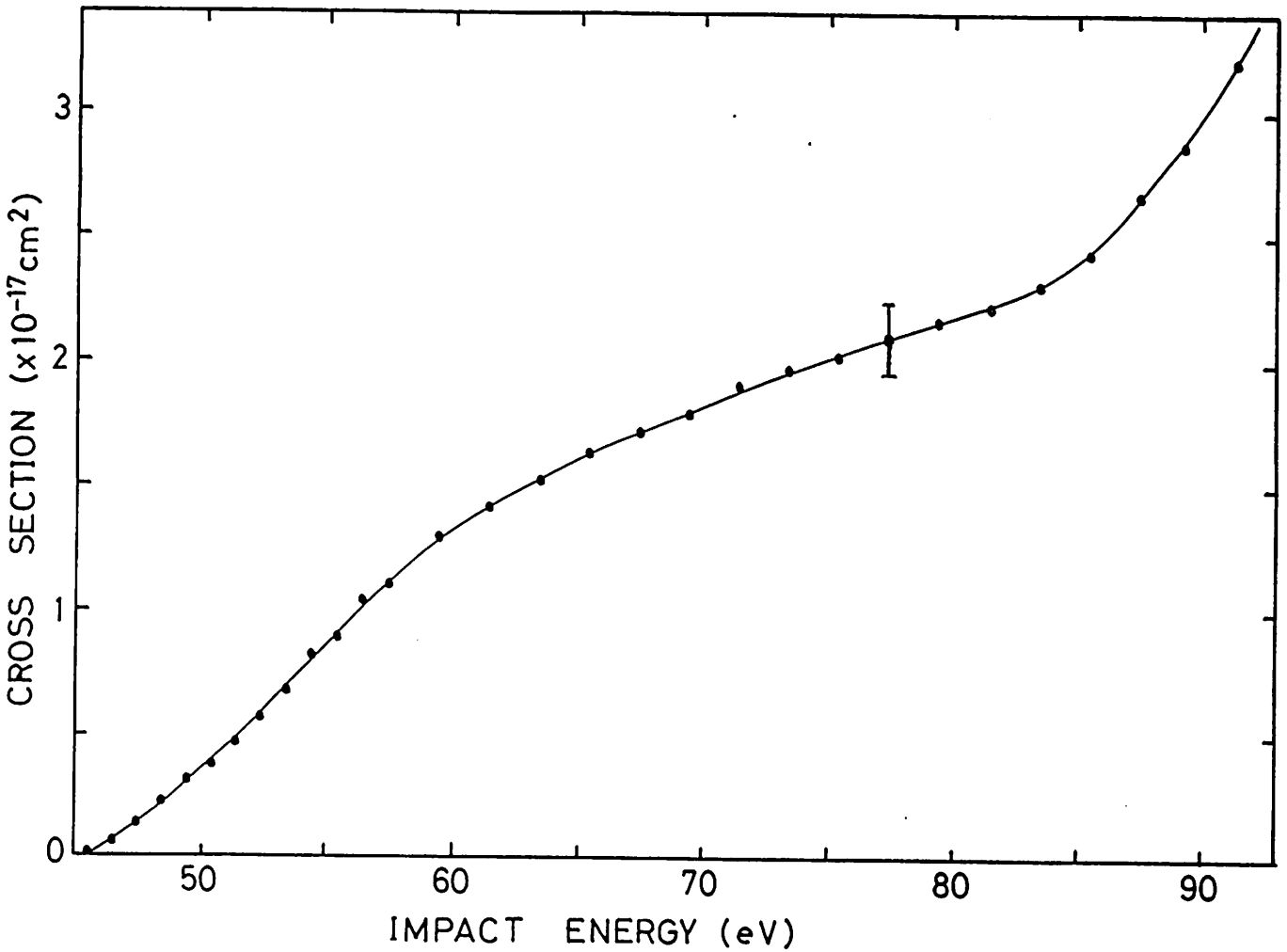

Fig.7-6. Ba^+ double ionization cross sections near the threshold region.

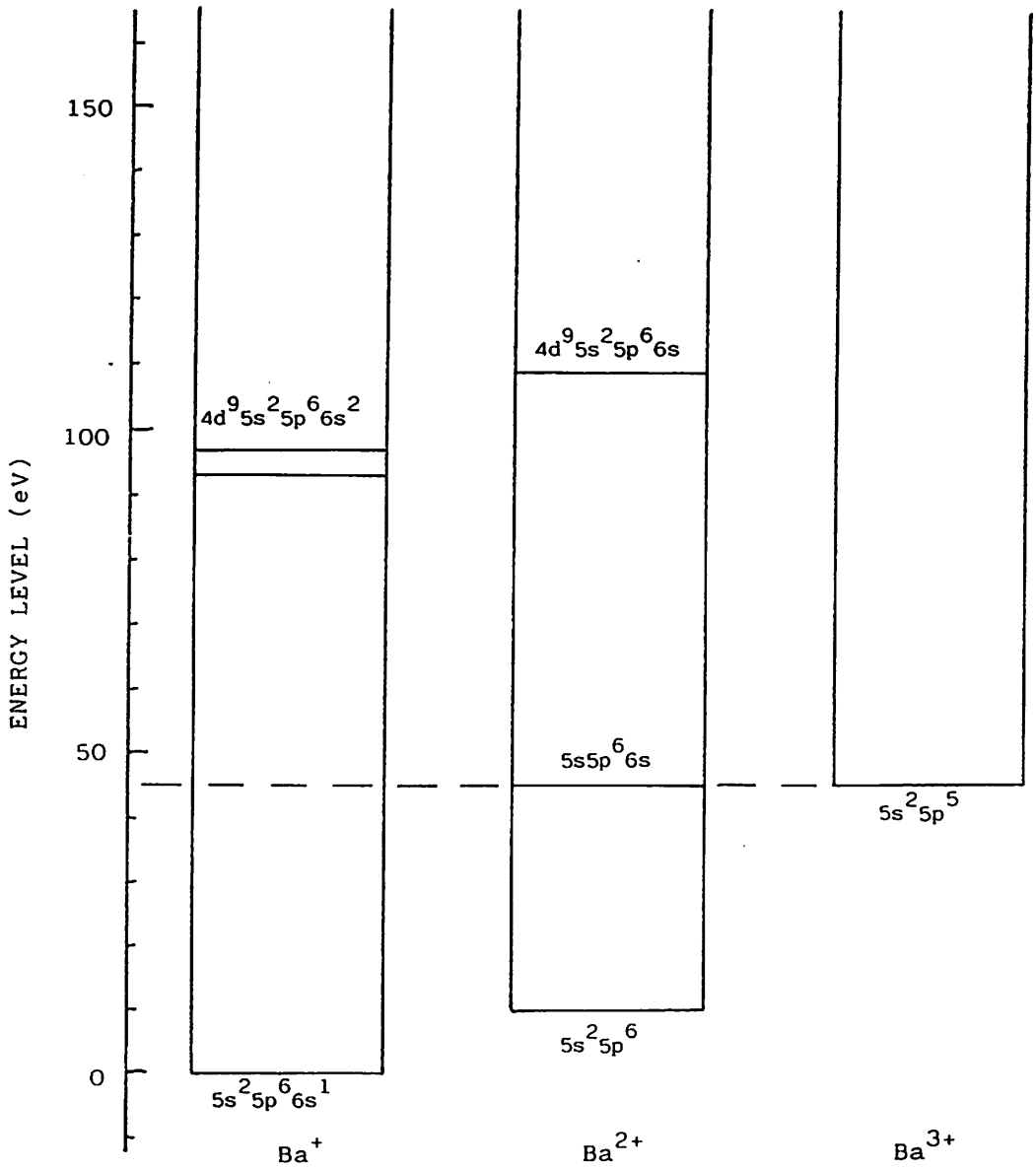

Fig.7-7. Energy diagram of Ba^+.

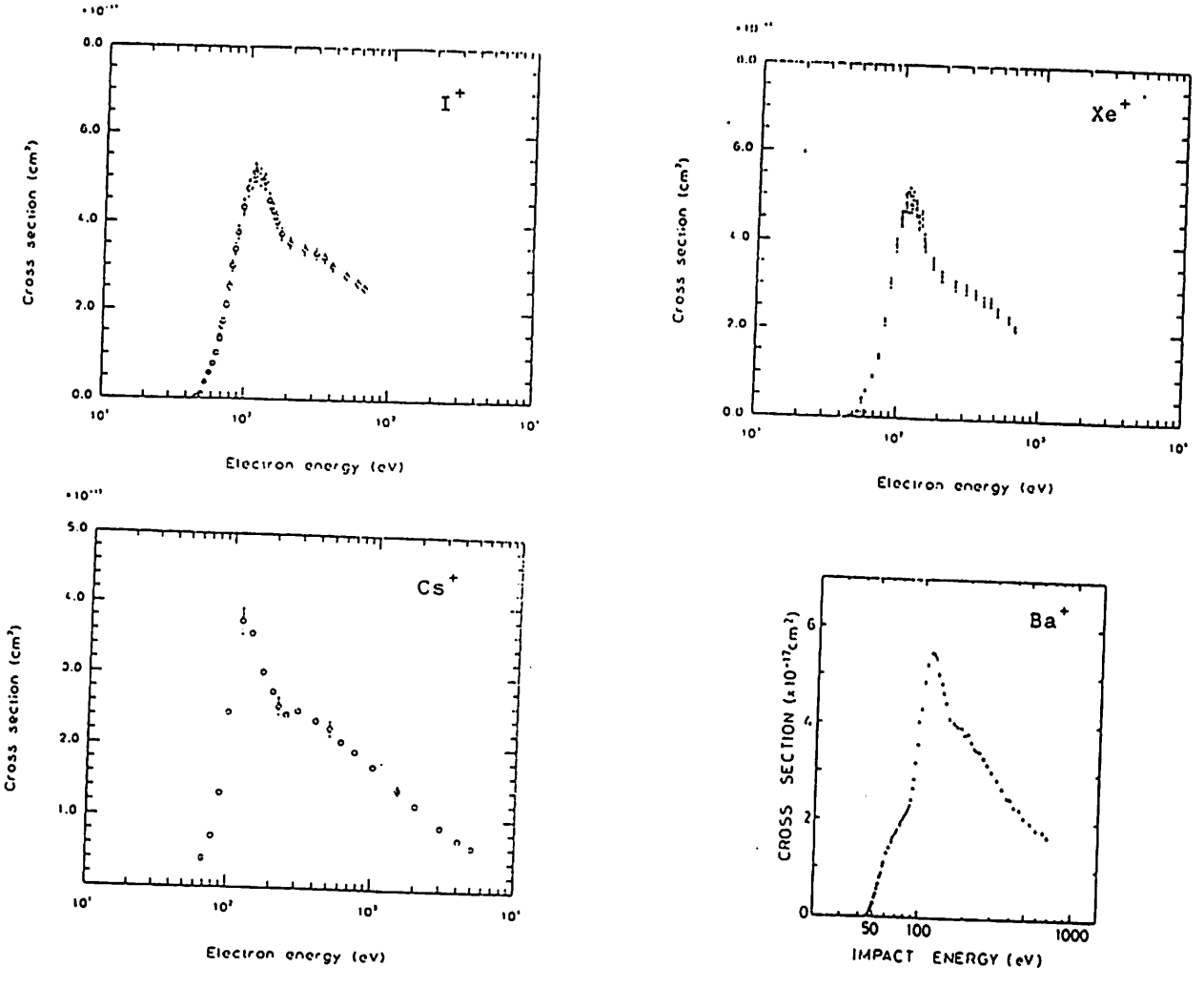

Fig.7-8. Double ionization cross sections for I^+ 92), Xe^+ 92), Cs^+ 93) and Ba^+.

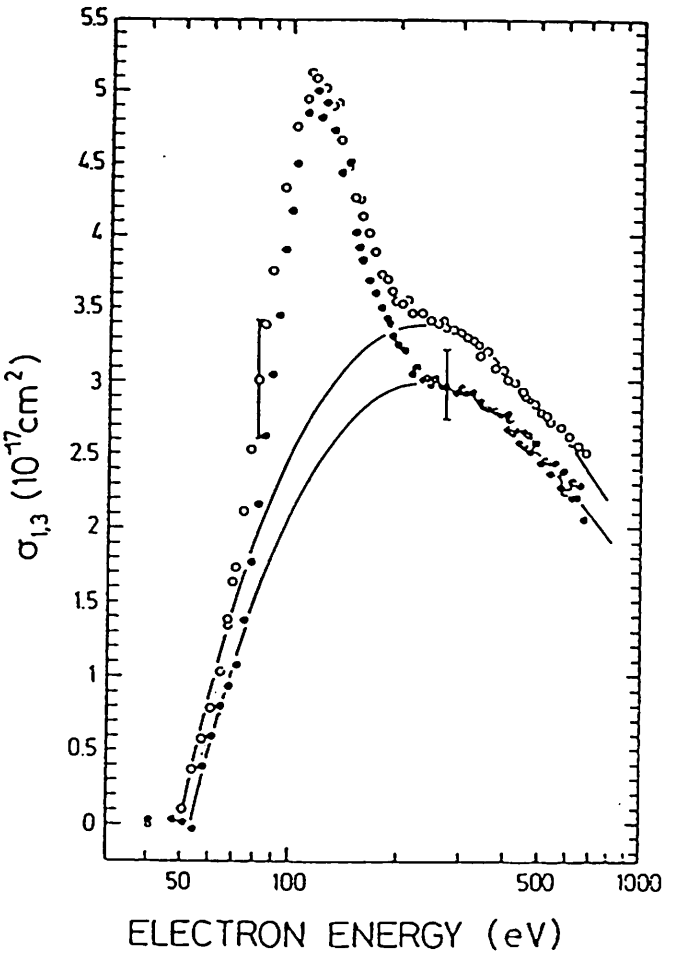

Fig.7-9. Estimation for 4d-ionization cross section in I^+ (open circles) and Xe^+ (closed circles) by Achenbach et al.[92] Solid curve represents the direct double ionization contribution obtained by a fitting procedure. (See text)

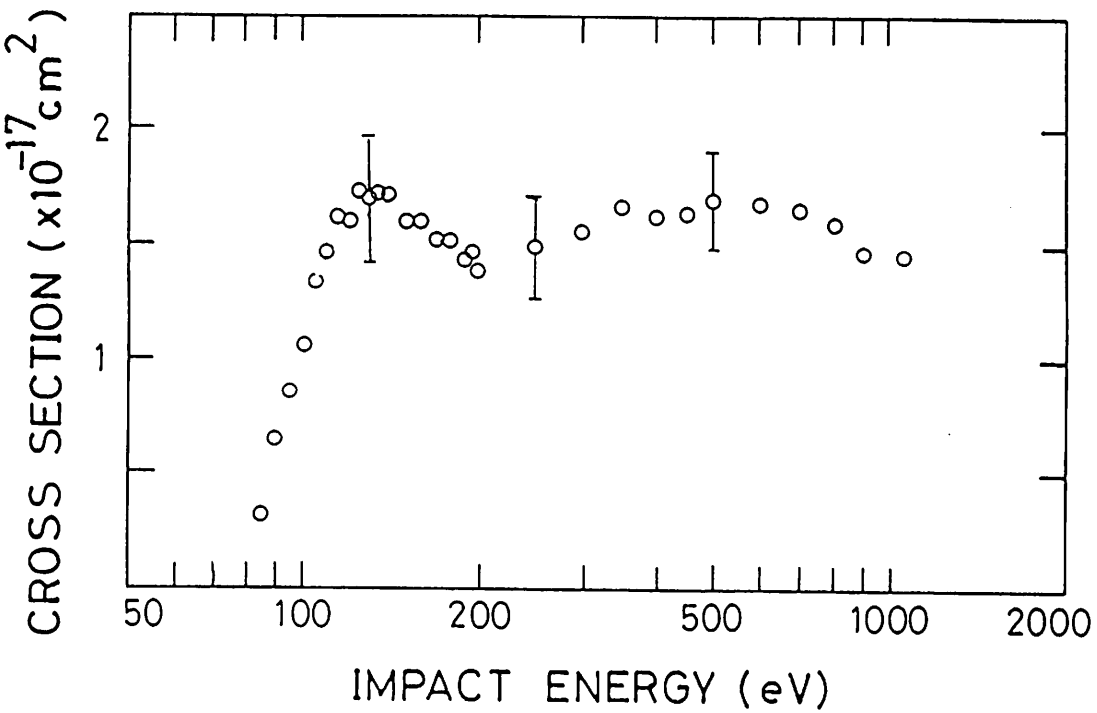

Fig.7-10. 4d-ionization cross sections in Xe atom measured by Takayanagi et al.[94),95)].

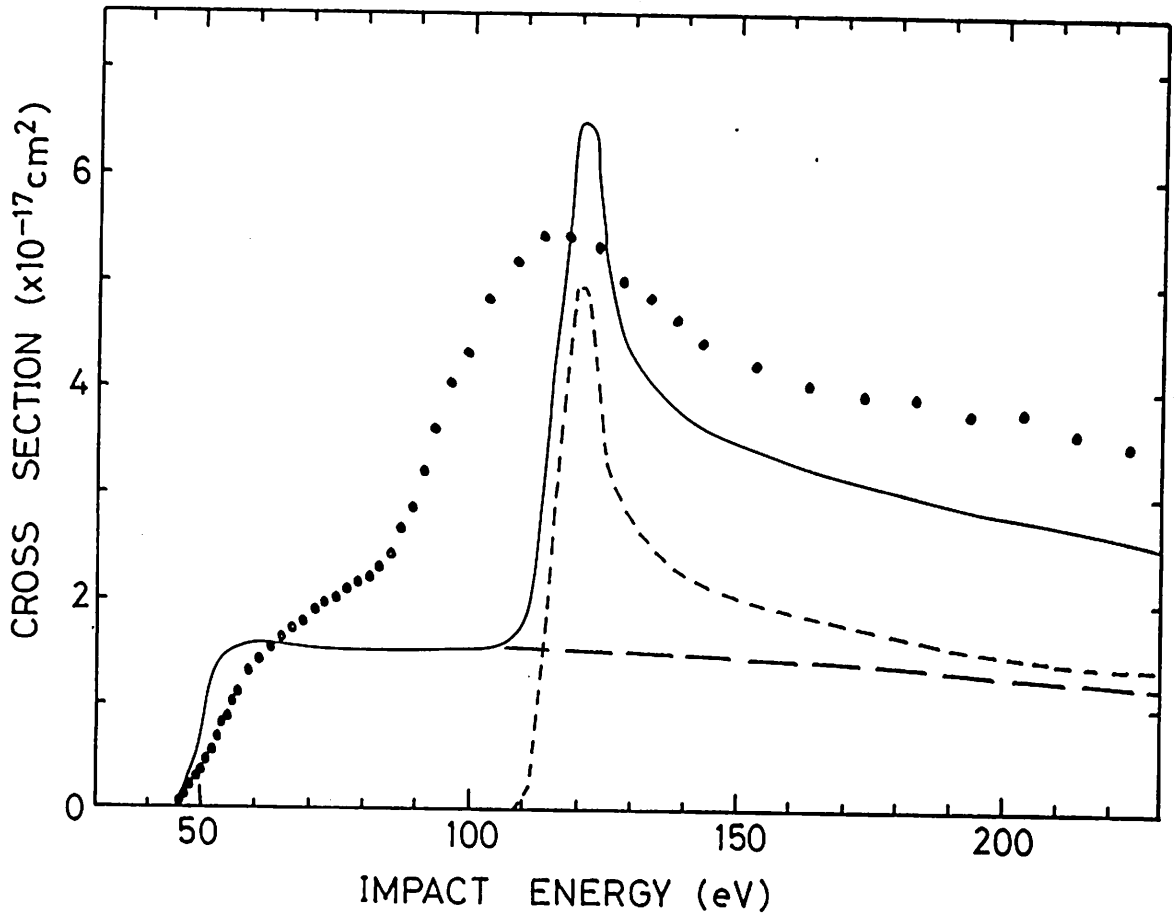

Fig.7-11. Comparison of the experimental results with the distorted wave calculation by Younger.[90] Solid points -- present experiments, long dashed line -- calculated 5s-direct ionization cross section, short dashed line -- calculated 4d-direct ionization cross section, solid line -- sum of the 5s and 4d ionization cross section, i.e. contribution from the inner-shell direct ionization to the double ionization cross sections. (See text)

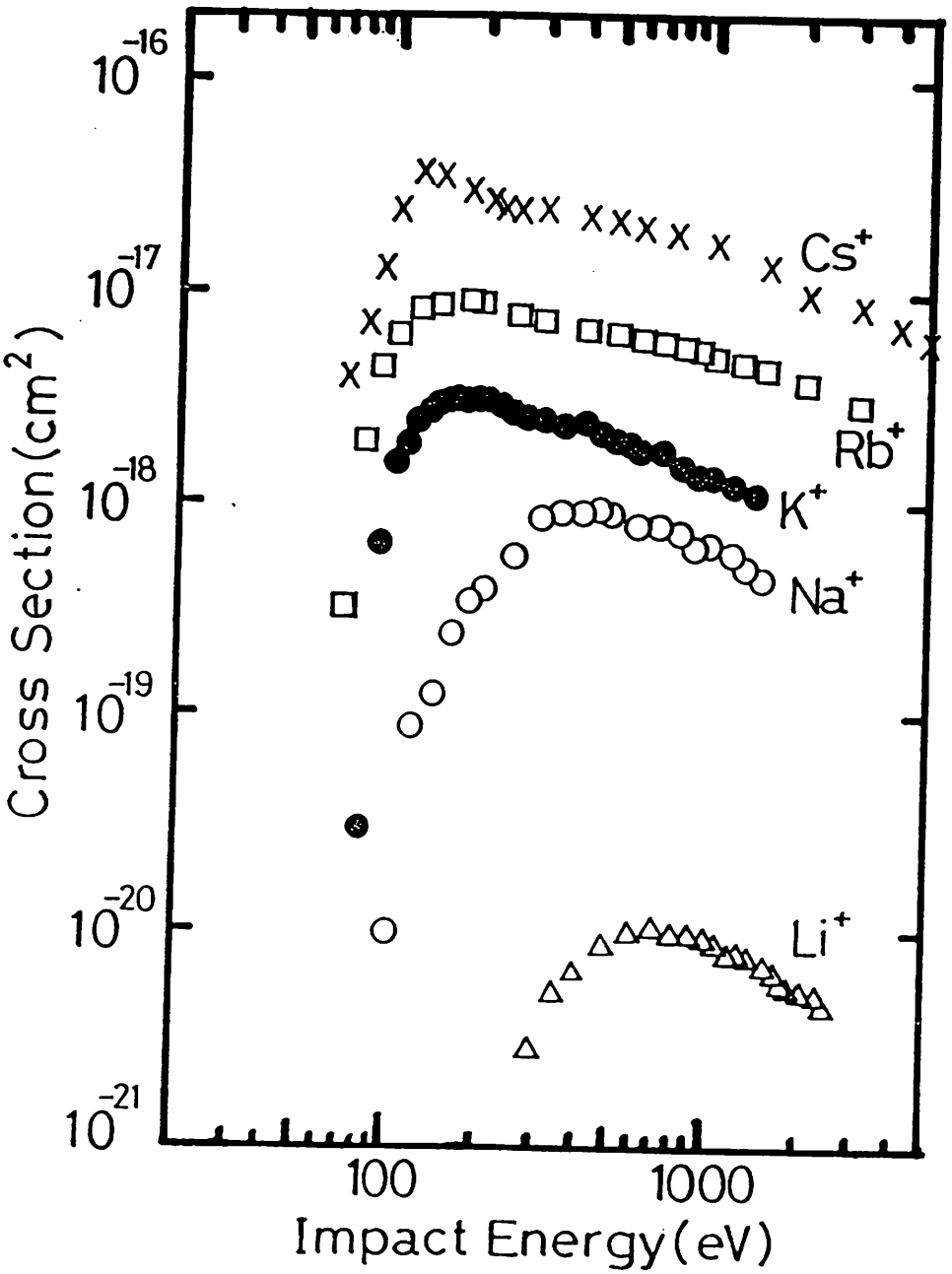

Fig.8-1. Double ionization cross sections for alkali ions. Na^+ and K^+ -- present, Li^+ -- Peart and Dolder[100], Rb^+ -- Hughes and Feeney[101], Cs^+ -- Hertling et al.[93]

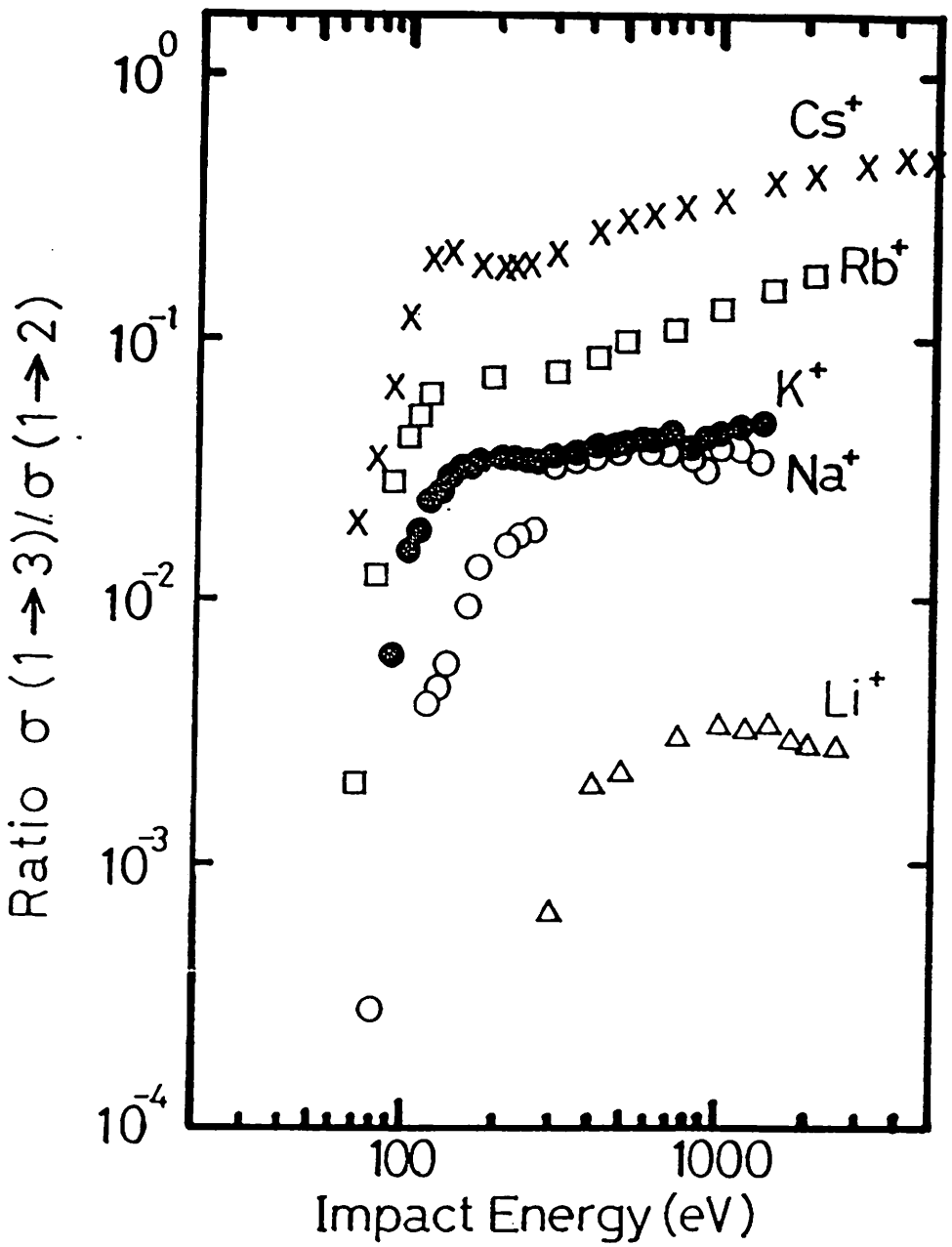

Fig.8-2. Ratios of single to double ionization cross sections for alkali ions.

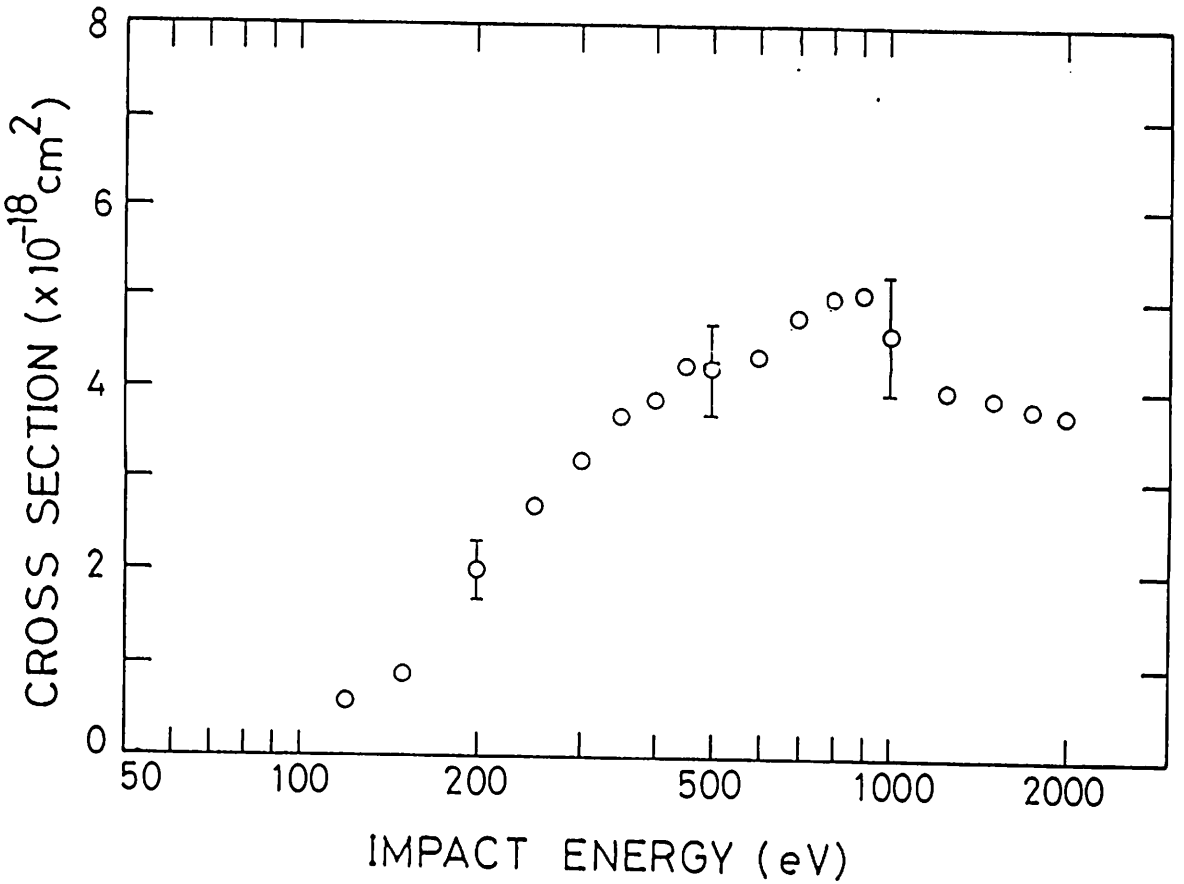

Fig.8-3. 3d-ionization cross sections in Kr atom measured by Takayanagi et al.[94),95)]

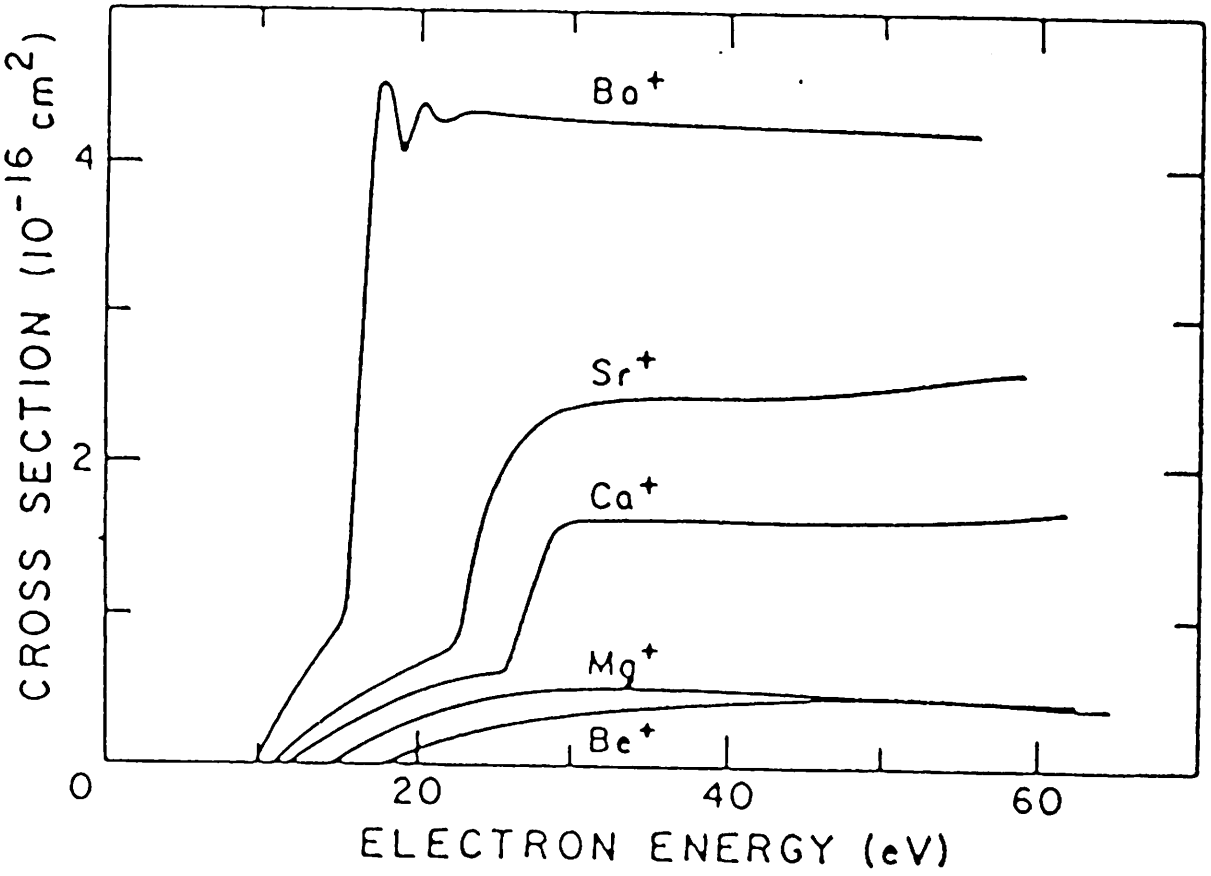

Fig.8-4. Single ionization cross sections for the alkaline earth ions. Ba^+ -- ref.85), Sr^+ and Ca^+ -- ref.80), Mg^+ -- ref.105), Be^+ -- ref.104).

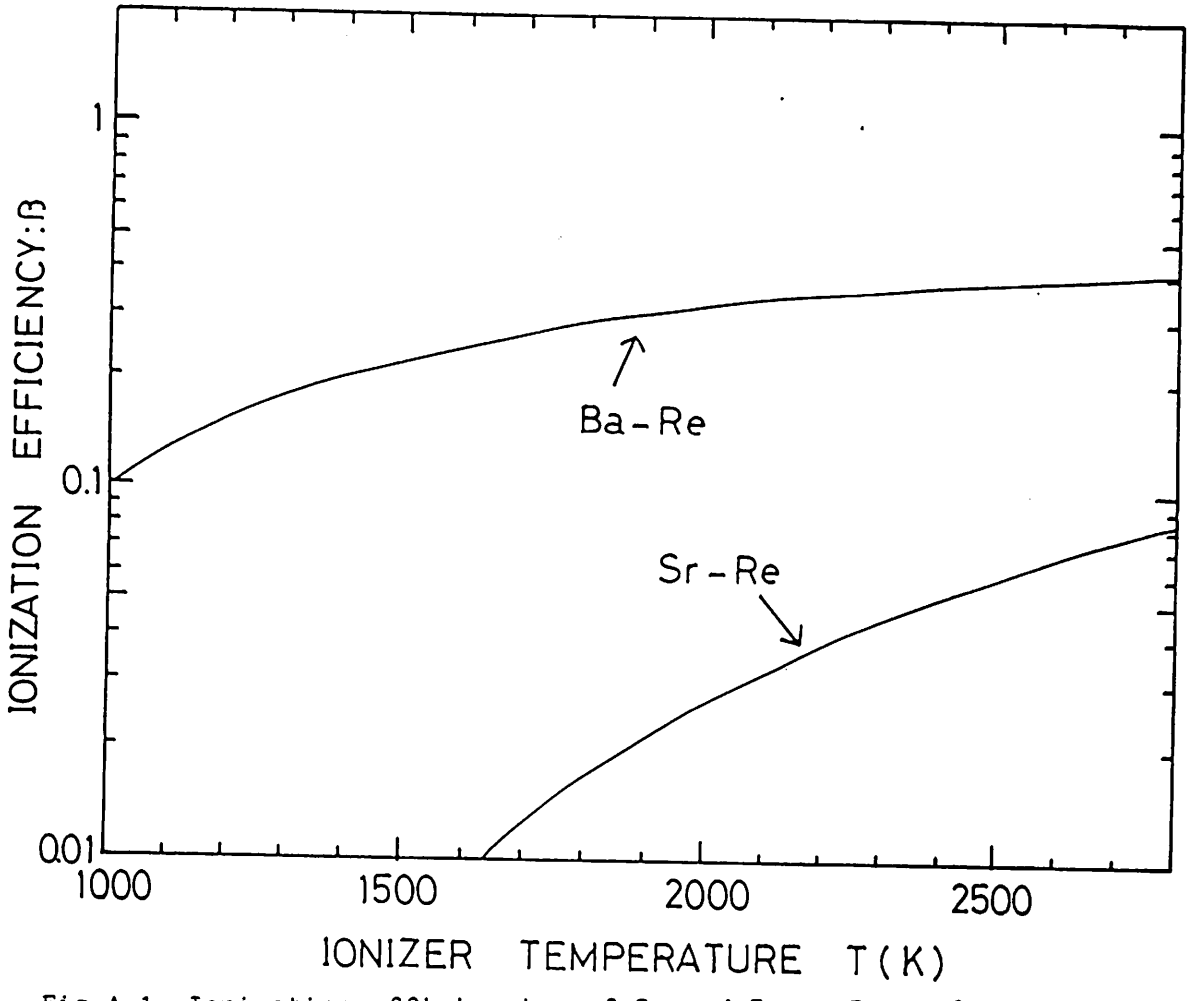

Fig.A-1. Ionization efficiencies of Sr and Ba on Re as functions of the ionizer temperature calculated from the equation (A-6).

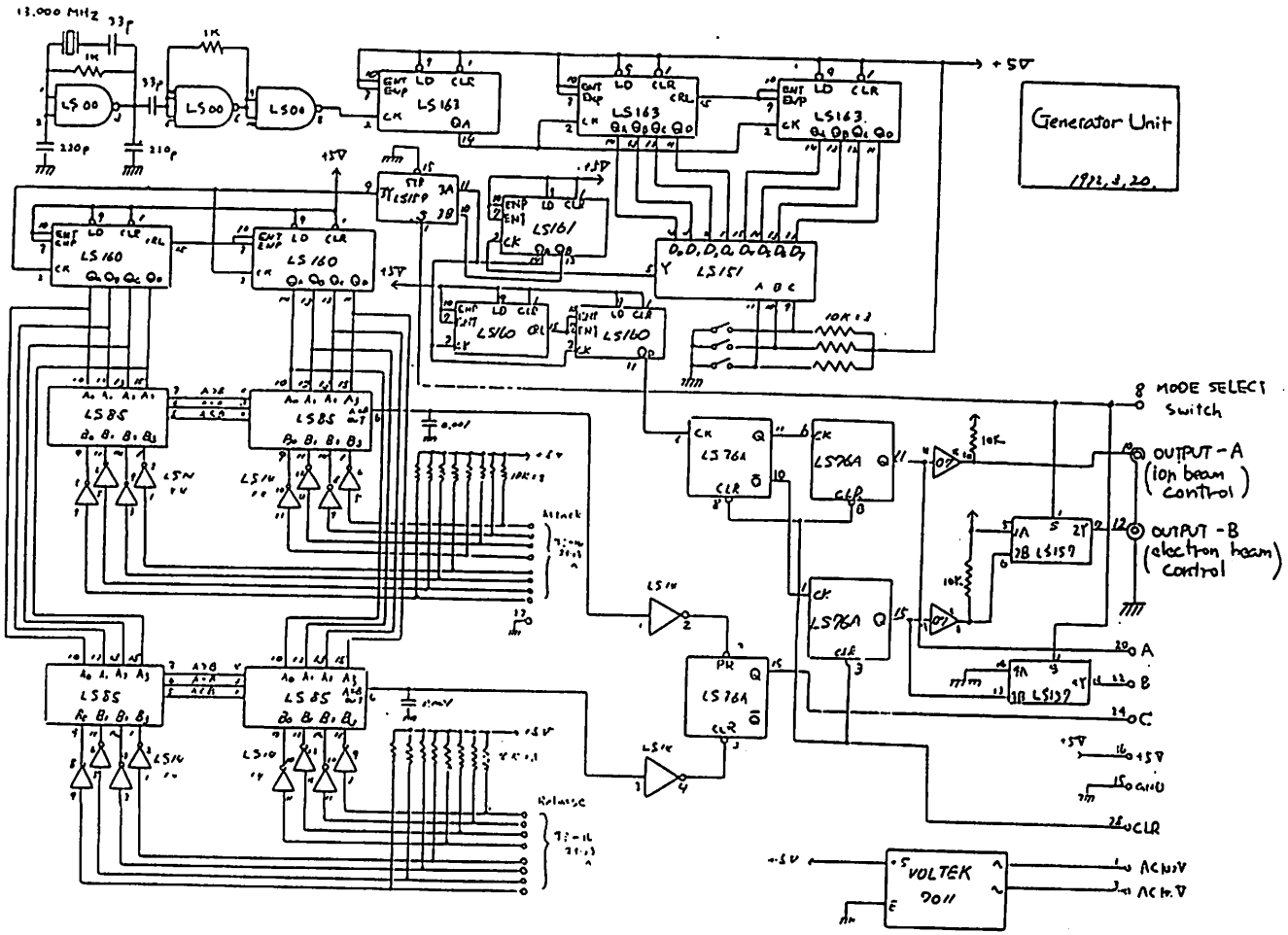

Fig.B-1. Circuit diagram of the control pulse generator unit.

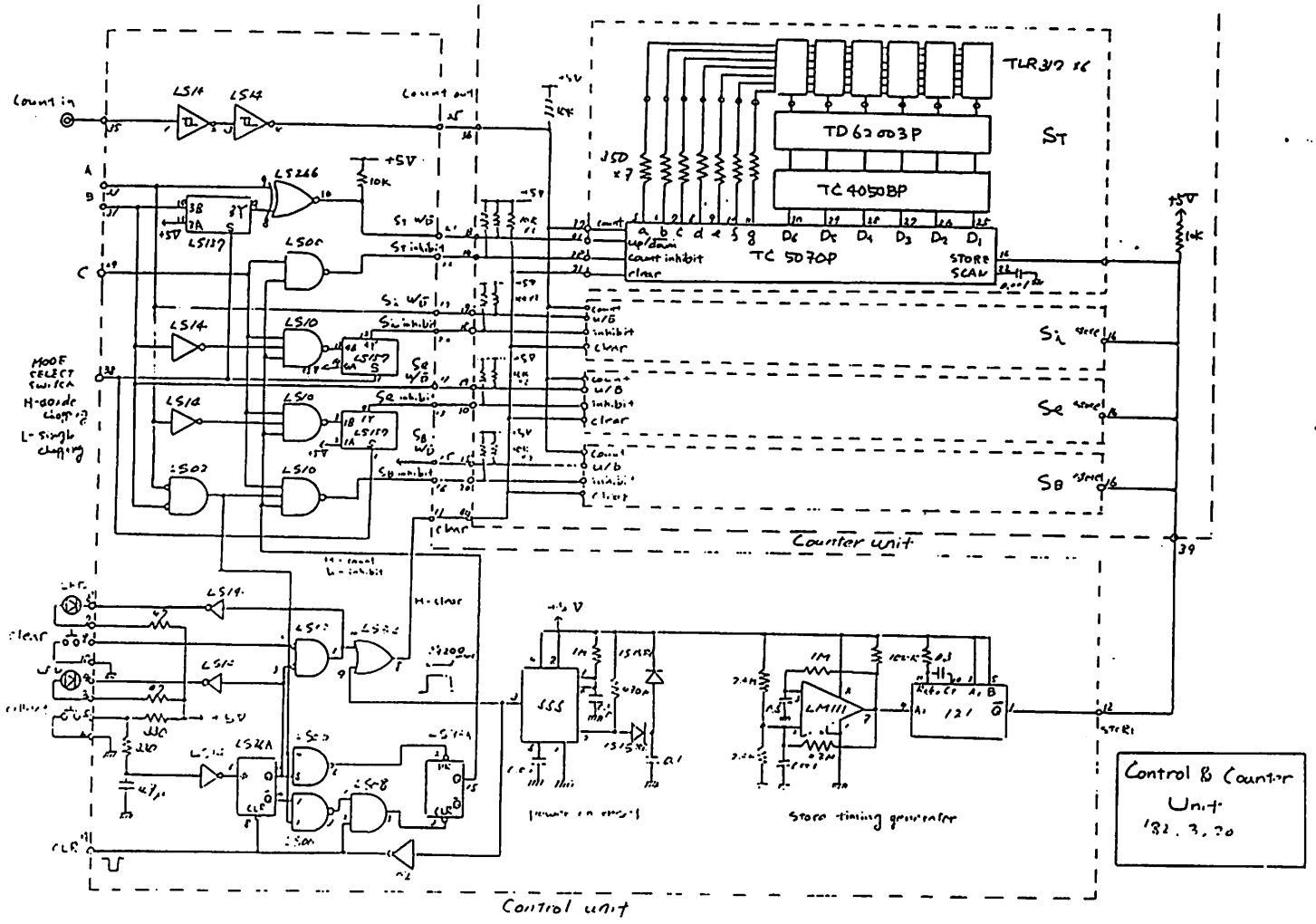

Fig.B-2. Circuit diagram of the multiplexer unit and the counter unit.

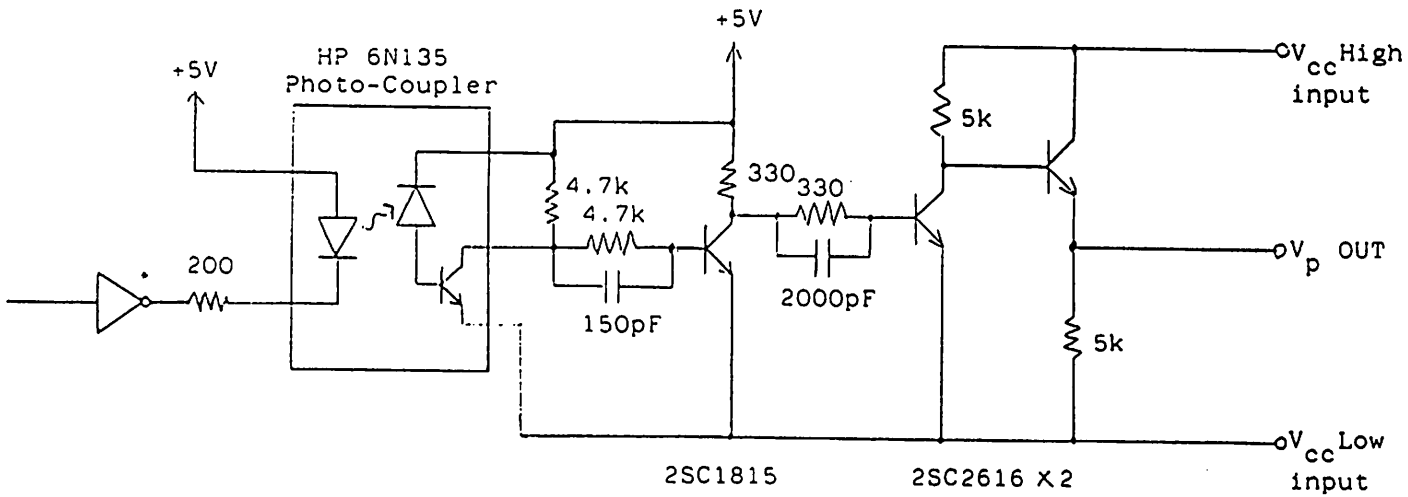

Fig.B-3. Circuit diagram of the chopping pulse driver unit.

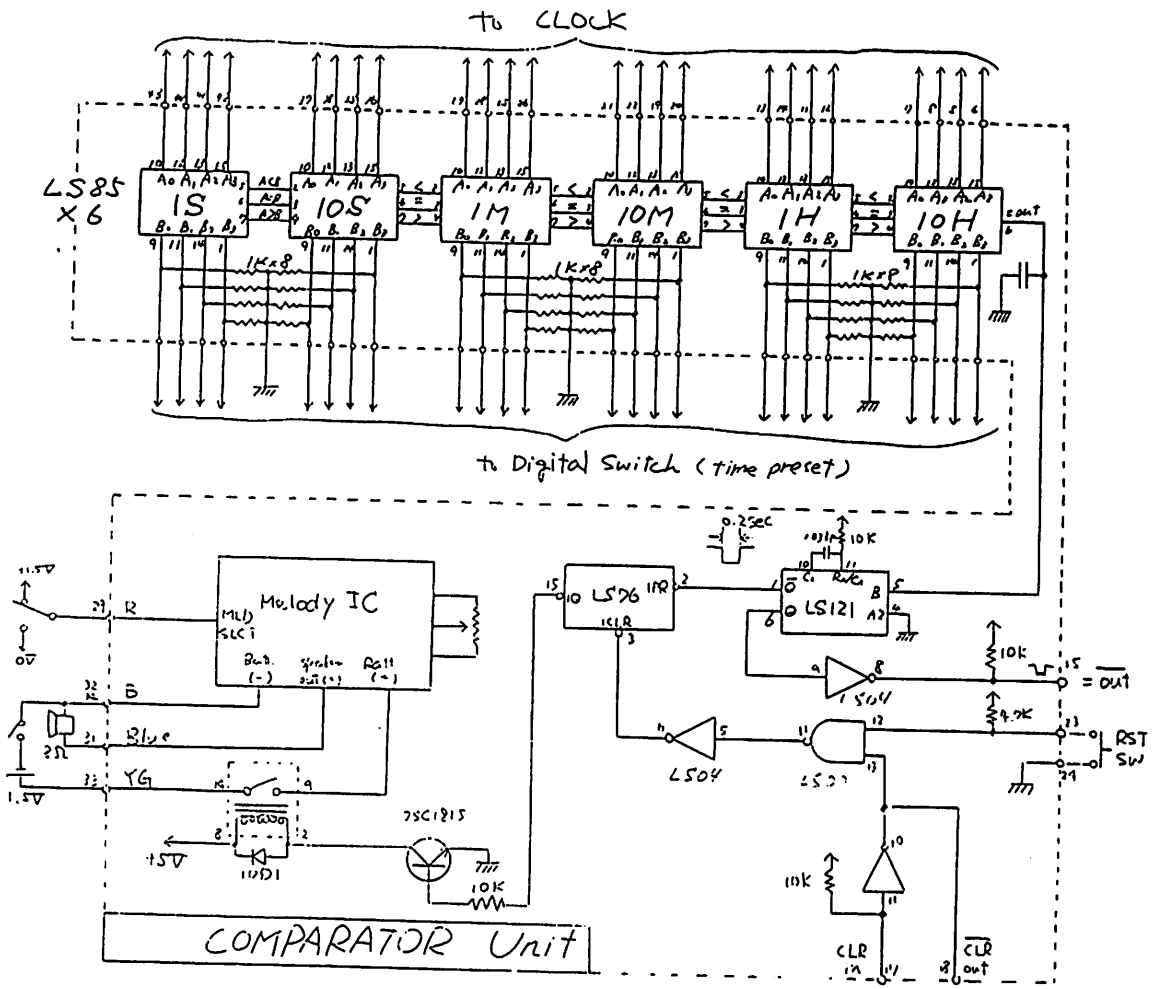

Fig.B-4. Circuit diagram of the time comparator unit.

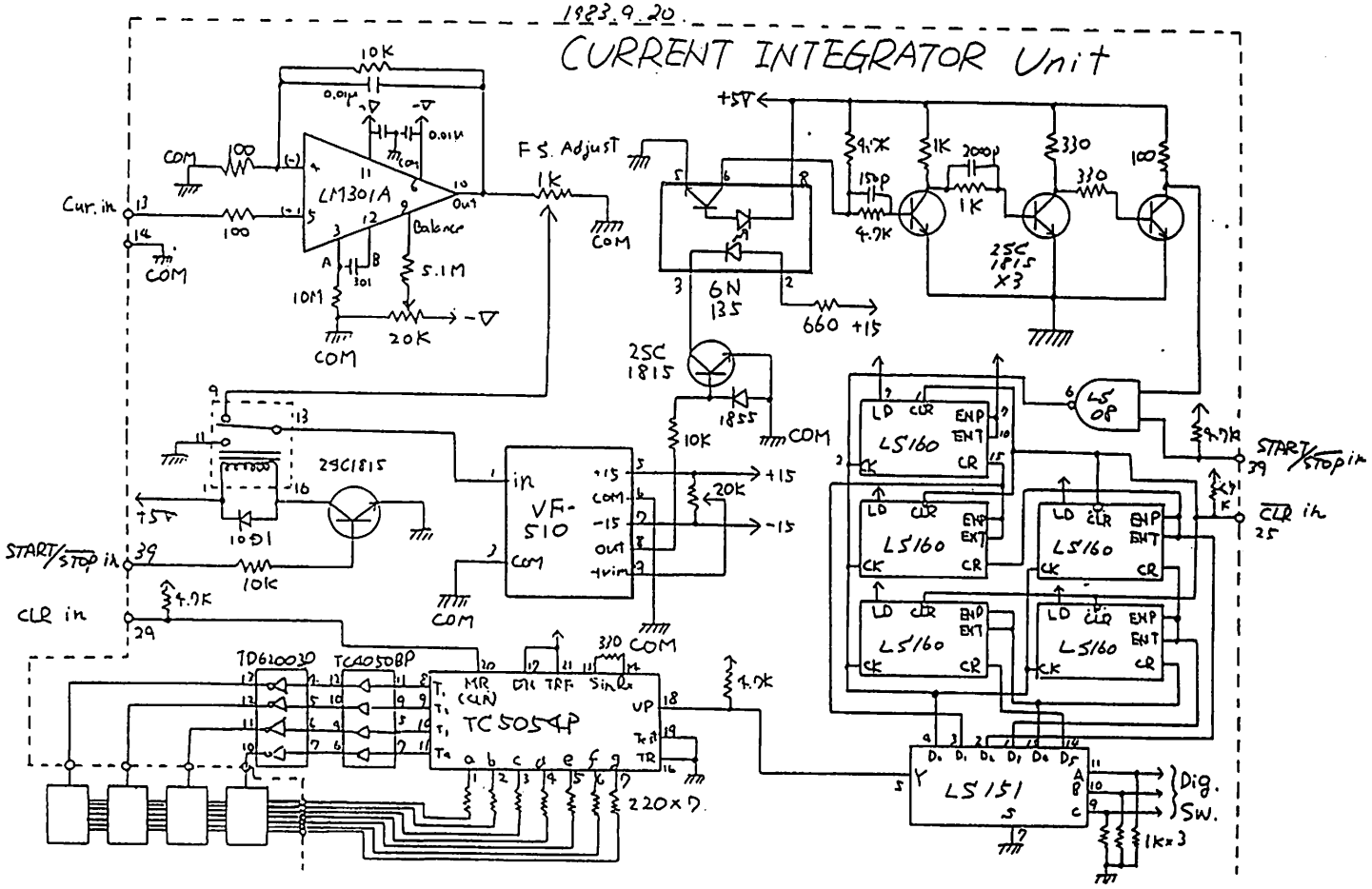

Fig.B-5. Circuit diagram of the current integrator unit.